Lawrence Berkeley National Laboratory
LBL Publications

Title

Sum-Frequency Spectroscopic Studies I. Surface Melting of Ice II. Surface Alignment of Polymers

Permalink

https://escholarship.org/uc/item/6c08418d

Author

Wei, Xing, Ph.D. Thesis

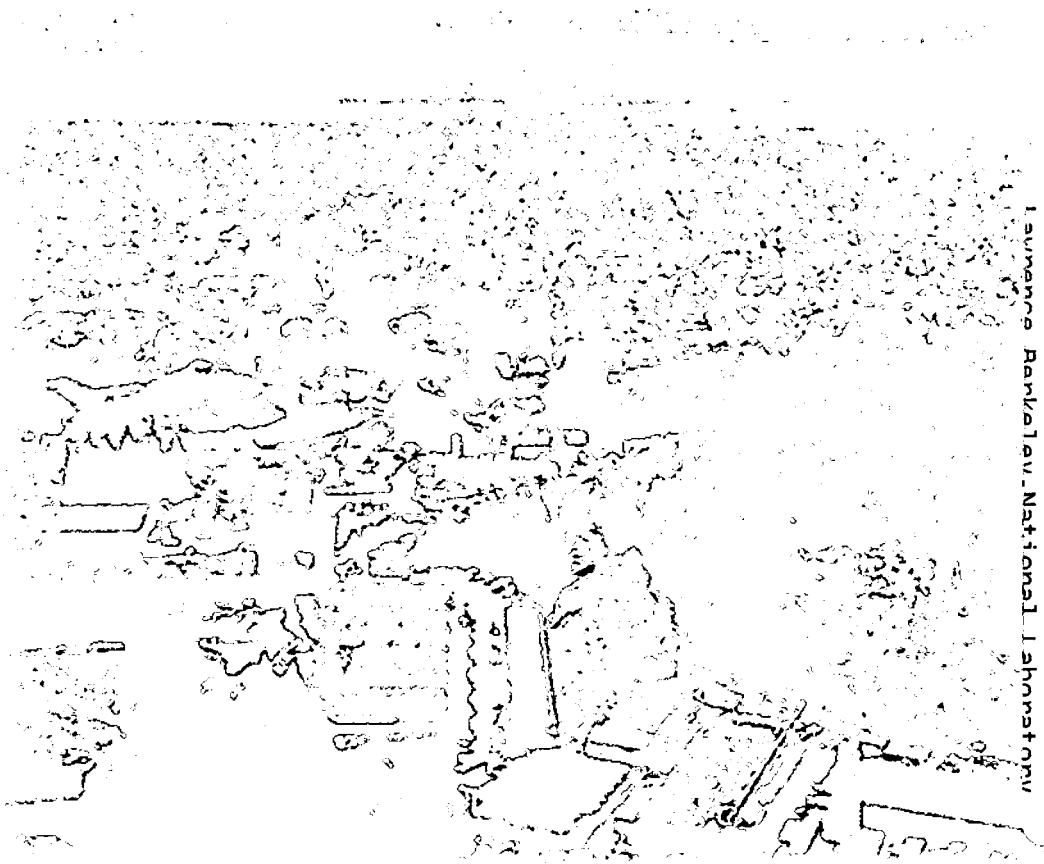**Publication Date**

2000-12-01

Copyright Information

ERNEST ORLANDO LAWRENCE BERKELEY NATIONAL LABORATORY

Sum-Frequency Spectroscopic Studies
I. Surface Melting of Ice
II. Surface Alignment of Polymers

Xing Wei

Materials Sciences Division

December 2000

Ph.D. Thesis

DISCLAIMER

This document was prepared as an account of work sponsored by the United States Government. While this document is believed to contain correct information, neither the United States Government nor any agency thereof, nor the Regents of the University of California, nor any of their employees, makes any warranty, express or implied, or assumes any legal responsibility for the accuracy, completeness, or usefulness of any information, apparatus, product, or process disclosed, or represents that its use would not infringe privately owned rights. Reference herein to any specific commercial product, process, or service by its trade name, trademark, manufacturer, or otherwise, does not necessarily constitute or imply its endorsement, recommendation, or favoring by the United States Government or any agency thereof, or the Regents of the University of California. The views and opinions of authors expressed herein do not necessarily state or reflect those of the United States Government or any agency thereof or the Regents of the University of California.

Sum-Frequency Spectroscopic Studies
I. Surface Melting of Ice
II. Surface Alignment of Polymers

Xing Wei
Ph.D. Thesis

Department of Physics
University of California, Berkeley

and

Materials Sciences Division
Ernest Orlando Lawrence Berkeley National Laboratory
University of California
Berkeley, CA 94720

December 2000

Sum-Frequency Spectroscopic Studies
I. Surface Melting of Ice
II. Surface Alignment of Polymers

by

Xing Wei

B.S. (Fudan University, Shanghai) 1990
M.S. (Fudan University, Shanghai) 1992

A dissertation submitted in partial satisfaction of the
requirements for the degree of
Doctor of Philosophy

in

Physics

in the

GRADUATE DIVISION
of the
UNIVERSITY of CALIFORNIA at BERKELEY

Committee in charge:

Professor Y. R. Shen, Chair
Professor R. Falcone
Professor R. Saykally

Fall 2000

Abstract

Sum-Frequency Spectroscopic Studies

I. Surface Melting of Ice

II. Surface Alignment of Polymers

by

Xing Wei

Doctor of Philosophy in Physics

University of California at Berkeley

Professor Y. R. Shen, Chair

Surface vibrational spectroscopy via infrared-visible sum-frequency generation (SFG) has been established as a useful tool to study the structures of different kinds of surfaces and interfaces. This technique was used to study the (0001) face of hexagonal ice (I_h). SFG spectra in the O-H stretch frequency range were obtained at various sample temperatures. For the vapor(air)/ice interface, the degree of orientational order of the dangling OH bonds at the surface was measured as a function of temperature. Disordering sets in around 200 K and increases dramatically with temperature, which is strong evidence of surface melting of ice. For the other ice interfaces (silica/OTS/ice and silica/ice), a similar temperature dependence of the hydrogen bonded OH stretch peak was observed; the free OH stretch mode, however, appears to be different from that of the vapor(air)/ice interface due to

2

interactions at the interfaces.

The technique was also used to measure the orientational distributions of the polymer chains on a rubbed polyvinyl alcohol surface. Results show that the polymer chains at the surface appear to be well aligned by rubbing, and the adsorbed liquid crystal molecules are aligned, in turn, by the surface polymer chains. A strong correlation exists between the orientational distributions of the polymer chains and the liquid crystal molecules, indicating that the surface-induced bulk alignment of a liquid crystal film by rubbed polymer surfaces is via an orientational epitaxy-like mechanism.

This thesis also contains studies on some related issues that are crucial to the above applications. An experiment was designed to measure SFG spectra in both reflection and transmission. The result confirms that SFG in reflection is generally dominated by the surface contribution. Another issue is the motional effect due to fast orientational motion of molecules at a surface or interface. Calculations show that the effect is significant if the molecular orientation varies over a broad range within the vibrational relaxation time. The stretch vibration of the free OH bonds at the vapor/water interface is used to illustrate the importance of the effect.

Contents

Acknowledgements

I am truly indebted to my advisor, Prof. Yuen Ron Shen, for his continuous support and guidance in the past several years. It was back in 1994 when I first contacted Prof. Shen, who encouraged me to apply for graduate school in Berkeley. With his strong support, I came and joined his research group in the fall of 1995. During my graduate study I have learned from him not only the theories and techniques of nonlinear optics but also a high standard of doing research. His endless curiosity and enthusiasm in science and technology, his ability to construct clear physical pictures without getting lost in mathematics, and his availability to help his students and colleagues are among his many characteristics that I hope to emulate throughout my career.

Another person of great influence on me was Prof. Xiao-feng Jin, who helped me in almost every critical step I made in my academic life. I first met him in 1986, when he was still a graduate student in Fudan University in Shanghai and helped me choose Fudan for my undergraduate education. In 1989-1990, after a complicated political situation, Prof. Jin helped me get into the graduate school at Fudan University to receive a Master's degree in Physics. In 1994, when I was working as a sales engineer in Beijing, Prof. Jin strongly recommended me to Prof. Shen. I definitely would not have come to this stage in my life without his help.

I am grateful to three fellow graduate students and mentors, Xiao-wei Zhuang, Deseok Kim, and Paulo B. Miranda. I took over an interesting project (rubbed polymers) from Dr. Zhuang and Dr. Kim when they graduated, which resulted in my first formal publication during my Ph.D. research. Dr. Miranda was the person who started the project

on surface melting of ice. I cannot express my gratitude to Dr. Miranda and Dr. Kim for teaching me in every detail how to use and maintain the sum-frequency vibrational spectroscopy setup.

I would like to thank all the postdocs, visiting scholars and students in our group. Joachim Diener taught me a great deal about computers and networks. Tomohisa Goto prepared the first rubbed polyvinyl alcohol (PVA) sample for my experiment on rubbed polymers. My collaboration with Hermann Held and Alex I. Lvovsky to investigate the bulk contributions in surface nonlinear optical spectroscopy was successful and rewarding. It was my great pleasure to work with Karl-Heinz Ernst, Wolfgang Beck, Markus Raschke, Masashito Oh-e, Lei Xu, Chun Zhang, and Song-Hee Han. Frequent discussions with Steve Baldelli from the Somorjai group were also very helpful to me. To newer graduate students in our group, John A. McGuire, Seok-Cheol Hong, Mikhail Belkin, Thai V. Truong and Na Ji, I wish them good luck and success. I owe special thanks to John for proofreading almost every manuscript I wrote, including this thesis.

Finally, I would like to thank my parents, who experienced both my excitement and frustration in these years and provided the greatest spiritual support. I wish them good health and an enjoyable retirement, and I hope they will always be proud of me.

Chapter 1

Introduction

1.1   Surface sum-frequency vibrational spectroscopy

The first experimental demonstration of surface vibrational spectroscopy via infrared-visible sum-frequency generation (SFG) was published by the Shen group in 1987 [1], in which a sum-frequency vibrational spectrum from a coumarin 504 dye monolayer on a fused silica substrate was reported. Since then, surface SFG vibrational spectroscopy has attracted much attention. Today, surface SFG vibrational spectroscopy continues to develop and has become a powerful tool to study the structures of surfaces and interfaces.

The basic principles of sum-frequency vibrational spectroscopy can be found in the review article [2] by Shen. Being a second-order nonlinear optical process, SFG is forbidden under the electric-dipole approximation in a medium with inversion symmetry, but is allowed at a surface or interface where the inversion symmetry is broken. This unique feature makes SFG extremely surface-specific and sensitive. Being a purely optical technique involving only light waves, SFG has promoted surface science to a new level by
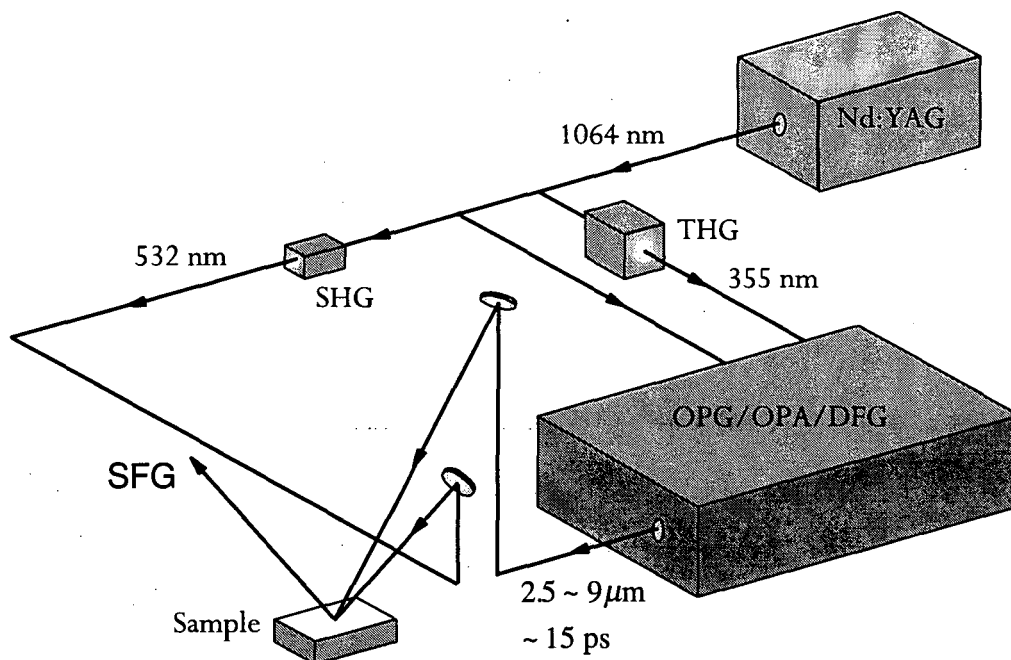
Figure 1.1: Schematic view of the SFG setup.

probing surfaces and interfaces that "traditional" surface science techniques (low energy electron diffraction, Auger electron spectroscopy, photoemission spectroscopy, etc.) do not have access to. Typical examples include studies of surfaces or interfaces of solids or liquids under high vapor pressure, surface chemical reactions in real atmosphere, buried interfaces, and so on. This thesis will be focused on two particular systems, the ice surface and a rubbed polymer (polyvinyl alcohol) surface.

1.2 Experimental setup

A typical SFG experimental setup has also been described in Ref. [2]. Below are some details of the SFG setup in Room B145 Birge Hall, from which we obtained most of the results in this thesis. A schematic view of the system is shown in Fig. 1.1.

Unless otherwise specified, all the SFG experiments were carried out with a visible beam at 532 nm (the second harmonic from a Continuum PY61C-20 picosecond Nd:YAG laser) and an infrared beam tunable from 2.5 to 9 μm (1100 to 4000 cm^{-1}) generated from a home-made optical parametric generator/amplifier (OPG/OPA) system and a difference frequency generation (DFG) stage which mixes the idler output of the OPG/OPA and the fundamental 1.064 μm. A detailed description of the OPG/OPA system can be found in Ref. [3]. We replaced the gratings in the OPG/OPA system with infrared gratings (900 groves/mm) in August, 1997 to seed the OPA with the idler instead of the signal, and improved the output linewidth to $\sim$ 6 cm^{-1} (FWHM). Both visible and infrared input beams had a pulse duration of $\sim$ 15 ps, a repetition rate of 20 Hz, and a beam diameter of $\sim$ 1 mm at the sample. The input intensities were $\sim$ 1.5 mJ and $\sim$ 100 μJ per pulse for the visible and the infrared, respectively. The infrared input frequency was further calibrated with molecular absorption lines in the gas phase. Figure 1.2 shows an example of infrared frequency calibration in the OH stretch frequency range. The accuracy of such a calibration is about 2 cm^{-1}.

Figure 1.3 shows the geometry of the input/output beams in the SFG experiment, in which X, Y, Z and x, y, z refer to the lab-fixed reference frame and sample-fixed reference frame, respectively. Distinguishing X, Y, Z and x, y, z is important only if anisotropic samples are used, e.g., rubbed polymer surfaces (Chap. 3). For isotropic samples, we do not expect the SFG signal to depend on the azimuthal angle γ in Fig. 1.3 and therefore do not distinguish X, Y, Z and x, y, z. For all experiments in this thesis except the bulk contribution experiment (Chap. 4), the incidence angles were β_1=45° and β_2=57° for the
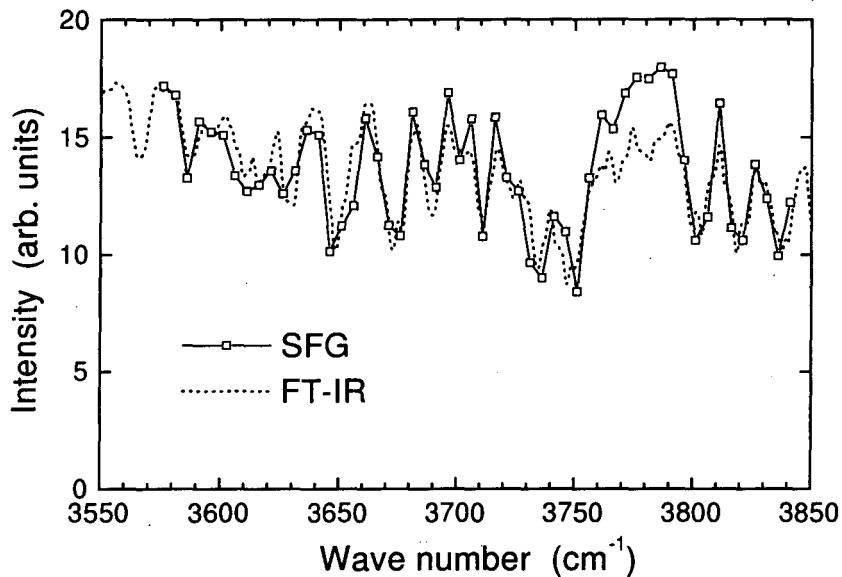
Figure 1.2: Calibration of the infrared frequency in the OH stretch frequency range. Square symbols represent the SFG intensity obtained from a z-cut quartz reference sample. Absorption lines in the SFG spectrum are due to the water vapor absorption in the infrared beam path. The dotted line is a smoothed infrared transmission spectrum of water vapor measured by Fourier-transform infrared spectroscopy (FT-IR).
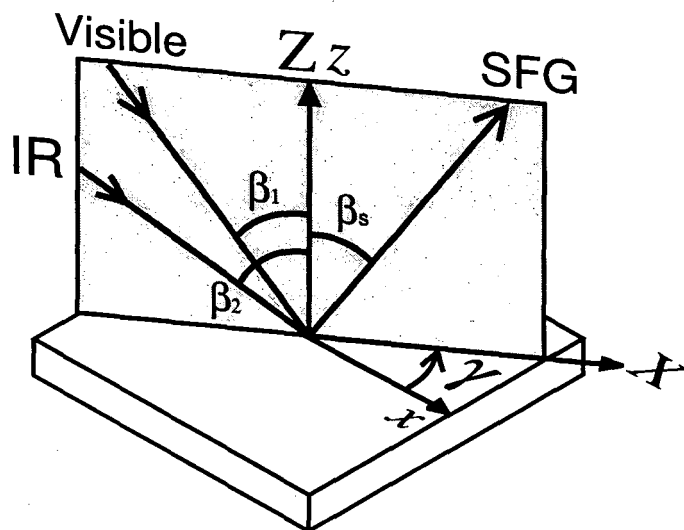
Figure 1.3: Geometry of the input/output beams in the SFG experiment.

visible and the infrared, respectively.

The SFG output was detected in the reflected direction by a Hamamatsu R292 head-on photomultiplier tube (PMT) with a quantum efficiency of $20 - 25\%$. The high voltage applied to the PMT varies between 800 V and 1.1 kV depending on the signal intensity. The PMT output was then measured with a Stanford Research SR250 gated integrator with the gate width and the sensitivity set to 30 ns and 20 mV, respectively.

The SFG signal from our setup covers four orders of magnitude, ranging from a few percent of a photon to a few hundred photons per laser shot. For weak signals (on average less than 1 photon/shot), the PMT was used in the photon counting mode [4]. For stronger signals, the total integrated signal was recorded (integral mode). We found that in the integral mode the gated integrator output increases with the input number of photons in a nonlinear fashion, presumably due to the PMT saturation. Figure 1.4 shows the relation between the integrated signal and the input number of photons, which was measured in the photon counting mode by attenuating the signal with polarizers and neutral density filters. The solid curves in Fig. 1.4 are empirical fits using

$$N = 3.0\,I\,(1 + 0.48\,I) \quad \text{for 1100V} ,$$

$$N = 6.4\,I\,(1 + 0.48\,I) \quad \text{for 1000V} ,$$

$$N = 16.1\,I\,(1 + 0.48\,I) \quad \text{for 900V} ,$$

$$N = 45\,I\,(1 + 0.48\,I) \quad \text{for 800V} ,$$

where I is the gated integrator output in volts. The above relations were used in all the measurements to correct the saturation effect of the PMT.
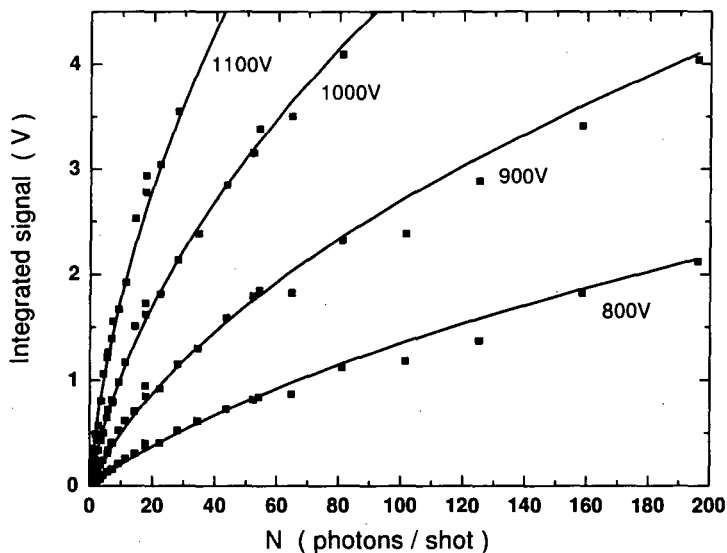
Figure 1.4: Calibration of the photomultiplier tube with various applied votages.

1.3 Standardization

As more and more research groups around the world have implemented SFG vibrational spectroscopy in recent years, we find it important for different groups to compare not only the spectral features in their SFG results but also the vibrational resonance peak intensities. However, this is not easy to do because different SFG systems have different pulse energies, pulse durations, spot sizes, detector efficiencies, etc. For this reason, the SFG intensity in the literature is mostly presented in arbitrary units, which poses a serious problem for different groups to compare their results quantitatively. To solve this problem, we present our SFG spectra in more meaningful units. In the following we address this issue in detail.

1.3.1 Effective surface nonlinear susceptibility

Surface SFG results from a second-order nonlinear polarization induced at an interface by two input fields $\mathbf{E}(\omega_1)$ and $\mathbf{E}(\omega_2)$ at frequencies ω_1 (visible) and ω_2 (infrared), respectively,

$$\mathbf{P}^{(2)}(\omega_s) = \epsilon_0 \boldsymbol{\chi}^{(2)} : \mathbf{E}(\omega_1)\mathbf{E}(\omega_2) , \qquad (1.1)$$

where $\boldsymbol{\chi}^{(2)}$ denotes the surface nonlinear susceptibility tensor, which is a physical quantity that does not depend on the experimental setup. Note that Eq. (1.1) has appeared in different forms depending on the conventions, which can cause a lot of confusion. This will be discussed in Appendix A.

Ideally, one could present all the nonvanishing elements of $\chi_{ijk}^{(2)}(\omega_2)$ as the SFG spectra for each sample measured. However, this is not practical because in most cases $\chi_{ijk}^{(2)}(\omega_2)$ cannot be uniquely determined simply from the SFG measurement. It can be shown that if both input fields are treated as plane waves, the SFG output is also a plane wave and its intensity is given by

$$I(\omega_s) = \frac{\omega_s^2}{8\epsilon_0 c^3 \cos^2 \beta_s} |\chi_{\text{eff}}^{(2)}|^2 I(\omega_1) I(\omega_2) . \qquad (1.2)$$

Here, β_s is the exit angle of the SFG output, $I(\omega_i)$ is the beam intensity at ω_i, and $\chi_{\text{eff}}^{(2)}$ is the effective surface nonlinear susceptibility defined as

$$\chi_{\text{eff}}^{(2)} = [\mathbf{L}(\omega_s) \cdot \hat{\mathbf{e}}_s] \cdot \boldsymbol{\chi}^{(2)} : [\mathbf{L}(\omega_1) \cdot \hat{\mathbf{e}}_1][\mathbf{L}(\omega_2) \cdot \hat{\mathbf{e}}_2] \qquad (1.3)$$

with $\hat{\mathbf{e}}_i$ being the unit polarization vector of the optical field at ω_i and $\mathbf{L}(\omega_i)$ the tensorial Fresnel factor (Appendixes B). A practical difficulty in deducing $\chi_{ijk}^{(2)}$ arises from the

fact that the Fresnel factors often contain some unknown parameters $\epsilon'(\omega_i)$, known as the dielectric constant of the surface layer (Appendix C).

However, as Eq. (1.2) shows, $|\chi_{\text{eff}}^{(2)}(\omega_2)|^2$ has a very simple relation to the SFG output intensity, and can be determined purely from experiment. Using $|\chi_{\text{eff}}^{(2)}(\omega_2)|^2$ to present SFG spectra seems to be a good compromise. In this thesis, most of the SFG spectra will be presented with $|\chi_{\text{eff}}^{(2)}(\omega_2)|^2$ in MKS units so that others can easily compare their results with ours quantitatively. The only disadvantage is that $|\chi_{\text{eff}}^{(2)}(\omega_2)|^2$ still depends on the incidence angles, which has to be taken into account when we compare $|\chi_{\text{eff}}^{(2)}(\omega_2)|^2$ obtained from two different SFG setups.

Note that Eq. (1.2) sometimes appears in a slightly different form (see, for example, Ref. [2]), i.e.,

$$I(\omega_s) = \frac{\omega_s^2 |\chi_{\text{eff}}^{(2)}|^2 I(\omega_1) I(\omega_2)}{8\epsilon_0 c^3 \cos^2 \beta_s \sqrt{\epsilon_1(\omega_s)\epsilon_1(\omega_1)\epsilon_1(\omega_2)}} \,, \tag{1.4}$$

where $\epsilon_1(\omega_i)$ is the dielectric function of "medium 1" in which the intensities $I(\omega_i)$ for the three beams are defined. We have dropped the factor $\sqrt{\epsilon_1(\omega_s)\epsilon_1(\omega_1)\epsilon_1(\omega_2)}$ in Eq. (1.2) because in all our experiments "medium 1" is just air or vacuum and therefore $\epsilon_1(\omega_i) \equiv 1$. This is still true even for buried interfaces or SFG generated in the transmission direction, because we always define $I(\omega_1)$ and $I(\omega_2)$ in air or vacuum before the the two input beams enter the sample, and define $I(\omega_s)$ in air or vacuum after the sum-frequency beam exits the sample. Accordingly, the Fresnel factors in Eq. (1.2) are always defined as the coefficients relating the field components in the interfacial layer to the corresponding ones in air or vacuum (see an example in Appendix B).

1.3.2 Quartz reference

Equation (1.2) shows that one can measure $|\chi_{\text{eff}}^{(2)}|^2$ of a sample by comparing its SFG intensity with that from a standard reference sample with a known $\chi_{\text{eff}}^{(2)}$. In the Shen group, we have been using quartz (α-SiO$_2$) crystals as the reference samples for many years. A quartz crystal gives a reasonably strong SFG signal due to its well known bulk nonlinearity. It has a wide transparency range $0.15 - 4.5$ μm (beyond 4.5 μm quartz absorbs strongly and alternative reference samples should be considered). For all the experiments in this thesis, a z-cut quartz crystal was used as the reference sample. This section presents our calculation for the effective surface nonlinear susceptibility $|\chi_{\text{eff}}^{(2)}|$ of the z-cut quartz surface, with which we calibrated the SFG signals and obtained the spectra $|\chi_{\text{eff}}^{(2)}(\omega_2)|^2$ from different samples.

The SFG signal from crystalline quartz is mainly from the bulk, which has D_3 symmetry with the following nonvanishing $\chi_{ijk}^{(2)}$ elements

$$\chi_{xxx}^{(2)} = -\chi_{xyy}^{(2)} = -\chi_{yyx}^{(2)} = -\chi_{yxy}^{(2)} = \chi_{\text{q}}^{(2)} \ ,$$

$$\chi_{xyz}^{(2)} = -\chi_{yxz}^{(2)} \ ,$$

$$\chi_{xzy}^{(2)} = -\chi_{yzx}^{(2)} \ ,$$

$$\chi_{zxy}^{(2)} = -\chi_{zyx}^{(2)} \ ,$$

among which the elements in the first row (defined as $\chi_{\text{q}}^{(2)}$ below) are much larger than the others [5]. In the following calculation we neglect all the weaker elements such as $\chi_{xyz}^{(2)}$. The formal solution for the reflected SFG amplitude from a medium with a bulk nonlinear susceptibility can be found in Ref. [6]. Applying it to a z-cut quartz crystal shows that the

SFG intensity is maximized when the x-axis of the crystal is in the incidence plane, and the absolute values of the effective surface nonlinear susceptibilities are

$$|\chi_{\text{eff}}^{(2)}(ssp)| = \cos\beta_2 L_{YY}(\omega_s)L_{YY}(\omega_1)L_{XX}(\omega_2)\chi_{\text{q}}^{(2)}l_c \ ,$$

$$|\chi_{\text{eff}}^{(2)}(sps)| = \cos\beta_1 L_{YY}(\omega_s)L_{XX}(\omega_1)L_{YY}(\omega_2)\chi_{\text{q}}^{(2)}l_c \ ,$$

$$|\chi_{\text{eff}}^{(2)}(ppp)| = \cos\beta_s \cos\beta_1 \cos\beta_2 L_{XX}(\omega_s)L_{XX}(\omega_1)L_{XX}(\omega_2)\chi_{\text{q}}^{(2)}l_c \ . \tag{1.5}$$

Here, β_i and L_{ii} are the incidence angle and Fresnel factor, and l_c is the effective coherence length

$$l_c = \frac{1}{|k_{2z}(\omega_s) - k_{2z}(\omega_1) - k_{2z}(\omega_2)|}$$

$$= \frac{1}{2\pi\left(\frac{\sqrt{n(\omega_s)^2-\sin^2\beta_s}}{\lambda_s} + \frac{\sqrt{n(\omega_1)^2-\sin^2\beta_1}}{\lambda_1} + \frac{\sqrt{n(\omega_2)^2-\sin^2\beta_2}}{\lambda_2}\right)}$$

for the reflection geometry, and

$$l_c = \frac{1}{2\pi\left|\frac{\sqrt{n(\omega_s)^2-\sin^2\beta_s}}{\lambda_s} - \frac{\sqrt{n(\omega_1)^2-\sin^2\beta_1}}{\lambda_1} - \frac{\sqrt{n(\omega_2)^2-\sin^2\beta_2}}{\lambda_2}\right|}$$

for the transmission geometry. For the bulk nonlinearity of quartz, we neglect the dispersion and take

$$\chi_{\text{q}}^{(2)} = 4d_{11} \approx 1.60 \times 10^{-12} \ \frac{\text{m}}{\text{V}} \ , \tag{1.6}$$

where d_{11} refers to the nonlinear coefficient for SHG, and its value for $\lambda=1.064$ μm found in Ref. [5] was used. The factor 4 arises from different conventions in the definitions of $\chi_{ijk}^{(2)}$ elements for SFG and d_{ijk} coefficients for SHG (see Appendix A).

For different experiments, $|\chi_{\text{eff}}^{(2)}|$ of the z-cut quartz surface may vary due to different coherence lengths and Fresnel factors. The calculated $|\chi_{\text{eff}}^{(2)}|$ of the quartz reference for different experiments in this thesis are listed in Tables 1.1, 1.2 and 1.3 .

Table 1.1: $\chi_{\text{eff}}^{(2)}$ of the z-cut quartz reference calculated from Eq. (1.5) for the experiments in Chap. 2 (ice) and Chap. 5 (water). Shown together are some parameters used in this calculation. The infrared wavelength corresponds to $\omega_2/(2\pi c)$ =3700 cm^{-1} (the free OH stretch frequency). For convenience the birefringence of the crystal is neglected and the refractive index of the ordinary wave n_o is used for all polarizations. The calculation is for SFG in the reflected direction only. The coherence length $l_c \approx 26$ nm.

	ω_s	ω_1	ω_2
λ	444 nm	532 nm	2.7 μm
$n = n_o$	1.553	1.547	1.49
β	46.8°	45°	57°
L_{XX}	.90	.90	1.01
L_{YY}	.67	.68	.61

$\chi_{\text{eff}}^{(2)}(ssp)$	1.05×10^{-20} m^{2}V^{-1}
$\chi_{\text{eff}}^{(2)}(sps)$	1.09×10^{-20} m^{2}V^{-1}
$\chi_{\text{eff}}^{(2)}(ppp)$	0.92×10^{-20} m^{2}V^{-1}

Table 1.2: $\chi_{\text{eff}}^{(2)}$ of the z-cut quartz reference calculated from Eq. (1.5) for the experiment in Chap. 3 (rubbed polymer). Shown together are some parameters used in this calculation. The infrared wavelength corresponds to $\omega_2/(2\pi c)$ =2900 cm^{-1} (center of the CH stretch frequency range). The calculation is for SFG in the reflected direction only. The coherence length $l_c \approx 27$ nm.

	ω_s	ω_1	ω_2
λ	460 nm	532 nm	3.4 μm
$n = n_o$	1.553	1.547	1.49
β	46.5°	45°	57°
L_{XX}	.90	.90	1.01
L_{YY}	.67	.68	.61

$\chi_{\text{eff}}^{(2)}(ssp)$	1.08×10^{-20} m^{2}V^{-1}
$\chi_{\text{eff}}^{(2)}(sps)$	1.12×10^{-20} m^{2}V^{-1}
$\chi_{\text{eff}}^{(2)}(ppp)$	0.94×10^{-20} m^{2}V^{-1}

12

Table 1.3: $\chi_{\text{eff}}^{(2)}$ of the z-cut quartz reference calculated from Eq. (1.5) for the experiment in Chap. 4 (bulk contribution). Shown together are some parameters used in this calculation. The infrared wavelength corresponds to $\omega_2/(2\pi c)$ =2900 cm^{-1} (center of the CH stretch frequency range). In the reflected direction (R) the coherence length $l_c \approx 46$ nm, and in the transmitted direction $l_c \approx 755$ nm.

	ω_s(R)	ω_s(T)	ω_1	ω_2
λ	810 nm	810 nm	1064 nm	3.4 μm
$n = n_0$	1.539	1.539	1.534	1.49
β	20.0°	20.0°	45°	57°
L_{XX}	.80	.96	.90	1.01
L_{YY}	.77	.95	.68	.61

	Reflection	Transmission
$\chi_{\text{eff}}^{(2)}(ssp)$	2.1×10^{-20} m^{2}V^{-1}	4.3×10^{-19} m^{2}V^{-1}
$\chi_{\text{eff}}^{(2)}(sps)$	2.2×10^{-20} m^{2}V^{-1}	4.5×10^{-19} m^{2}V^{-1}
$\chi_{\text{eff}}^{(2)}(ppp)$	2.0×10^{-20} m^{2}V^{-1}	3.8×10^{-19} m^{2}V^{-1}

1.4 Thesis highlights

In Chap. 2, we report the use of surface sum-frequency vibrational spectroscopy to study surface melting of ice, a phenomenon proposed by Faraday in 1842. SFG is ideally suited for this study because of its high surface sensitivity and high-vapor-pressure compatibility. By probing the orientational disordering of the first surface monolayer, we found that surface melting of ice appears to set in around 200K. The degree of disordering increases with temperature, and the results indicate that the liquid-like layer on the ice surface is structurally different from the normal water surface [7].

In Chap. 3, we report the use of the same technique to study the surface structure of a rubbed polymer (polyvinyl alcohol, PVA) film. The results allow us to determine the orientational distribution of the surface polymer chains quantitatively. They show explicitly that the polymer chains are well aligned on the surface in the rubbing direction, and explain how a rubbed polymer surface can effectively induce bulk alignment of a liquid crystal film

[8, 9]. This work is highly relevant to liquid crystal display (LCD) technology and more generally to polymer science.

The last two chapter are some "by-products" of my research. Chapter 4 is about the intrinsic bulk contribution in surface sum-frequency vibrational spectroscopy [10]. This is particularly important for the interpretation of the SFG spectra of neat materials. Ice, water and polymer films all belong in this category.

In Chap. 5, we discuss an effect due to molecular motion which has been ignored in the past in nonlinear optical spectroscopy [11]. As sum-frequency vibrational spectroscopy has matured and become more quantitative in recent years, this effect is no longer negligible in the spectral analysis. Neglecting the effect would create difficulty in the understanding of certain spectra. A simple theoretical model, as well as a practical example - the vapor/water interface, will be presented to demonstrate the importance of the effect. This work is on a very fundamental level and could provide new explanations for some long existing but unexplained experimental facts. It is particularly important for the analysis of the free OH bonds on the ice surface (Chap. 2).

Chapter 2

Surface melting of ice

2.1 Introduction

Michael Faraday first proposed the existence of a liquid-like layer on an ice surface below the bulk melting temperature, which we know today as surface melting or premelting of ice [12]. Surface melting is not a unique property of ice but a rather common behavior of many solids including lead [13, 14], argon [15], germanium [16], gallium [17] and aluminum [18]. Ice surface melting is particularly interesting because of its dramatic consequences. It is believed to play an important role in phenomena such as reduction of the frictional coefficient of ice, electrification of thunder clouds, glacier flows, frost heaves, and ozone depletion [19, 20]. The problem has been the subject of numerous theoretical and experimental investigations.

An early calculation based on electrostatic interactions [21] predicts that ice surface melting is a complete surface melting (i.e., the quasi-liquid layer thickness diverges as the temperature approaches the bulk melting temperature), and the onset temperature is

between -3 and -6 °C. A more recent theory based on van der Waals interactions (dispersion force theory) [22], however, predicts that surface melting of ice is incomplete (i.e., the quasi-liquid layer thickness does not diverge before the bulk melting occurs). Molecular dynamics simulations of ice surface melting have also been carried out [23, 24, 25], and the reported onset temperature can be as low as -40 °C [23]. Today, a generally accepted theory of surface melting of ice has not yet been found.

A number of experiments have also been carried out to study this phenomenon. These experiments include photoemission [26], proton backscattering [27], ellipsometry [28, 29], optical reflectometry and interference microscopy [30], nuclear magnetic resonance [31, 32], low energy electron diffraction [33], glancing angle x-ray diffraction [34], helium atom scattering [35], and atomic force microscopy [36, 37]. Ice in contact with other solids has also been investigated by various techniques, e.g., wire regelation [38], quasi-elastic neutron scattering [39], and viscosity measurements [40]. While most of these experiments seem to have confirmed the existence of the liquid-like layer on the ice surface or interface, the details, such as the onset temperature and the temperature dependence of the layer thickness, vary widely from experiment to experiment. Today, the exact nature of surface melting of ice remains controversial, and the structure and properties of the quasi-liquid layer are far from being fully understood.

We note that one serious problem in the studies of ice is its incompatibility with ultra high vacuum (UHV) due to its high vapor pressure (Fig. 2.1), which varies between 1 and 10^{-4} Torr in the temperature range of interest. The high vapor pressure hinders the use of standard UHV surface science techniques at temperatures close to the melting
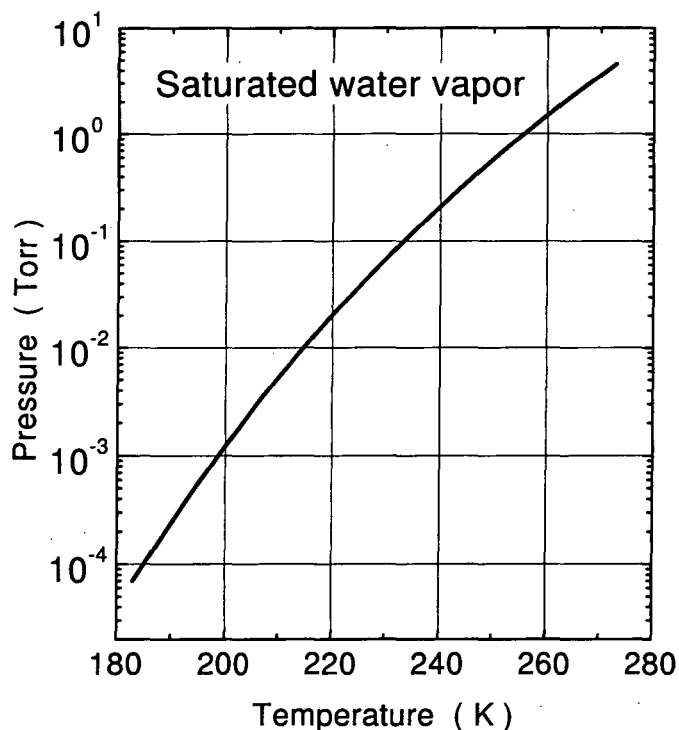
Figure 2.1: Saturated vapor pressure of ice.

temperature of ice. Non-UHV techniques such as ellipsometry and x-ray diffraction can cover a wide range of temperatures, but do not have as high surface sensitivity.

As discussed in Chap. 1, surface SFG vibrational spectroscopy is highly surface-specific and sensitive, and does not require an ultra high vacuum environment. Therefore, it is ideally suited for studies of surfaces and interfaces of ice and water. It has been used before to investigate various interfaces of water [41, 42, 43], as well as an ice film grown on Pt(111) [44]. These experiments demonstrated the capability of SFG vibrational spectroscopy to yield structural information of water and ice that could not be obtained with other experimental techniques. In this chapter we report our studies of surface melting of hexagonal ice (I_h) using this technique. Our studies were focused on the ice interfaces of the (0001) orientation (basal plane), since the (0001) surface is the most stable surface of

ice I_h in nature.

2.2 Theory

2.2.1 Molecular hyperpolarizability of OH bonds

In Chap. 1, we have shown that the SFG signal results from the surface nonlinear susceptibility tensor $\chi_{ijk}^{(2)}$ through Eqs. (1.1)-(1.3). If the infrared frequency ω_2 is tuned across the surface vibrational resonances, the following resonant behavior of $\chi_{ijk}^{(2)}$ is expected:

$$\chi_{ijk}^{(2)}(\omega_2) = \chi_{NR,ijk}^{(2)} + \sum_q \frac{A_{q,ijk}}{\omega_2 - \omega_q + i\Gamma_q} , \tag{2.1}$$

where $\chi_{NR,ijk}^{(2)}$ is a non-resonant background, $A_{q,ijk}$, ω_q, and Γ_q are the amplitude, resonant frequency, and damping constant of the qth vibrational mode. In this experiment on ice, we focus on the OH stretch vibrational modes. The resonant part of $\chi_{ijk}^{(2)}$ can be considered as an ensemble average of the molecular hyperpolarizability tensor $\alpha_{lmn}^{(2)}$, which has similar resonant behavior

$$\alpha_{lmn}^{(2)}(\omega_2) = \sum_q \frac{a_{q,lmn}}{\omega_2 - \omega_q + i\Gamma_q} , \tag{2.2}$$

where the indices l, m, n refer to the molecular reference frame.

The basic idea of using SFG vibrational spectroscopy to study the ice surface structure is quite straightforward. Fig. 2.2 shows the structure of an ideal (0001) basal surface of ice I_h, which is likely to be the case at low temperatures when surface melting does not occur. In great contrast, Fig. 2.3 shows a molecular dynamics simulation of the ice (0001) surface [24] as a quasi-liquid layer is formed. The dramatic change in the orientations of the molecules at the ice surface should have a measurable effect on the tensor $\chi_{ijk}^{(2)}$ (or a
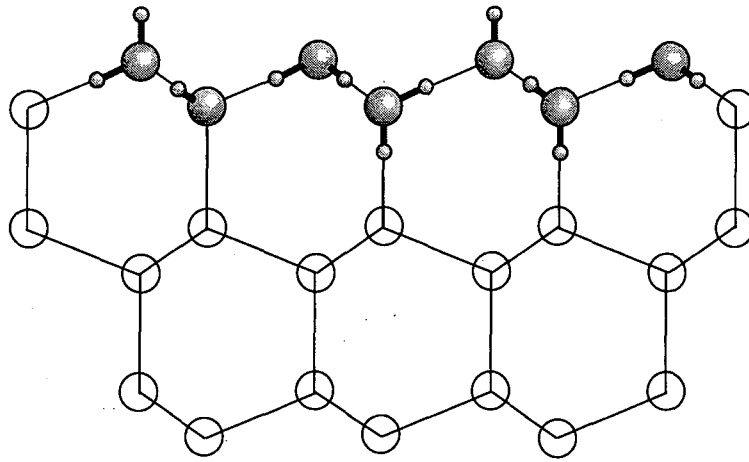
Figure 2.2: Side view of an ideal (0001) basal surface of ice I_h. Note that the free (or dangling) OH bonds are perpendicular to the surface due to the tetrahedral hydrogen bonding.

Figure 2.3: Molecular dynamics simulation of the (0001) basal surface of ice I_h at 265 K (from Ref. [24]).
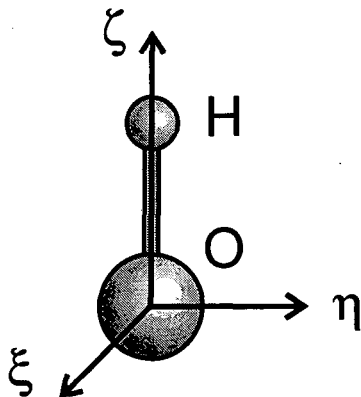
Figure 2.4: Molecular reference frame of a single OH bond, with ζ along the bond direction and ξ, η perpendicular to ζ.

particular resonant mode amplitude $A_{q,ijk}$).

Since our quantitative analysis will be on the free OH stretch mode, we present here our theoretical model of the molecular hyperpolarizability of a free OH bond. The theory of SFG vibrational spectroscopy shows that $a_{q,lmn}$ is related to the infrared and Raman characteristics of a vibrational mode through the equation [45]

$$a_{q,lmn} = -\frac{1}{2\epsilon_0\omega_q}\frac{\partial\mu_n}{\partial Q_q}\frac{\partial\alpha_{lm}^{(1)}}{\partial Q_q} \ , \qquad (2.3)$$

where $\frac{\partial\mu_n}{\partial Q_q}$ and $\frac{\partial\alpha_{lm}^{(1)}}{\partial Q_q}$ are the infrared dipole derivative and the Raman polarizability tensor of the qth vibrational mode, and Q_q is the classical normal coordinate. For a free OH bond,

$$Q_q = \sqrt{m_H}\Delta r \ , \qquad (2.4)$$

where Δr is the change in the OH bond length due to the stretch, and m_H is the mass of a hydrogen atom. Equation (2.3) then becomes

$$a_{q,lmn} = -\frac{1}{2\epsilon_0\omega_q m_H}\frac{\partial\mu_n}{\partial\Delta r}\frac{\partial\alpha_{lm}^{(1)}}{\partial\Delta r} \ . \qquad (2.5)$$

We can use Eq. (2.5) to calculate $a_{q,lmn}$ for the free OH stretch mode. Figure 2.4 shows the molecular reference frame of a single OH bond. The infrared dipole derivative along the bond direction $\hat{\zeta}$ was reported to be

$$\frac{\partial \mu_\zeta}{\partial \Delta r} = 0.157 \text{ (atomic units)} = 2.52 \times 10^{-20} \text{ C} \tag{2.6}$$

from *ab initio* calculations [46], in good agreement with experiments [47]. Although Ref. [46] also suggested that a free OH bond could have a small but non-zero dipole derivative component perpendicular to the bond direction $\hat{\zeta}$, it will be neglected in our simple model. For the Raman polarizability tensor, we use the experimentally deduced values from Ref. [48] (converted to MKS units)

$$\frac{\partial \alpha^{(1)}_{\zeta\zeta}}{\partial \Delta r} = (2.20 \pm 0.13) \times 10^{-30} \frac{\text{mC}}{\text{V}} \ ,$$

$$\frac{\partial \alpha^{(1)}_{\xi\xi}}{\partial \Delta r} = \frac{\partial \alpha^{(1)}_{\eta\eta}}{\partial \Delta r} = (7.0 \pm 0.4) \times 10^{-31} \frac{\text{mC}}{\text{V}} \ ,$$

with the depolarization ratio $r = \frac{\partial \alpha^{(1)}_{\xi\xi}}{\partial \Delta r} / \frac{\partial \alpha^{(1)}_{\zeta\zeta}}{\partial \Delta r} \approx 0.32$. The free OH stretch is at ~ 3700 cm^{-1} [41], which corresponds to an angular frequency

$$\omega_q = 2\pi c \times 3700 \text{ cm}^{-1} = 7.0 \times 10^{14} \text{ sec}^{-1} \ .$$

Inserting these values into Eq. (2.5), we obtain

$$a_{q,\zeta\zeta\zeta} \approx 2.7 \times 10^{-27} \frac{\text{m}^4}{\text{Vsec}} \ ,$$

$$a_{q,\xi\xi\zeta} = a_{q,\eta\eta\zeta} = r a_{q,\zeta\zeta\zeta} \approx 8.6 \times 10^{-28} \frac{\text{m}^4}{\text{Vsec}} \ .$$

$$\tag{2.7}$$

The macroscopic resonant amplitude $A_{q,ijk}$ results from the ensemble average of the microscopic property $a_{q,lmn}$ of the molecules at the surface. Depending on the time

scale of the molecular orientational fluctuations, $A_{q,ijk}$ can be related to $a_{q,lmn}$ through

$$A_{q,ijk} = N_S \sum_{\lambda\mu\nu} a_{q,lmn} \langle (\hat{i} \cdot \hat{l})(\hat{j} \cdot \hat{m})(\hat{k} \cdot \hat{n}) \rangle \qquad (2.8)$$

for the slow-motion limit, or

$$A_{q,ijk} = N_S \sum_{\lambda\mu\nu} a_{q,lmn} \langle (\hat{i} \cdot \hat{l})(\hat{j} \cdot \hat{m}) \rangle \langle (\hat{k} \cdot \hat{n}) \rangle \qquad (2.9)$$

for the rapid-motion limit (see Chap. 5 for the motional averaging effect). Here N_S is the surface density of the molecular groups, and the angle brackets represent the ensemble average. Therefore, if we can obtain $A_{q,ijk}$ for the free OH stretch from our experiment, we can then deduce an approximate orientational distribution of the free OH bonds through Eq. (2.8) or (2.9). We expect that the orientational distribution would be very narrow if the surface layer has an ordered crystalline structure as in Fig. 2.2 but would broaden appreciably if the layer becomes liquid-like as in Fig. 2.3. Note that in Eqs. (2.8) and (2.9) we have neglected the microscopic local field correction which, when fully included, will lead to the relacement of N_S in Eqs. (2.8) and (2.9) with $N_S l_\parallel(\omega_s) l_\parallel(\omega_1) l_\parallel(\omega_2)$. The definition of $l_\parallel(\omega_i)$ can be found in Appendix C.

2.2.2 Symmetry of the ice basal surface

Being a rank-3 tensor, $\chi_{ijk}^{(2)}$ (or $A_{q,ijk}$) has in general 27 elements. Surface symmetry, however, can make some elements vanish and some become mutually dependent. The hexagonal symmetry of the (0001) surface of ice I_h reduces the nonvanishing independent tensor elements to the following three (see Fig. 1.3 for the reference frame):

$$\chi_{zzz}^{(2)} \quad ,$$
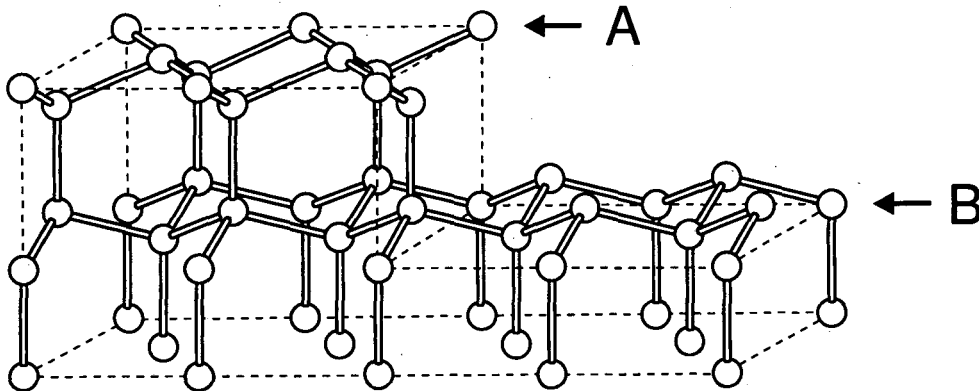
Figure 2.5: The (0001) basal surface of ice I_h with a monolayer-height step. Only oxygen atoms are shown; hydrogen atoms are omitted for clarity. Note that layer A and layer B do not repeat each other by a simple spatial translation but are rotated by 180° with respect to each other in the surface plane.

$$\chi^{(2)}_{xxz} = \chi^{(2)}_{yyz} \ ,$$

$$\chi^{(2)}_{xzx} = \chi^{(2)}_{zxx} = \chi^{(2)}_{yzy} = \chi^{(2)}_{zyy} \ .$$

In the last row we have used the approximation $\chi^{(2)}_{ijk} = \chi^{(2)}_{jik}$, assuming that the visible ω_1 and the sum-frequency ω_s are far away from electronic resonances. The simplicity of $\chi^{(2)}_{ijk}$ (i.e., only three independent components) implies that we can measure the $\chi^{(2)}_{ijk}$ tensor with only three input/output polarization combinations *ssp* (denoting *s-*, *s-*, and *p*-polarized sum-frequency output, visible input, and infrared input, respectively), *ppp*, and *sps*. It also implies that we do not need to rotate the sample in this experiment because $\chi^{(2)}_{ijk}$ of the basal surface of ice I_h appears to be isotropic in the xy plane.

In Ref. [49] Geiger and co-workers, however, drew a different conclusion and claimed that the (0001) surface of ice should possess more non-vanishing $\chi^{(2)}_{ijk}$ elements, such as $\chi^{(2)}_{xxx}$, due to a $3m$ (C_{3v}) symmetry, analogous to that of the Si(111) surface [50]. We do not agree with such an analogy because there is an essential difference between the (0001)

surface of a hexagonal crystal and the (111) surface of a cubic crystal. Figure 2.5 shows an ideal (0001) surface of ice with a monolayer-height step. Due to its dynamic nature, the vapor/ice (0001) interface cannot be atomically flat, but contains steps. We note that layer A and layer B as shown in Fig. 2.5 do not repeat each other by a simple spatial translation, but are rotated by 180° with respect to each other. This is not the case for the Si(111) surface, where adjacent layers always repeat each other by a simple spatial translation. On the ice (0001) surface the two configurations A and B are energetically equivalent, and therefore, domains of type A and type B coexist with equal coverage. Although each type exhibits $3m$ (C_{3v}) symmetry, the ice (0001) surface has an overall 6-fold symmetry instead of 3-fold, in strong contrast to the Si(111) surface.

2.3 Experiment

Ice I_h single crystals were grown by the Bridgeman method from deionized water. The crystal growth apparatus was similar to the one described in Ref. [51]. Typical growth rate was 1 μm/sec (3.6 mm/hour) to prevent bubbles. The ice crystals were then stored in a homemade cold glove box (modified from a commercial freezer), and the storage temperature was between -5 and -10 °C. The sample preparation was all carried out in this cold glove box. The orientation of the ice crystals was checked with two crossed polarizers by using the birefringence of ice.

To prepare the (0001) basal surface, an ice crystal was first cut (by melting) and roughly oriented with its (0001) surface exposed. We then covered the ice crystal with a glass beaker with some pure ice in it and started to cool the ice crystal slightly with a

peltier cooler and let the crystal grow slowly from the water vapor. After typically one day of growth, hexagonal facets would appear on the crystal surface. This would allow us to have an accurate determination of the crystal orientation by looking at the reflection of a He-Ne laser beam from the hexagonal facets.

After finding the desired orientation, an ice crystal was "glued" (by melting and refreezing) to a clean fused silica substrate with the ice crystal's c-axis oriented perpendicularly to the substrate (miscut less than 2°). Another fused silica plate, which had been coated with an octadecyltrichlorosilane (OTS) monolayer [52], was heated and brought in contact with the other side of the ice crystal. A bubble-free fused silica/OTS/ice interface was formed by melting and regrowing a thin layer of ice crystal near the OTS-coated fused silica plate. Finally the sample was put in a sealed cold chamber (Fig. 2.6) filled with ambient pressure air and brought to the SFG optical bench. The ice chamber was made of copper and could be cooled to 173 K with an accuracy of 0.1 K. After cooling and waiting for the ice sample to reach thermal equilibrium with the chamber, the OTS-coated fused silica plate was separated from the ice sample by a mechanical device inside the chamber, leaving a smooth (0001) ice surface in equilibrium with the saturated water vapor in the sealed chamber. Such an ice surface preparation procedure is similar to that described in the glancing angle X-ray diffraction experiment [34] except that we used an OTS monolayer on the fused silica plate to make it hydrophobic and therefore easy to separate from the ice crystal.

Since air was present in the ice chamber, the vapor/ice (or vapor/water) interface that we studied could be called an air/ice (or air/water) interface as well. Here we will not
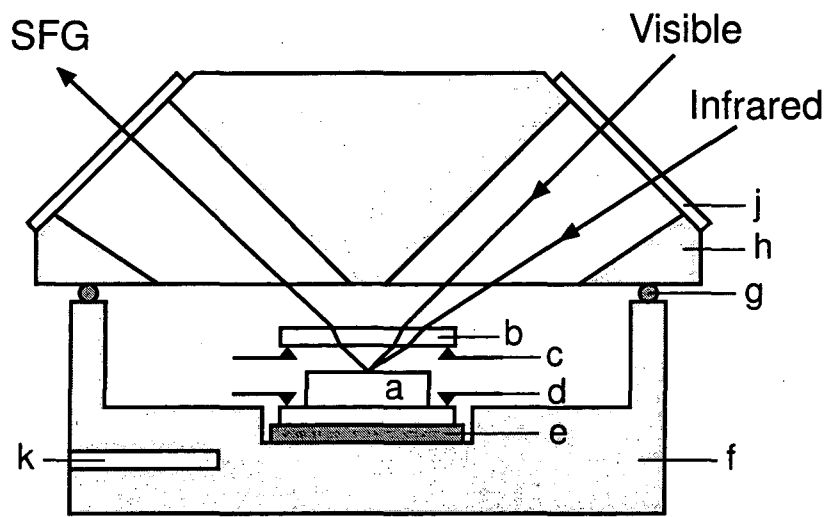
Figure 2.6: Schematic drawing of the ice chamber. (a)Single-crystal ice sample frozen to a fused silica plate at the bottom. (b)OTS-coated fused silica plate mechanically separated from the ice crystal. (c)Stainless steel levers that lift up the OTS-coated silica plate. (d)Stainless steel clamps that secure the bottom silica plate. (e)Glass color filter to absorb the transmitted visible input pulse. (f)Copper chamber cooled with cold nitrogen gas (cooling stage not shown). (g)O-ring. (h)Chamber cover made of Plexiglas. (j)Fused silica windows. (k)Omega Pt100 platinum resistance thermometer.

distinguish the subtle difference. Besides the vapor/ice interface, we also studied the interfaces between ice and fused silica plates which were either coated with OTS (hydrophobic) or uncoated (hydrophilic). These two interfaces will be called the silica/OTS/ice interface (Sec. 2.5.1) and the silica/ice interface (Sec. 2.5.2), respectively.

The SFG setup has been described in Sec. 1.2. One special precaution in the ice experiment is to avoid laser heating and damage. In the strong infrared absorption range of ice (2900 cm^{-1} to 3570 cm^{-1}), the infrared input pulse energy was reduced to about 20 μJ to avoid laser heating. Furthermore, the sample chamber was put on a computer-controlled two-dimensional raster stage to prevent input pulses from repeatedly hitting the same spot. With such precautions, the SFG output was found to be linearly proportional to the infrared input, indicating negligible laser heating or damage (see Sec. 2.6.1 for more

discussion on the effect of laser heating).

2.4 Study of the vapor(air)/ice interface

2.4.1 Experimental results

Shown in Fig. 2.7 is a typical SFG spectrum of the vapor/ice (0001) interface at 232 K in comparison with that of the liquid water surface at 293 K (an enlarged water spectrum can be found in Fig. 5.2). The polarization combination is *ssp*, which stands for *s*-, *s*-, and *p*-polarized sum-frequency output, visible input, and infrared input, respectively. The SFG output was calibrated against a reference *z*-cut quartz crystal (Sec. 1.3.2), yielding the spectra of $|\chi^{(2)}_{\text{eff}}|^2$ in MKS units, and the reflection loss of the windows on the ice chamber has also been corrected. As seen in Fig. 2.7, the spectrum of the ice surface is dominated by a strong but relatively broad peak at $\sim$3150 cm^{-1} that resembles the main OH stretch peak observed in the Raman spectrum of ice I$_h$ [53]. This peak is associated with the bonded OH stretching modes in the hydrogen bonding lattice. Unlike linear vibrational spectroscopy, in which the area under a resonant peak closely corresponds to the number of contributing oscillators, in the SFG spectrum the intensity or area of a resonant peak is very sensitive to the degree of order. This explains why the intensity of the bonded OH peak from the vapor/ice interface appears to be more than 30 times higher than that from the vapor/water interface, which is not the case in the infrared absorption and Raman spectra of ice and water. Besides the bonded OH peak, the SFG spectra in Fig. 2.7 also exhibit a sharp peak around 3695 cm^{-1} associated with the stretch vibration of the free OH (or dangling OH) bonds protruding from the surfaces [41].
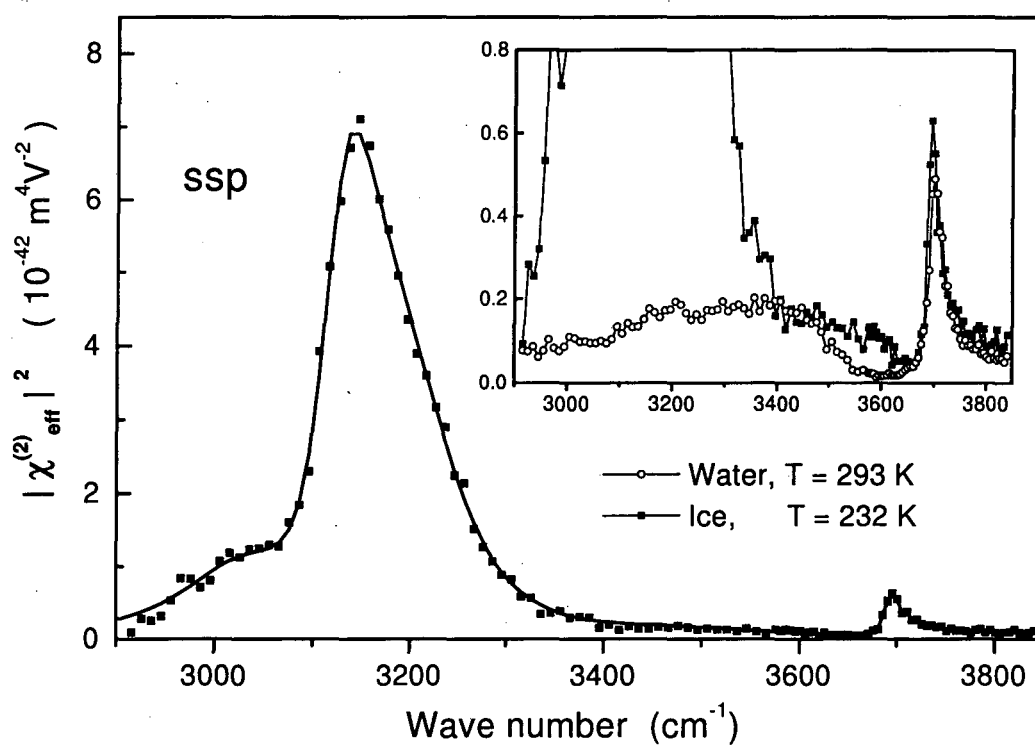
Figure 2.7: SFG spectra of the vapor/ice (0001) interface at 232 K (squares) and the vapor/water interface at 293 K (circles). The polarization combination is *ssp*.

Figures 2.8, 2.9 and 2.10 display the temperature dependence of the SFG spectra of the vapor/ice (0001) interface with different polarization combinations. In Fig. 2.8, the bonded OH peak decreases as the temperature increases but remains significantly different from that of liquid water (shown in the inset of Fig 2.7). Figure 2.8 also shows a small frequency shift of the bonded OH peak as the temperature increases, which is consistent with the temperature dependence of the bonded OH stretch frequency measured by Raman spectroscopy [54]. At this point, we do not know how the temperature dependence of the bonded OH peak in SFG is related to the appearance and change of the quasi-liquid layer on the ice surface. A molecular dynamics calculation is probably needed to find the answer.

The free OH peak in the SFG spectra of the ppp polarization combination (Fig. 2.9) exhibits a dramatic temperature dependence. The free OH peak is a feature that belongs to the vapor/ice interfacial layer and therefore can be used to characterize the surface structure. Figure 2.11 displays a set of ssp and ppp spectra of the free OH peak for the vapor/ice interface at different temperatures. The solid lines Fig. 2.11 are fits to the spectra using

$$\chi_{\text{eff}}^{(2)}(\omega_2) = \chi_{\text{NR,eff}}^{(2)} + \sum_q \frac{A_{q,\text{eff}}}{\omega_2 - \omega_q + i\Gamma_q} . \tag{2.10}$$

The fitting parameters $A_{q,\text{eff}}(ssp)$, $A_{q,\text{eff}}(ppp)$, ω_q and Γ_q for the free OH stretch mode are plotted in Fig. 2.12 and Fig. 2.13 as functions of temperature (including many other temperatures not shown in Fig. 2.11). Note that fitting the spectra with Eq. (2.1) could yield $|A_{q,\text{eff}}|$ but not the sign. The relative sign of $A_{q,\text{eff}}(ssp)$ and $A_{q,\text{eff}}(ppp)$ was measured by the interference between ssp and ppp using mixed polarizations for the visible input and SFG output (an example of such a relative phase measurement can be found in Fig. 3.6).
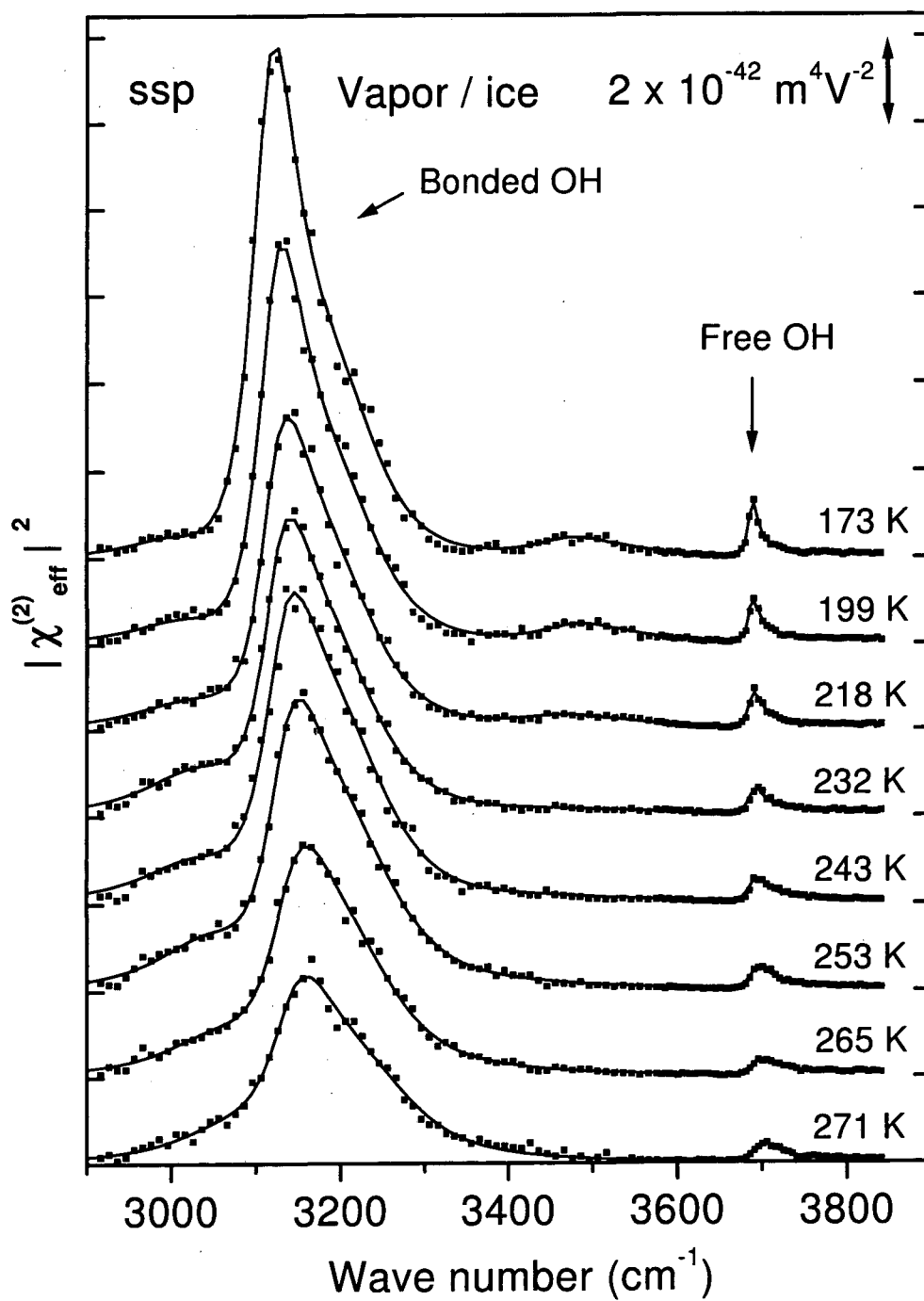
Figure 2.8: SFG spectra of the vapor/ice (0001) interface at various temperatures. The polarization combination is *ssp*.
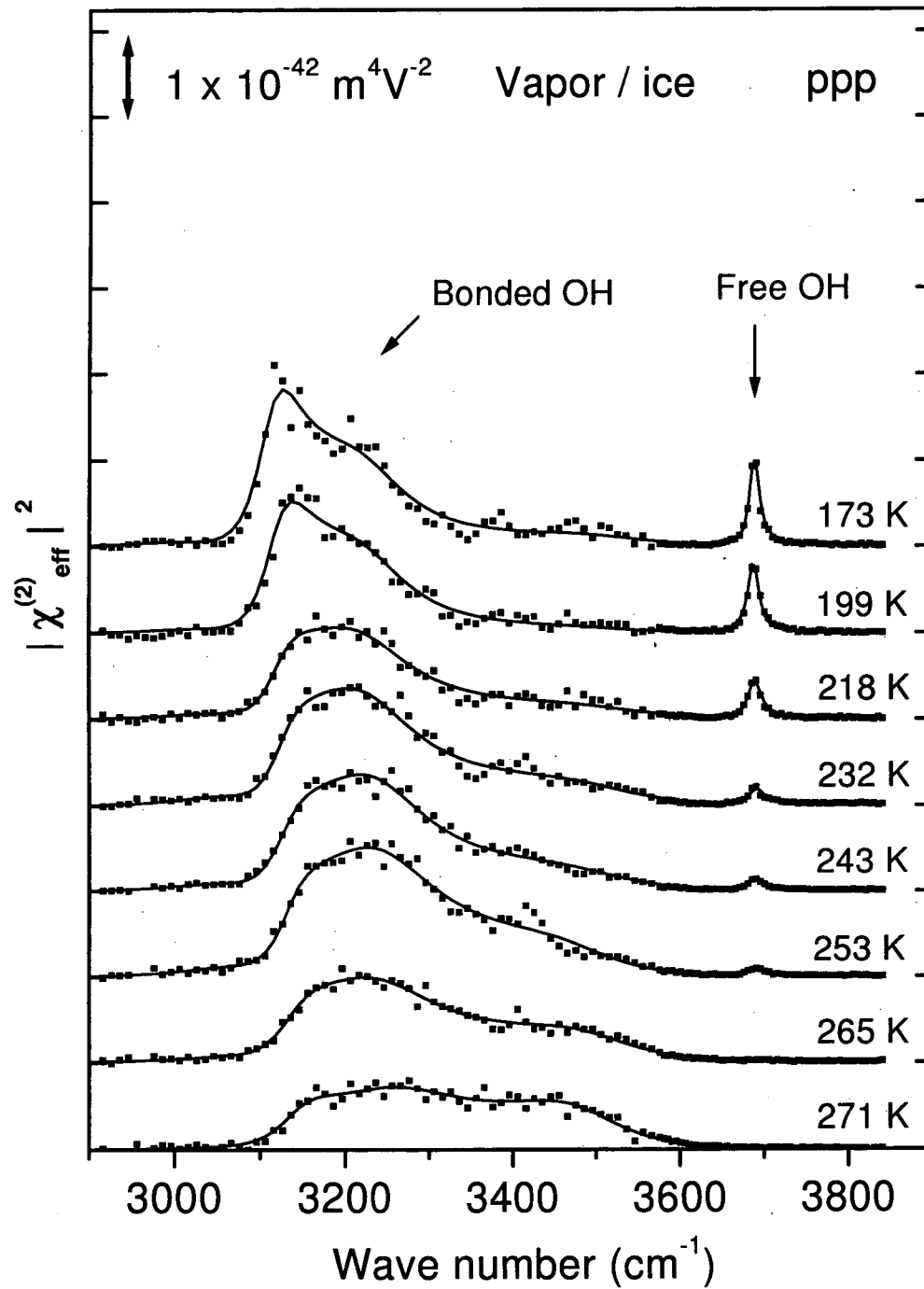
Figure 2.9: SFG spectra of the vapor/ice (0001) interface at various temperatures. The polarization combination is *ppp*.
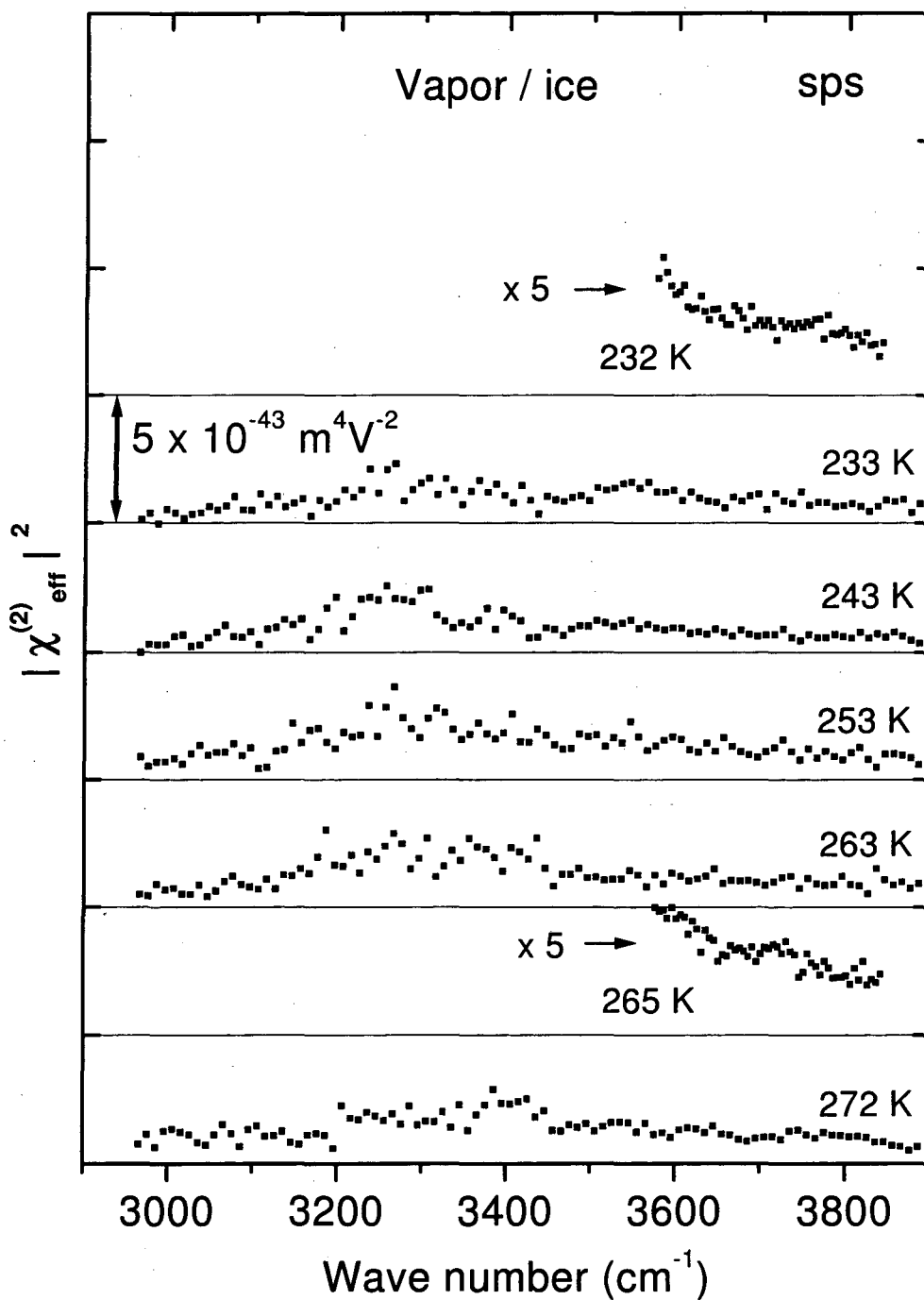
Figure 2.10: SFG spectra of the vapor/ice (0001) interface at various temperatures. The polarization combination is *sps*.
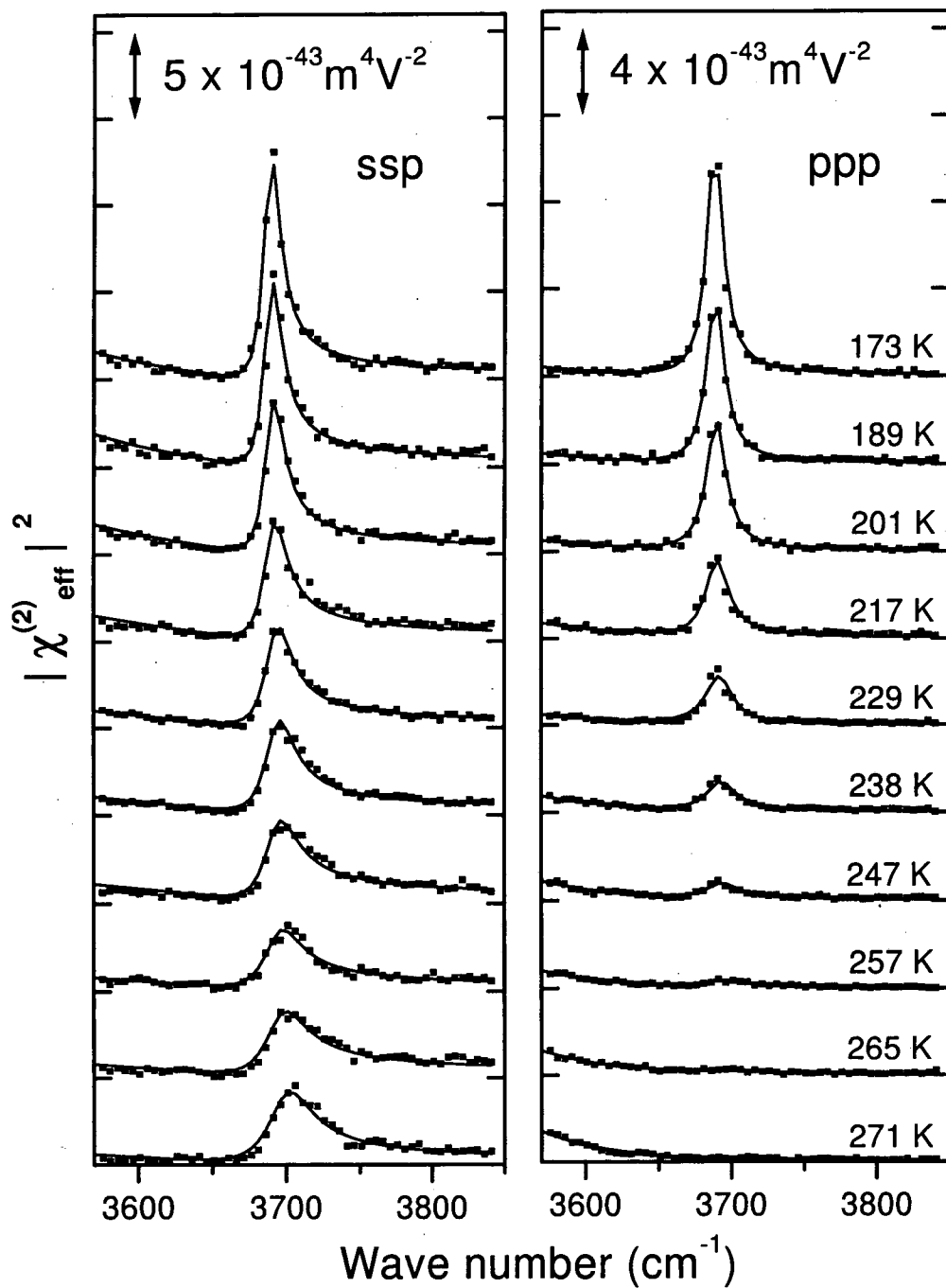
Figure 2.11: SFG spectra of the free OH stretch mode for the vapor/ice (0001) interface at various temperatures. The polarization combinations are *ssp* and *ppp*.
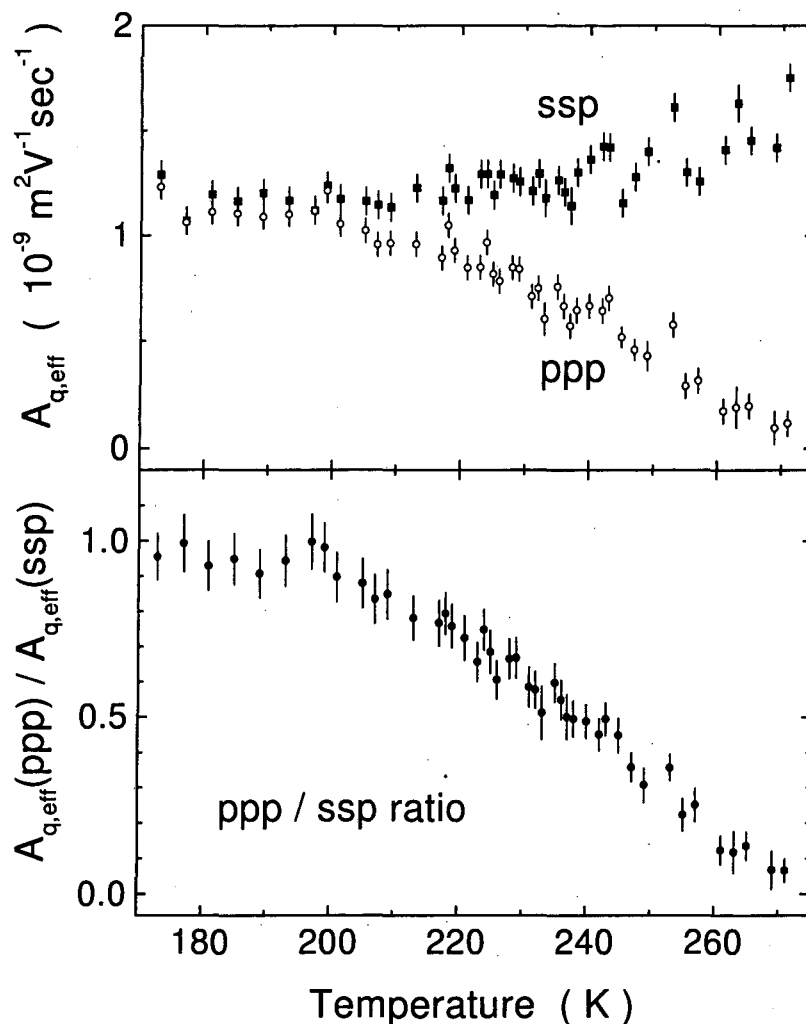
Figure 2.12: Amplitudes $A_{q,\text{eff}}(ssp)$ and $A_{q,\text{eff}}(ppp)$ and their ratio for the free OH stretch mode at the vapor/ice (0001) interface obtained from fitting the spectra in Fig. 2.11.

$A_{q,\text{eff}}(ssp)$ and $A_{q,\text{eff}}(ppp)$ were found to have the same sign.

In Fig. 2.12, $A_{q,\text{eff}}(ssp)$ and $A_{q,\text{eff}}(ppp)$ display relatively large fluctuations. This is because the spectra for different temperatures were obtained from different samples on different days. Although proper normalization methods were used (Sec. 1.2), some uncontrolled experimental conditions such as the humidity variation in the lab could result in a relatively large uncertainty in the absolute SFG peak intensity (see Fig. 1.2 for the infrared
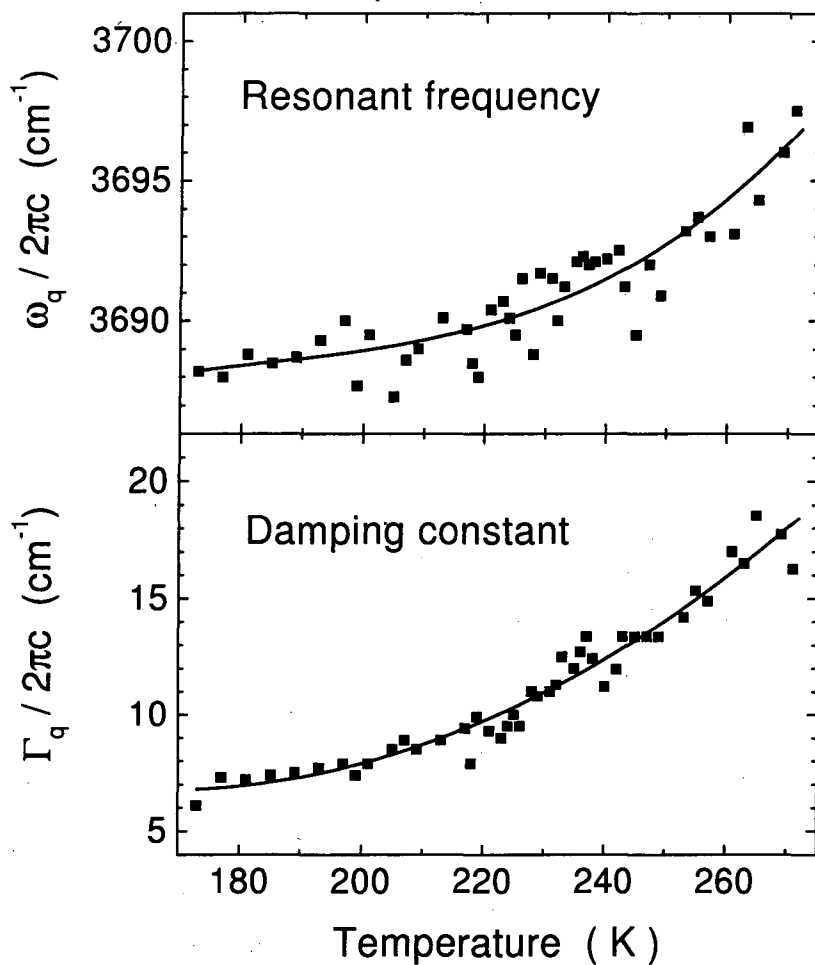
Figure 2.13: Resonant frequency and damping constant for the free OH stretch mode at the vapor/ice (0001) interface obtained from fitting the spectra in Fig. 2.11. The solid lines are guides to the eye.

absorption due to the water vapor in the infrared beam path). However, these conditions affect $A_{q,\text{eff}}(ssp)$ and $A_{q,\text{eff}}(ppp)$ in a similar way and, therefore, have less effect on the ratio of the two. It can be seen in Fig. 2.12 that the fluctuations of $A_{q,\text{eff}}(ssp)$ and $A_{q,\text{eff}}(ppp)$ are correlated, and the ratio displays smaller fluctuations.

From the values of $A_{q,\text{eff}}(ssp)$ and $A_{q,\text{eff}}(ppp)$ and their ratio in Fig. 2.12 we can deduce an approximate orientational distribution for the free OH bonds. The ratio $A_{q,\text{eff}}(ppp)/A_{q,\text{eff}}(ssp)$ remains constant at temperatures below 200 K and decreases continuously as the temperature increases. This indicates that the vapor/ice interface undergoes a continuous structural change which starts around 200 K.

2.4.2 Analysis of the free OH bonds

To proceed with a more quantitative analysis, we must first verify our theoretical speculations regarding the symmetry of the (0001) surface of ice I_h. If the surface indeed has a 6-fold symmetry, from our theory in Sec. 2.2.2, we do not expect to observe any SFG signal with polarization combinations *sss*, *pps*, *spp* and *psp*. The SFG spectra of the vapor/ice interface with these forbidden polarization combinations are presented in Fig. 2.14, in comparison with the allowed polarization combinations *ssp*, *ppp* and *sps*. As we had predicted, there was indeed no SFG signal with the forbidden polarization combinations.

We must also determine whether the slow-motion limit [Eq. (2.8)] or the rapid-motion limit [Eq. (2.9)] better describes the dynamic nature of the vapor/ice interface. In Chap. 5 we will show that the strong evidence of motional averaging effect on the free OH stretch mode is the unexpectedly weak SFG signal with the *sps* polarization combination.
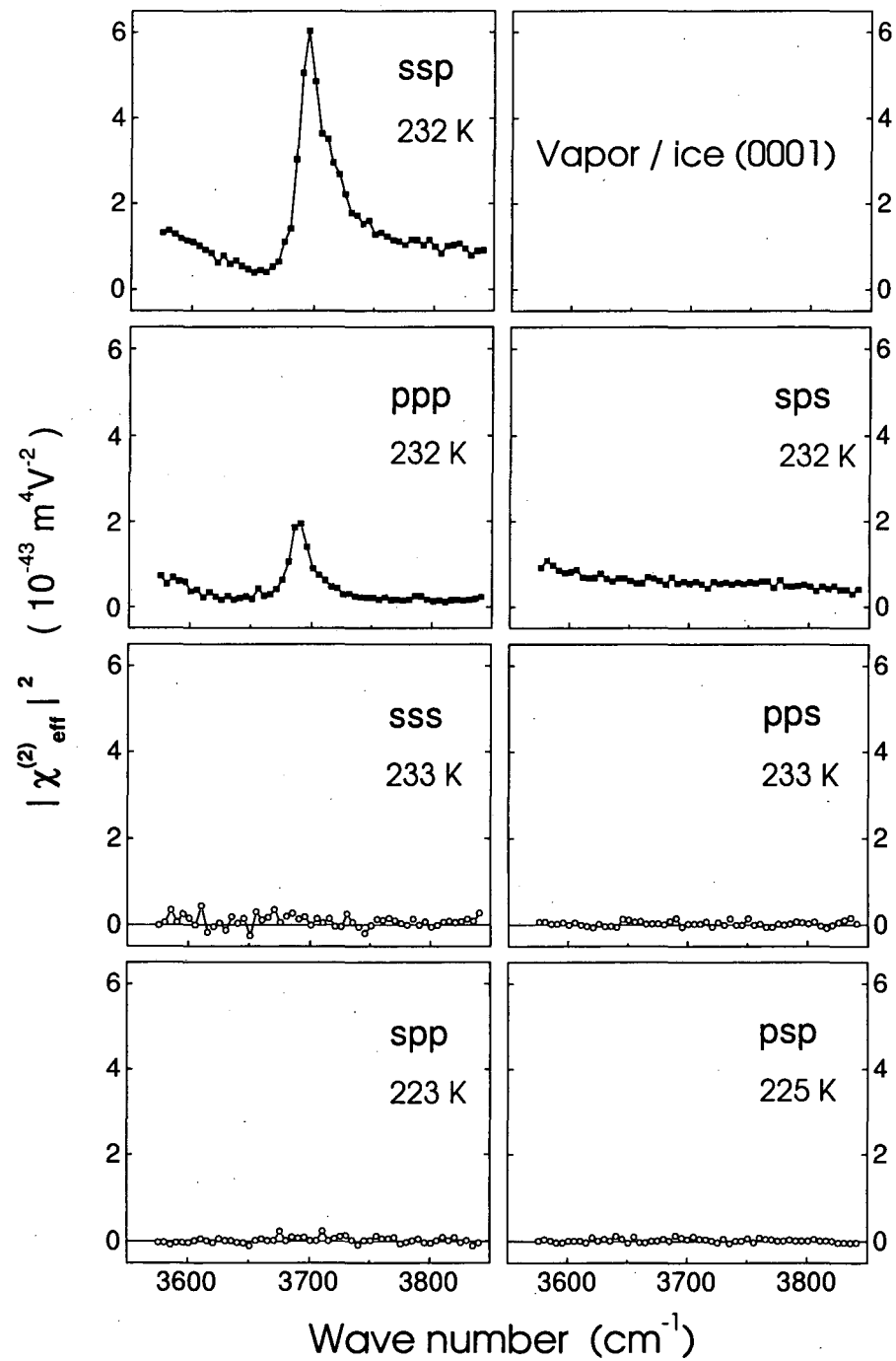
Figure 2.14: SFG spectra of the vapor/ice (0001) interface with different polarization combinations, of which the lower four are forbidden by the hexagonal symmetry.

Figure 2.10 shows the *sps* SFG spectra of the vapor/ice interface, in which the resonant signal of the free OH stretch is hardly detectable for all temperatures. This resembles the case of the vapor/water interface (Fig. 5.2) and indicates that the rapid-motion limit is a better approximation for describing the orientational fluctuations of the free OH bonds at the vapor/ice interface. From Eq. (2.9) with the rapid-motion approximation, we find

$$A_{q,xxz} = A_{q,yyz} = \frac{1}{2}N_S \left[a_{\zeta\zeta\zeta}\left(1 - \langle cos^2\theta \rangle\right) + a_{\xi\xi\zeta}\left(1 + \langle cos^2\theta \rangle\right)\right]\langle cos\theta \rangle , \quad (2.11)$$

$$A_{q,zzz} = N_S \left[a_{\zeta\zeta\zeta}\langle cos^2\theta \rangle + a_{\xi\xi\zeta}\left(1 - \langle cos^2\theta \rangle\right)\right]\langle cos\theta \rangle , \quad (2.12)$$

$$A_{q,xzx} = A_{q,yzy} = 0 . \quad (2.13)$$

Here N_S is the surface density of the free OH bonds; the angle brackets represent the ensemble average over $f(\theta)$, the polar orientational distribution of the free OH bonds in the tilt angle θ ($0 \le \theta \le \pi/2$) from the surface normal (the azimuthal distribution is isotropic); and $a_{\zeta\zeta\zeta}$ and $a_{\xi\xi\zeta} = a_{\eta\eta\zeta}$ are the two independent nonvanishing hyperpolarizability elements of a free OH bond (values listed in Eq. (2.7)).

If we simply assume a truncated flat distribution for $f(\theta)$,

$$f(\theta) = \text{constant} \quad \text{for } 0 \le \theta \le \theta_M ,$$

$$f(\theta) = 0 \quad \text{for } \theta > \theta_M ,$$

then we can calculate $A_{q,xxz}$ and $A_{q,zzz}$ for each value of θ_M using Eqs. (2.11) and (2.12), from which we can further calculate $A_{q,\text{eff}}(ssp)$ and $A_{q,\text{eff}}(ppp)$ through the relation

$$A_{q,\text{eff}} = [\mathbf{L}(\omega_s)\cdot\hat{\mathbf{e}}_s]\cdot\mathbf{A}_q : [\mathbf{L}(\omega_1)\cdot\hat{\mathbf{e}}_1][\mathbf{L}(\omega_2)\cdot\hat{\mathbf{e}}_2] , \quad (2.14)$$

where $\hat{\mathbf{e}}_i$ is the unit polarization vector of the field at ω_i and $\mathbf{L}(\omega_i)$ is the tensorial Fresnel factor (Appendix B). The values of the Fresnel factors used in this calculation are listed

Table 2.1: Calculated Fresnel factors for the vapor/ice interface. z is along the sample surface normal, with the xz plane being the light incidence plane. β is the incidence angle of the input or output beam. ϵ' is the effective dielectric constant of the surface monolayer.

	ω_s	ω_1	ω_2
λ	444 nm	532 nm	2.7 μm
n	1.31	1.31	1.18
β	46.8°	45°	57°
L_{xx}	.96	.95	1.04
L_{yy}	.77	.78	.79
L_{zz}	$1.04/\epsilon'_s$	$1.05/\epsilon'_1$	$.96/\epsilon'_2$
$e_x L_{xx}$ (p)	-.66	.67	.57
$e_y L_{yy}$ (s)	.77	.78	.79
$e_z L_{zz}$ (p)	$.76/\epsilon'_s$	$.74/\epsilon'_1$	$.80/\epsilon'_2$

in Table 2.1. The results of $A_{q,\text{eff}}(ssp)$ and $A_{q,\text{eff}}(ppp)$ from the calculation are presented in Fig. 2.15 as functions of θ_M. Note that we had some unknown (therefore adjustable) parameters in this calculation. One parameter is the dielectric constant ϵ'_i of the surface monolayer, as shown in Table 2.1, and another one is a common factor $l_\parallel(\omega_s)l_\parallel(\omega_1)l_\parallel(\omega_2)$, which has been neglected in Eq. (2.9). The physical implications of ϵ'_i and $l_\parallel(\omega_i)$ are discussed in Appendix C. In our calculation we assumed that $\epsilon'_s = \epsilon'_1$ (neglecting dispersion in the visible) and adjusted the value of ϵ'_1 such that the calculated ratio $A_{q,\text{eff}}(ppp)/A_{q,\text{eff}}(ssp)$ for $\theta_M = 0$ matches the experimentally deduced value ~0.95 at low temperatures (Fig. 2.12). At such low temperatures (≤ 200 K), the free OH bonds at the vapor/ice (0001) interface presumably have a δ-function-like orientational distribution perpendicular to the surface. From this we found $\epsilon'_s = \epsilon'_1 = 1.31$, which agrees very well with the estimate obtained from the model presented in the appendix of Ref. [55] [Eq. (C.6) gives $\epsilon'_s = \epsilon'_1 = 1.29$ for ice]. The other parameters ϵ'_2 and $l_\parallel(\omega_s)l_\parallel(\omega_1)l_\parallel(\omega_2)$ cannot be determined experimentally, but fortunately, they have no effect on the results in Fig. 2.15 because they all cancel out as we normalize the values of $A_{q,\text{eff}}(ssp)$ and $A_{q,\text{eff}}(ppp)$ with respect to the value of $A_{q,\text{eff}}(ssp)$ at
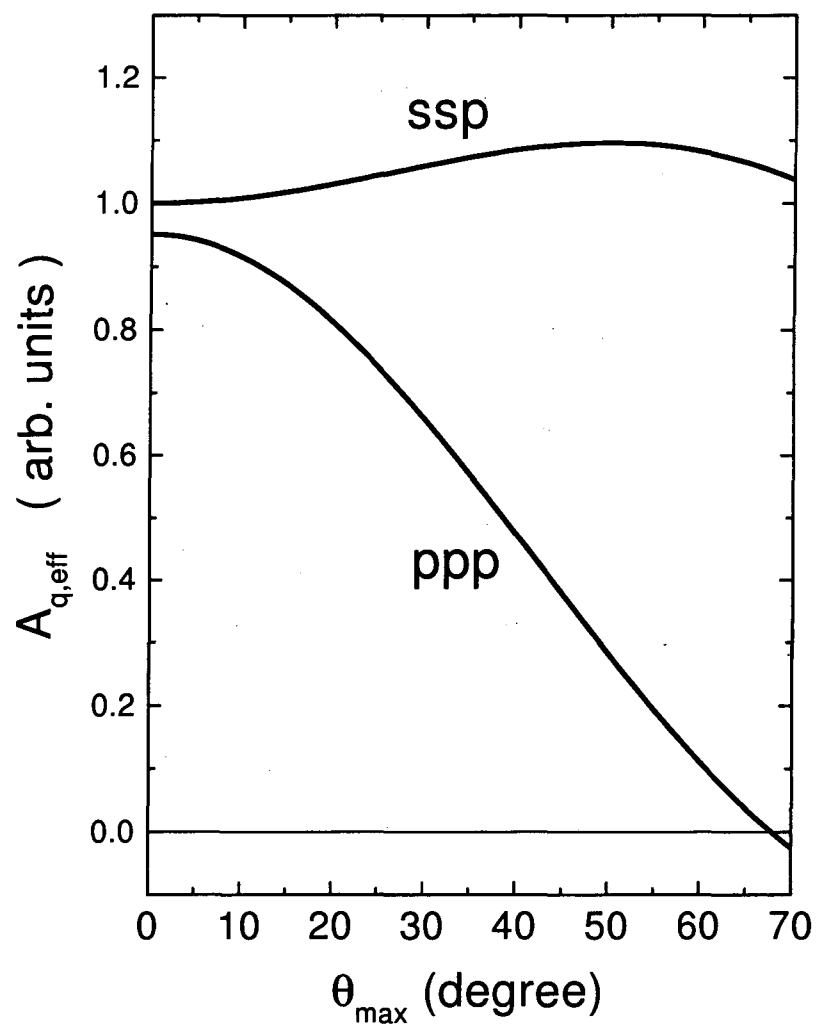
Figure 2.15: Theoretical calculation of the mode amplitudes $A_{q,\text{eff}}(ssp)$ and $A_{q,\text{eff}}(ppp)$ in the rapid-motion limit for the free OH bonds at the vapor/ice (0001) interface. All values are normalized with respect to $A_{q,\text{eff}}(ssp)$ at $\theta_{\text{M}} = 0$.

$\theta_M = 0$. ϵ'_2 and $l_\parallel(\omega_s)l_\parallel(\omega_1)l_\parallel(\omega_2)$ would still affect our calculation of the absolute amplitude $A_{q,\text{eff}}$. For this we used the model in Ref. [55] and obtained an estimate $\epsilon'_2 \approx 1.18$ and $l_\parallel(\omega_s)l_\parallel(\omega_1)l_\parallel(\omega_2) \approx 1.32$.

With these parameters we calculated the absolute amplitude $A_{q,\text{eff}}(ssp)$ for $\theta_M = 0$. From Eqs. (2.9) and (2.14), we have

$$A_{q,\text{eff}}(ssp) = N_S l_\parallel(\omega_s)l_\parallel(\omega_1)l_\parallel(\omega_2)L_{yy}(\omega_s)L_{yy}(\omega_1)L_{zz}(\omega_2)(\sin\beta_2)a_{q,\eta\eta\zeta} . \quad (2.15)$$

The surface density of free OH bonds on the ice (0001) surface is one quarter of the surface density of H_2O molecules because only the top half bilayer has broken hydrogen bonds and only half of the broken hydrogen bonds are dangling OH bonds (Fig. 2.2). The surface density of H_2O molecules in the top bilayer of the ice (0001) surface is 1.14×10^{15} cm^{-2}, and one quarter of this value gives $N_S = 2.8 \times 10^{14}$ cm^{-2} (or 2.8/nm^2). Equation (2.15) then yields

$$A_{q,\text{eff}}(ssp) = 1.29 \times 10^{-9} \text{ m}^2\text{V}^{-1}\text{sec}^{-1} .$$

The measured $A_{q,\text{eff}}(ssp)$ at low temperatures is about 1.2×10^{-9} m^{2}V^{-1}sec^{-1} (Fig. 2.12). The agreement between theory and experiment here is truly remarkable considering the uncertainties of the input parameters that we used for the calculation.

As we increase the temperature, a comparison of the theory (Fig. 2.15) and the experiment (Fig. 2.12) yields the maximum bond tilt angle θ_M as a function of temperature, as shown in Fig. 2.16(a). Also shown in Fig. 2.16(a) is θ_M of the free OH bonds at the vapor/water interface obtained in a similar way from the SFG spectra of the vapor/water interface (Fig. 2.17).
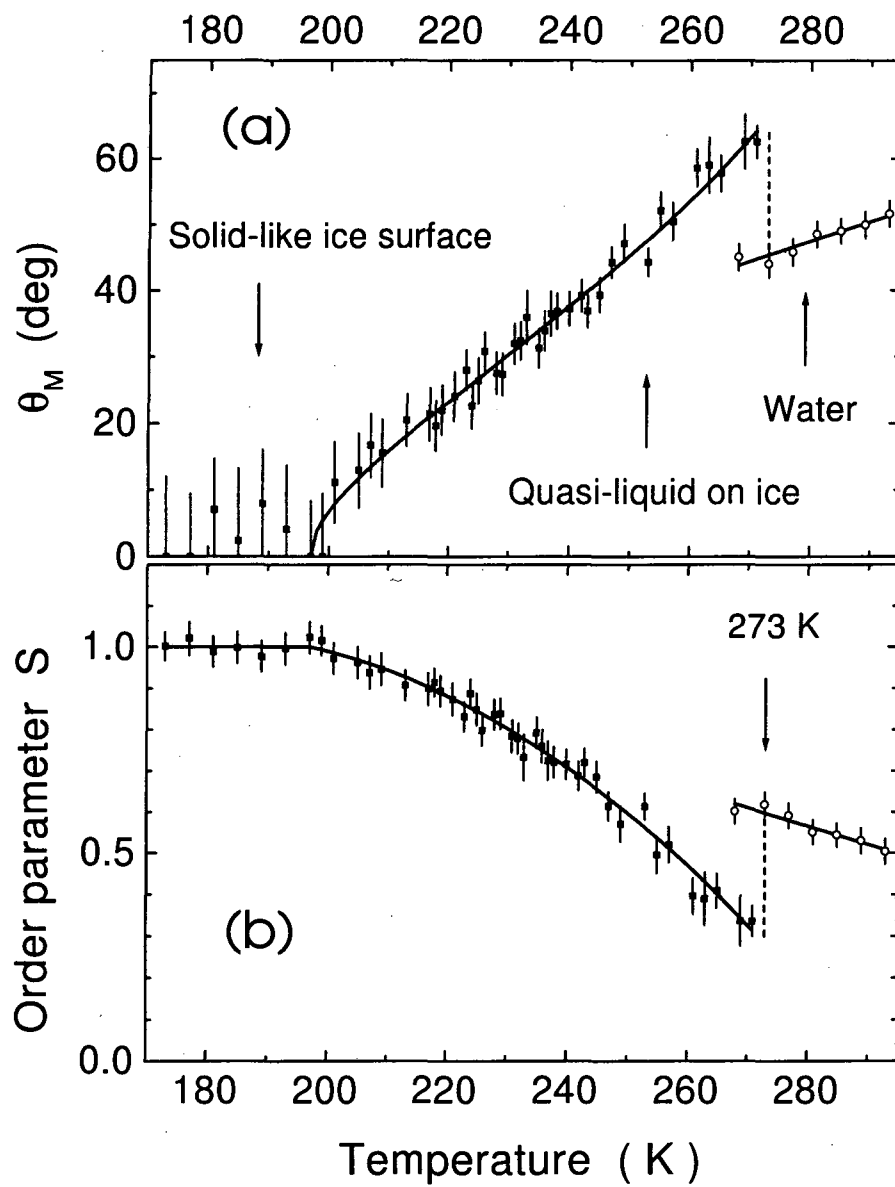
Figure 2.16: (a)Maximum tilt angle θ_M, and (b)orientational order parameter S for the free OH bonds at the vapor/ice and vapor/water interfaces. The solid lines are guides to the eye.
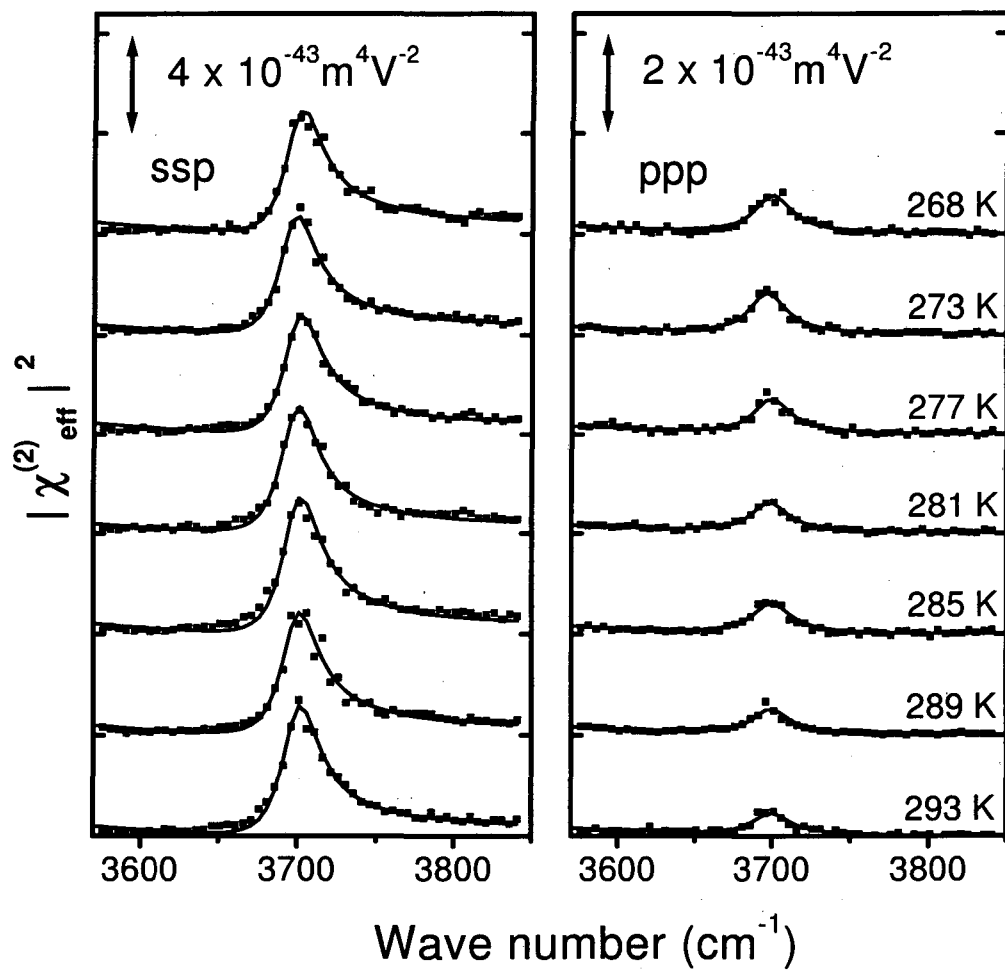
Figure 2.17: SFG spectra of the free OH stretch mode for the vapor/water interface at various temperatures. The polarization combinations are *ssp* and *ppp*. Note that at 268 K water is supercooled.

We can convert θ_M into a more meaningful orientational order parameter S defined as

$$S = \frac{3\langle\cos^2\theta\rangle - 1}{2} \tag{2.16}$$

to describe the ordering of the free OH bonds. If $\theta_M \to 0$, then $S \to 1$ corresponding to perfect orientational order. The other extreme is $\theta_M = \pi/2$ leading to $S = 0$ for total disorder. One advantage of using S instead of θ_M is that S does not depend on our assumptions for the distribution function $f(\theta)$. This can be seen from Eqs. (2.11) and (2.12), from which the ratio $A_{q,zzz}/A_{q,yyz}$ depends only on $\langle\cos^2\theta\rangle$ regardless of the actual shape of $f(\theta)$. The values of S are displayed in Fig. 2.16(b). S is close to 1 below 200 K and drops appreciably as the temperature increases above 200 K.

2.4.3 Implications for surface melting of ice

An apparent onset of surface melting can be defined as the point at which surface disorder becomes detectable. Our experiment indicates that the onset of surface melting of ice is around ~200 K, below which the surface monolayer is still solid but above which it becomes increasingly disordered. Our onset temperature is lower than those obtained by other techniques. This is presumably because our SFG technique is more surface specific and sensitive to the disorder of the surface monolayer. For example, the recent measurement of x-ray scattering at glancing angles found that for the (0001) ice surface, the onset of surface melting was at 259.5 K ± 2.5 K, below which no surface melting could be observed [34]. However, the measurement did not have enough sensitivity to detect a few monolayers of the quasi-liquid. Extrapolation of the data to zero quasi-liquid layer thickness to obtain the

onset temperature for surface melting could yield too high a value.

The usual melting transition in the bulk is a first order phase transition, in which abrupt changes of physical properties are expected to occur. However, Fig. 2.16 shows that, within the experimental uncertainty, the decrease of the order parameter S of the vapor/ice interface is continuous. This indicates that the quasi-liquid layer has a temperature-dependent structure and suggests that there should be a structural variation across the quasi-liquid layer on the ice surface. This picture is consistent with the results of molecular dynamics simulations [23, 25] but different from the simple models of surface melting used in the analyses of many experimental results. The latter assume a quasi-liquid layer with uniform structural properties.

An interesting feature displayed in Fig. 2.16 is that near the bulk melting temperature (273 K), the order parameter S of the ice surface is even lower than that of the supercooled water surface. Although not physically impossible, this seems surprising and needs a good theoretical explanation. In any case, it indicates that the quasi-liquid layer on ice is different from the surface layer of water. There is a long-debated question whether surface melting of ice is complete or incomplete (i.e., whether the thickness of the quasi-liquid layer diverges or remains finite as the temperature approaches 273 K) [30]. Our result here favors the incomplete surface melting scenario because otherwise one would expect the surface structure of the quasi-liquid layer to approach that of normal water as the layer thickness diverges.

2.5   Study of other ice interfaces

2.5.1   Hydrophobic ice interface

A set of SFG spectra of a hydrophobic ice interface, the fused-silica/OTS/ice (0001) interface, at different temperatures are shown in Fig. 2.18. The spectra appear to be similar to those from the vapor/ice interface, with a strong and broad hydrogen-bonded OH peak and a sharp free OH peak. An additional sharp peak at $\sim$2940 cm^{-1} is associated with a CH stretch mode of the methyl groups on the OTS monolayer.

Figure 2.19 displays a set of SFG spectra for the free OH stretch in both *ssp* and *ppp* polarization combinations. Compared with the vapor/ice interface (Fig. 2.11), the free OH peak is shifted by $\sim$25 cm^{-1} to lower frequency due to the hydrophobic interaction with the OTS monolayer. Similar red shift of the free OD stretch at a hydrophobic D_2O ice interface has been reported before by infrared spectroscopy [56].

A major difference between the silica/OTS/ice and vapor/ice interfaces is that the free OH peak from the silica/OTS/ice interface remains very weak and hardly detectable for all temperatures with *ppp* polarization combination. With the same analysis we did for the vapor/ice interface, we came to the conclusion that the H_2O molecules at the silica/OTS/ice interface are disordered in orientation regardless of the temperature, presumably because of the roughness of the surface of the fused (amorphous) silica plate on a microscopic scale. As we separate this silica plate from the ice crystal, the exposed ice surface quickly relaxes to a microscopically flat surface which gives rise to a clear free OH peak with the *ppp* polarization combination (Fig. 2.11).
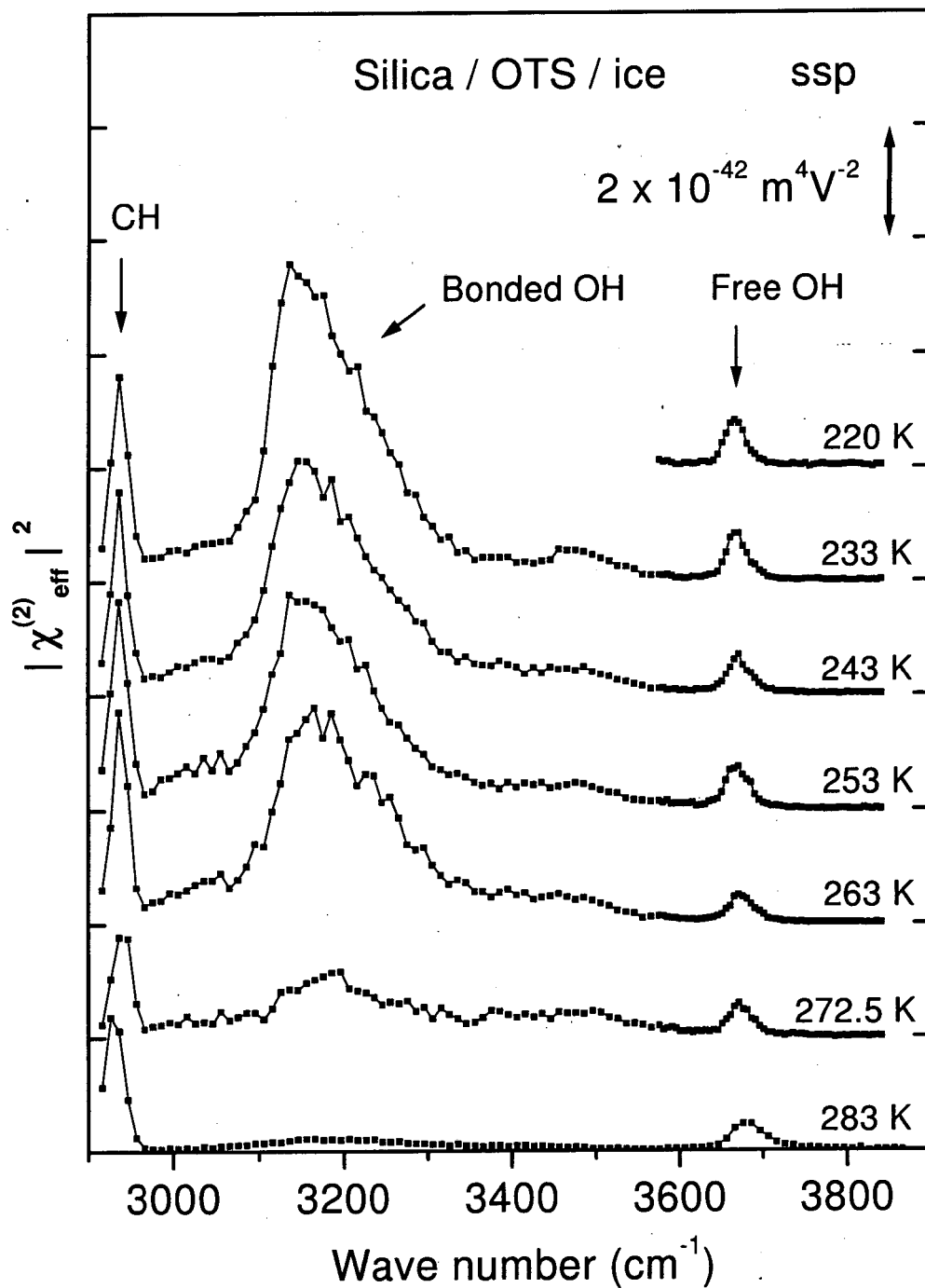
Figure 2.18: SFG spectra of the silica/OTS/ice (0001) interface at various temperatures, in comparison with the spectrum of the silica/OTS/water interface at 283 K. The polarization combination is *ssp*.
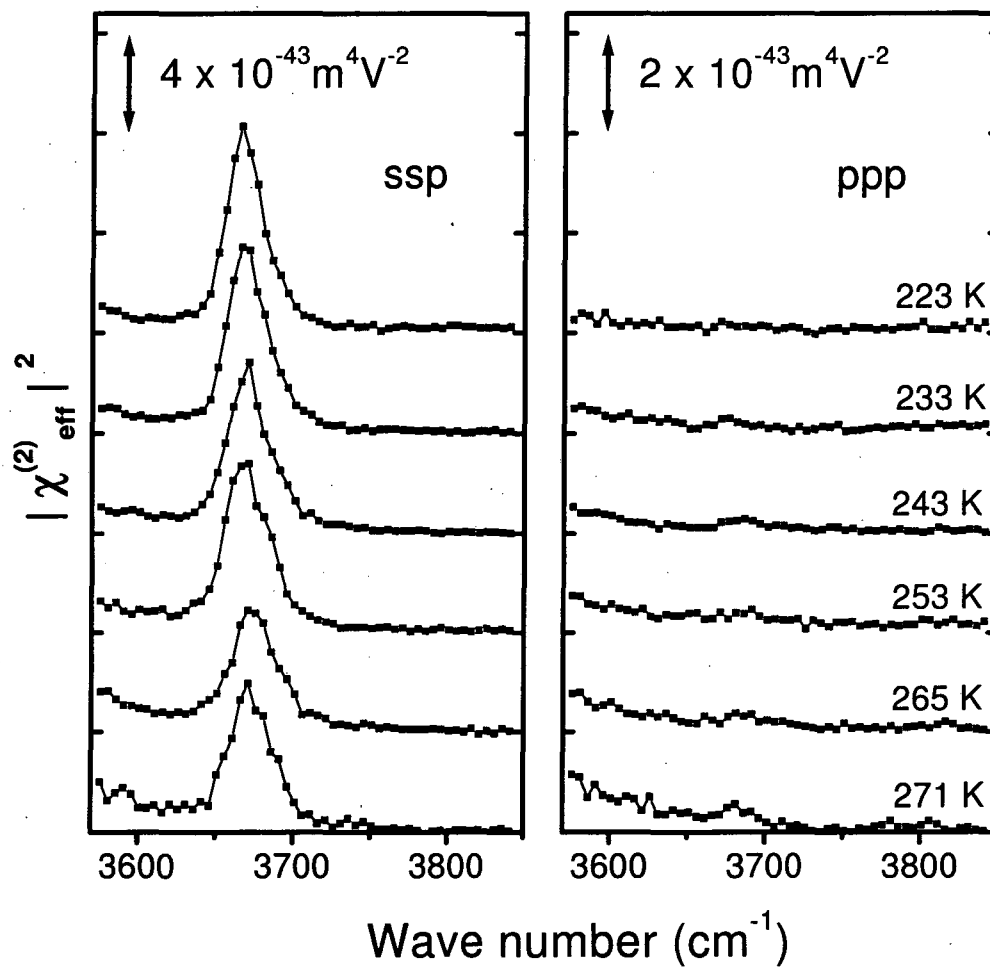
Figure 2.19: SFG spectra of the free OH stretch mode for the silica/OTS/ice (0001) interface at various temperatures. The polarization combinations are *ssp* and *ppp*.

2.5.2   Hydrophilic ice interface

In comparison with the hydrophobic ice interface, we also measured a hydrophilic ice interface by using a clean (uncoated) fused silica plate to replace the OTS-coated one. The silica plate was cleaned with acid, rinsed with deionized water and blown dry with nitrogen gas. Such a silica surface is known to be terminated by $\sim 5/nm^2$ SiOH (silanol) groups, which can form hydrogen bonds with water and thus make the surface hydrophilic [57]. The OH stretch of the silanol groups on a hydrophilic silica surface has been reported to be observable in the SFG spectrum [58].

The measured spectra of the silica/ice interface are presented in Fig. 2.20. The free OH peak has disappeared due to hydrogen bonding to the silanol groups on the silica surface, similar to the case of the silica/water interface [42].

The bonded OH peak, however, remains strong up to 272 K. In our experiment, we increased the sample temperature very slowly so that we could actually melt the silica/ice interface and form a thin layer of liquid water (denoted as 273^+ K in Fig. 2.20). An interesting transition was observed. As the interface started to melt, the bonded OH peak first broadened and decreased to a minimum, and then increased again. In the mean time another resonant peak around 3450 cm^{-1} emerged.

A typical silica/water spectrum was reported before [42], in which the relatively strong SFG signal of the bonded OH stretch was explained by polar ordering of the water molecules in the electric double layer created by the electric charge on the silica surface due to ionization of the silanol groups. Such an interpretation was verified by the variation of the SFG spectrum with the pH value of water. In this picture the silica surface is negatively
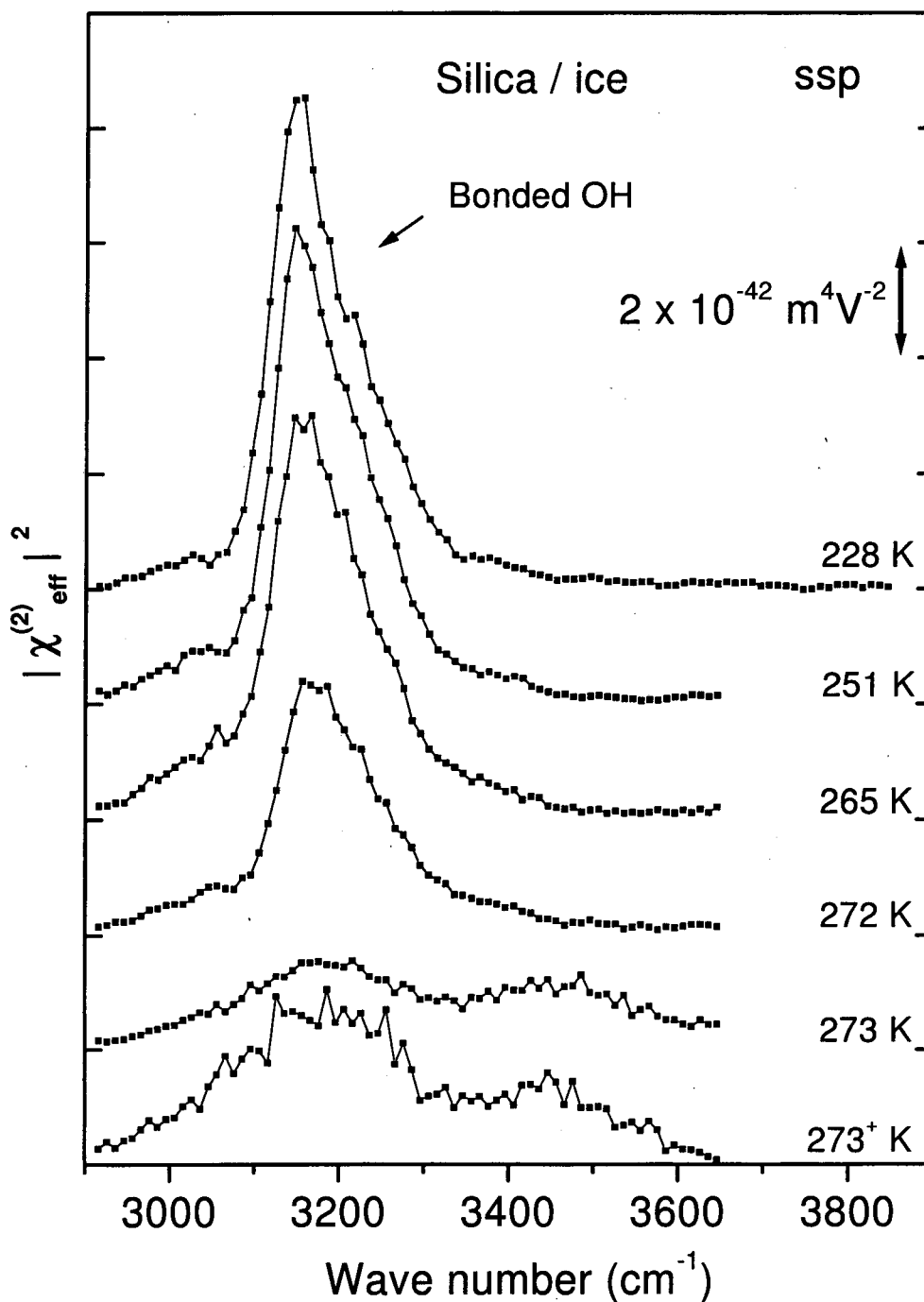
Figure 2.20: SFG spectra of the silica/ice (0001) interface at various temperatures. The spectrum at 273^+ K was taken when a thin layer of water had been formed at the interface. The polarization combination is *ssp*.
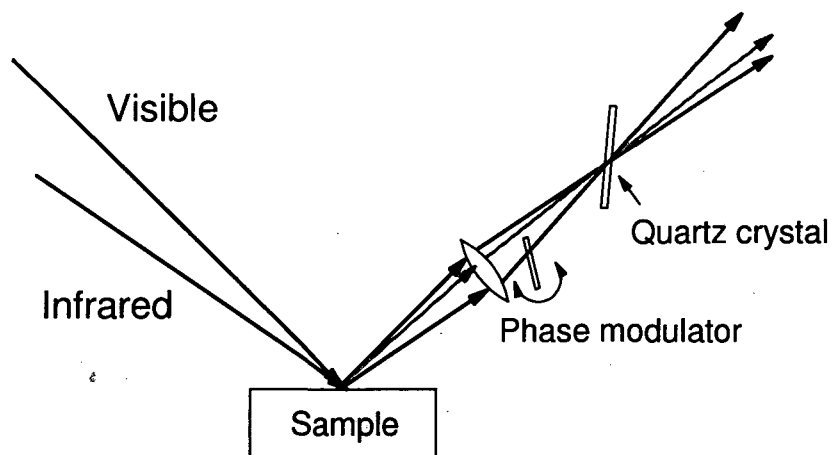
Figure 2.21: SFG phase measurement. Interference is achieved by focusing the three beams onto a thin nonlinear optical crystal (z-cut quartz, 50 μm thick), and the phase of the reflected infrared beam can be modulated by tilting a glass film in its optical path.

charged and causes the water molecules in the electric double layer to orient their OH bonds (or dipole moments) towards the silica surface. In the case of the silica/ice interface, an electric double layer does not exist, and the strong bonded OH signal can only be explained by a net bond orientation pointing towards ice. A flipping of the molecular orientation at the silica/water interface when melting occurs would explain the minimum intensity of the SFG signal. To confirm this interpretation, we performed a relative SFG phase measurement as illustrated in Fig. 2.21, based on the fact that the nonlinear susceptibility changes its sign when the average orientation of the molecules is inverted. This method was used previously to study the molecular orientation of water molecules in the electric double layer at the silica/water interface as the pH value changes [59]. By varying the phase of the reflected infrared beam, we obtained a modulation of SFG intensity due to the interference between the SFG signal from the sample and the signal generated from a reference nonlinear optical crystal. As we warmed the sample and changed it from silica/ice (253 K) into silica/water
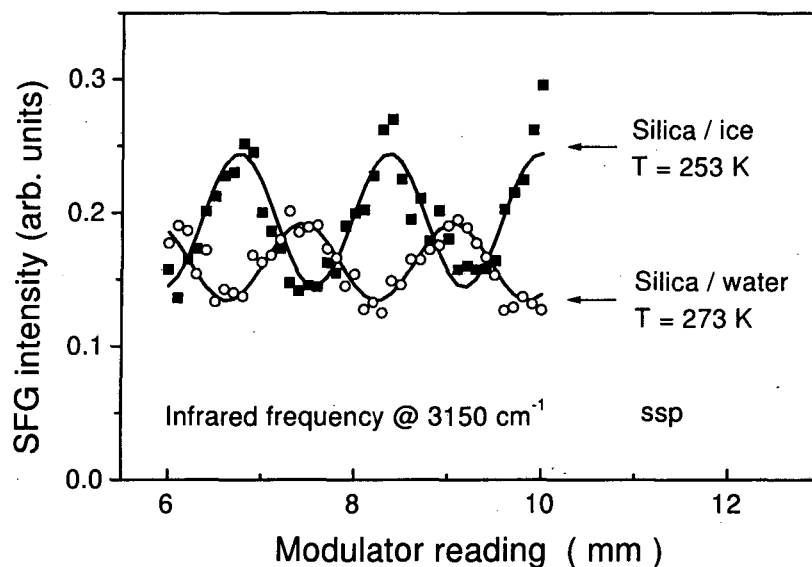
Figure 2.22: Out-of-phase interference patterns obtained from silica/ice and silica/water interfaces in the SFG phase measurement.

(273 K), the interference pattern had a $\sim$180 ° phase shift (Fig. 2.22), which confirmed that the hydrogen bonded OH bonds at the silica/ice and silica/water interfaces are indeed oriented in opposite directions.

Interestingly, the strong bonded OH peak at the silica/ice interface can be greatly enhanced by doping the ice crystal with a small amount of ammonia, as shown in Fig. 2.23. The ammonia-doped ice crystal was grown from an ammonia-water solution with a pH value of 11.0 at room temperature. The crystal growth rate was $\sim$2 μm/sec, twice as fast as the usual growth rate for growing pure ice crystals. Fast growth helps ammonia to incorporate into the ice crystal. A test sample was melted after growth to measure the actual doping concentration. The pH value of the melted test sample was 10.15, corresponding to a NH_3 doping concentration of $\sim$1 mM.

The enhancement of the bonded OH peak due to NH_3 can be explained as follows.
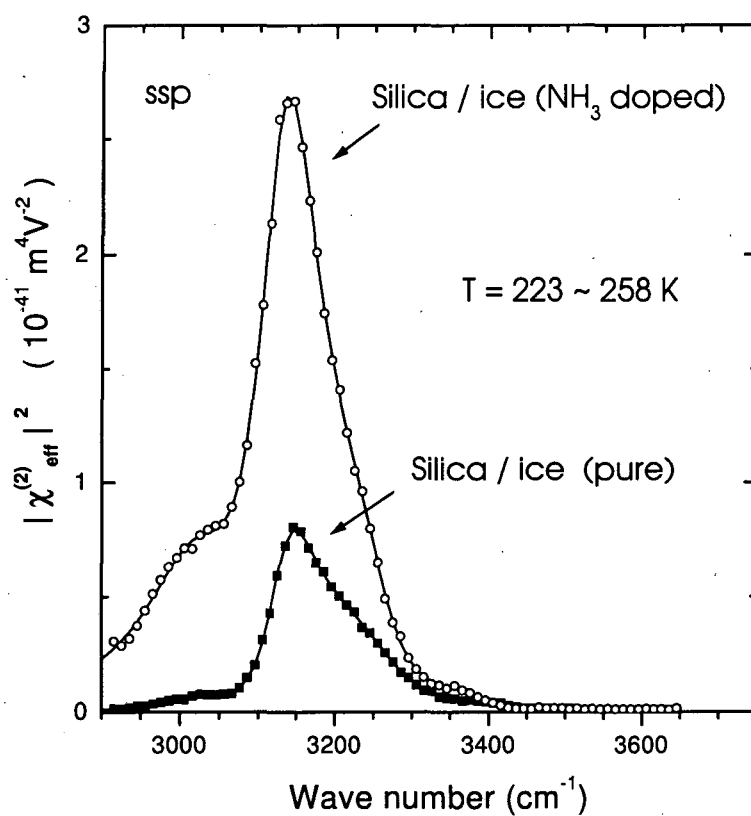
Figure 2.23: SFG spectra of the silica/ice interfaces with ammonia-doped and undoped ice crystals. The NH_3 molar concentration in the doped crystal is ~ 1 mM. Each spectrum is an average of several spectra in the temperature range 223-258 K to improve the signal to noise ratio.
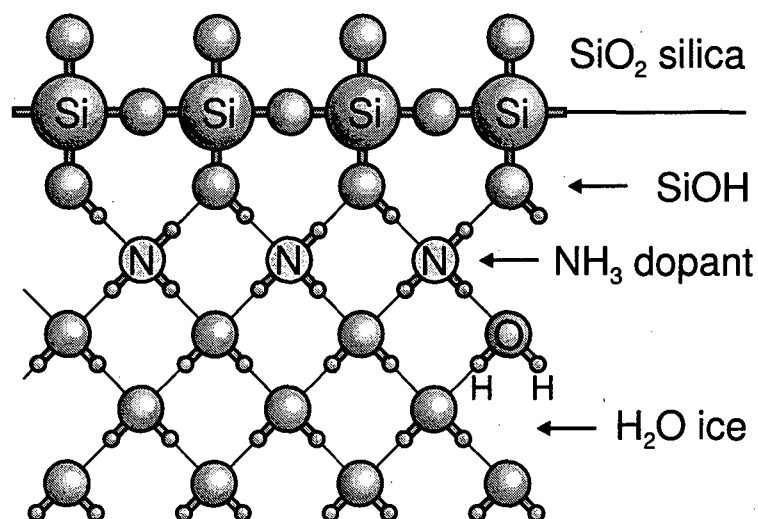
Figure 2.24: Two dimensional illustration of the NH₃ induced polar ordering of the H₂O molecules near the silica/ice interface. The surface density of NH₃ and the degree of polar ordering are exaggerated for clarity.

Since the silica/ice interface was formed by melting and refreezing the ice crystal, the interface was likely to have a much higher NH₃ concentration than the bulk. The NH₃ concentration at the interface was not high enough for a strong NH stretch peak to show up in the SFG spectrum (the NH symmetric stretch peak was reported to be at 3312 cm⁻¹ in the SFG spectrum from the ammonia-water solution surface [60]) but could still have a dramatic effect on the net orientation of the H₂O molecules near the silica/ice interface. As illustrated in Fig. 2.24, some NH₃ molecules may form strong hydrogen bonding with the silanol groups on the silica surface with the nitrogen atoms facing silica, resulting in an excessive number of protons (NH bonds) pointing into ice. Starting from these surface-anchored NH₃ molecules, the H₂O molecules will adopt the same orientation (with a net dipole moment pointing to the bulk ice) to obey the Bernal-Fowler ice rules [61] until Bjerrum defects (broken hydrogen bond with two protons facing each other) are created [62, 63]. Consequently, net polar ordering of the H₂O molecules is established near the

interface, which enhances the SFG signal. A similar mechanism was used to explain the strong bonded OH signal in SFG from a layer of ice grown on the Pt(111) surface [44].

2.6 Discussion

2.6.1 Laser heating

One of our major concerns in this experiment was to ensure that the results shown in Fig. 2.16 are intrinsic and not a consequence of laser heating. Fortunately, ice does not absorb the infrared in the free OH range as strongly as it does in the bonded OH range. The infrared penetration depth in ice is $\sim 40\mu$m at 3700 cm^{-1}, in comparison to less than 1 μm at the peak absorption frequency 3250 cm^{-1}. We tested the heating effect experimentally. Fig. 2.25 shows a set of SFG spectra of the vapor/ice interface with different infrared input energy. Attenuation of the infrared pulse was achieved by inserting silicon windows (2 mm thick, polished on both sides) in the infrared beam path and readjusting the time delay. In the free OH range the effect of laser heating was found to be negligible. However, laser heating can be a serious problem in the bonded OH range since the energy of each infrared input pulse ($\sim$100 μJ concentrated in an area of $\sim$1 mm^2) is enough to melt the surface layer of ice. As shown in Fig. 2.25, laser heating reduced the SFG signal of the bonded OH stretch. As we further attenuated the infrared to below 20% of its full power, laser heating became negligible as indicated by the linear dependence of the SFG intensity on the input infrared power. Therefore, we chose to use 20% of the full infrared power to obtain the SFG spectra of ice in the bonded OH range (2900 cm^{-1} to 3570 cm^{-1}).

Laser heating sets a practical limit on our study of the bonded OH peak near
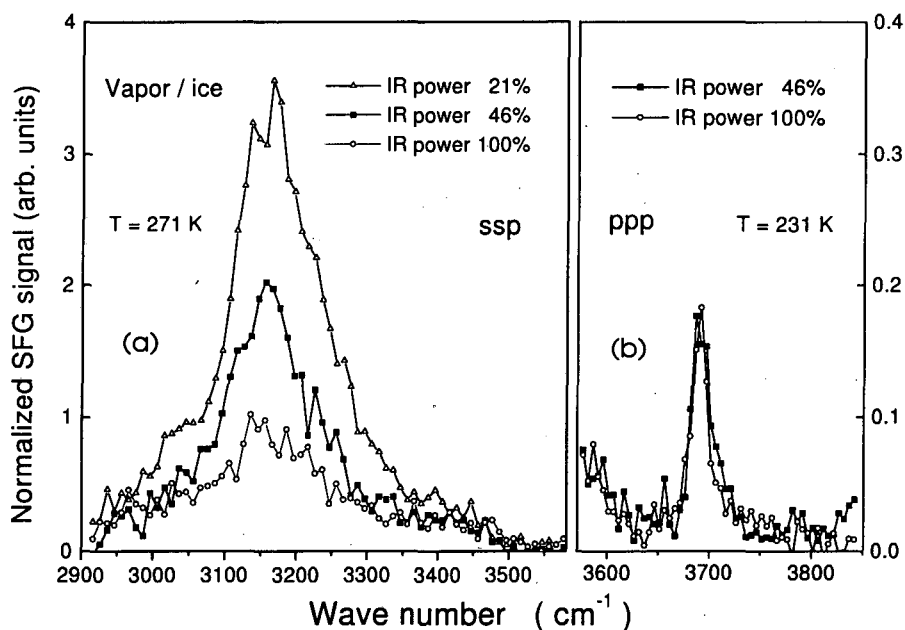
Figure 2.25: Test of laser heating effect with different infrared input pulse energies. The SFG intensity has been normalized against the infrared power. (a)In the bonded OH range, the decrease of the SFG intensity with the increase of the infrared power is due to laser heating. (b)In the free OH range, laser heating is negligible.

273 K. The very low intensity of the bonded OH peak at 272.5 K in Fig. 2.18 could be an artifact due to laser heating. The silica/ice spectra in some early publications [42, 43] could have suffered from laser heating as well.

2.6.2 Surface roughening

The roughening transition is another phenomenon that occurs on solid surfaces [64] and often results in the disappearance of facets and rounding up of the equilibrium crystal shape. Surface roughening is similar to surface melting in the sense that it also causes disorder at a solid surface. Unlike other techniques which measure how the quasi-liquid layer on ice grows in thickness and extends into the bulk, SFG only measures the disorder in the top surface layer. To determine whether the surface disorder observed by SFG is due

to surface melting or surface roughening, we refer to other experiments. Elbaum studied the surface roughening of ice with interference microscopy [65] and found that the roughening transition does not happen on the (0001) basal surface of ice at all temperatures up to the triple point, in contrast to the (10$\bar{1}$0) prism surface, on which a roughening transition was observed around -2°C. In our experiment, we used the (0001) surface and observed the surface disorder at much lower temperatures than the temperature range in Ref. [65]. Surface roughening as the explanation can thus be ruled out.

We should mention that we had another kind of roughening of the ice surface during our experiment, which is on a much larger length scale. We found that the smoothness of the vapor/ice interface appeared to deteriorate during the experiment, especially when the temperature was above 253 K, presumably due to extended exposure to the high intensity laser pulses. Although the effect of laser heating on the SFG spectra was confirmed to be negligible, mild laser heating was still present and could disturb the delicate dynamic equilibrium at the vapor/ice interface, resulting in a slow deterioration of the surface smoothness on a macroscopic scale. However, we found that this kind of roughening reduces the free OH peak intensities in *ssp* and *ppp* proportionally and thus doesn't affect the ratio $A_{q,\text{eff}}(ppp)/A_{q,\text{eff}}(ssp)$, a measure of the surface order. This indicates that the SFG signal was still dominated by large flat (0001) terraces at the vapor/ice interface. We also found that the reduction of the SFG signal due to such roughening was approximately proportional to the reduction of the intensity of the specular reflection of the 532 nm visible input pulse. A photodiode was used in our experiment to monitor the smoothness of the vapor/ice interface by measuring the reflected visible pulse. We corrected the SFG sig-

nal according to the measured visible reflection intensity when necessary, and terminated the experiment if the reflected visible pulse intensity dropped to below 2/3 of that from a perfectly smooth ice surface.

2.6.3 Effect of impurities

It has been suggested that impurities may affect the surface melting of ice [22, 30]. In our study of the vapor/ice interface, however, the impurity effect due to contamination of the ice sample is unlikely to be significant. We note that in a recent experiment to demonstrate the effect of impurities, an ice sample containing a very high concentration (10 mM) of KCl was used [36]. Our ice crystals were grown and prepared under clean conditions, and therefore, concerns about ionic impurities with a high concentration seem to be irrelevant. It would be interesting to study the impurity effect by doping the ice crystals as we did for the silica/ice interface with ammonia-doped ice (Sec. 2.5.2), in which NH_3 with a concentration of $\sim$1 mM was successfully doped into the ice crystal. It was demonstrated that a much higher doping concentration (600 ppm or 30 mM) of KOH in ice can be achieved (beyond which the ice crystal turns slightly milky) [66].

Some airborne impurities are more likely to be a source of contamination than ionic impurities since air was present in our experiment. One typical contaminant in atmosphere is the hydrocarbon. In our experience, this kind of impurity at the vapor/water or vapor/ice interface is likely to suppress the dangling OH bonds. In the current experiment, hydrocarbon contamination is unlikely because of the clear presence of the free OH bonds. Another air borne impurity is carbon dioxide (CO_2). We have tried to study the effect by intentionally dosing the ice chamber with CO_2 gas. Unfortunately, CO_2 has an infrared ab-

sorption band right at the free OH stretch frequency and prevented us from getting reliable SFG spectra from the CO_2/ice interface. This problem could be solved by reducing the infrared beam path in the ice chamber. Investigating the impurity effect on surface melting of ice is an ongoing project.

2.7 Conclusion

In summary, we have used SFG vibrational spectroscopy to study surface melting of ice by probing the structure of the very first monolayer of the (0001) surface of ice I_h. Orientational disordering of the surface molecules as a signature of surface melting appears to set in around 200 K. The degree of disorder increases with temperature and shows that the quasi-liquid layer on the ice surface is structurally different from the normal water surface layer. Our results suggest that the usual model treating the quasi-liquid layer as a structurally uniform film should be modified.

Chapter 3

Surface alignment of polymers

3.1 Introduction

The alignment of liquid crystal (LC) molecules on rubbed polymer surfaces was discovered in 1911 [67]. In recent years, this phenomenon has been studied extensively not only because of the basic interest in understanding the underlying mechanism but also because of its relevance to LC display technology. Today, rubbed polymer films are widely used in industry to obtain homogeneous bulk LC alignment for LC displays [68]. Different mechanisms have been proposed for LC alignment on rubbed polymer surfaces. One assumes that rubbing creates microgrooves or scratches on polymer surfaces which then align the LC along the grooves to minimize the energy of elastic distortion [69]. Another suggests that rubbing aligns surface polymer chains which in turn align the LC through intermolecular interaction [70]. The latter is believed to be operative when LC molecules anchor strongly to polymer surfaces, as is commonly the case in the LC industry.

To study LC alignment by rubbed polymer surfaces, a number of experimental

techniques have been used. Optical second-harmonic generation (SHG) showed that a rubbed polymer surface can align an adsorbed LC monolayer which then aligns the LC bulk by molecular correlation [71, 72, 73, 74], providing convincing evidence that molecular interaction between LC and polymer at the surface is responsible for the LC alignment. Attempts to study the rubbed polymer itself with SHG have also been made, but the structural information obtained so far from SHG is rather limited [75]. Atomic force microscopy (AFM) could provide images of rubbed polymer surfaces showing an overall anisotropy but was unable to resolve the surface polymer chains [76, 77, 78]. Ellipsometry [79] and infrared spectroscopy [80, 81, 82, 83] could measure rubbing-induced anisotropy and other structural changes in the polymer film. However, because of their lack of surface specificity, it is unclear whether these results indeed represent the real surface structure of the rubbed polymer. Grazing incidence X-ray scattering (GIXS) could probe a surface region of $\sim$5 nm thick [84, 85]. A higher surface sensitivity has been achieved by Near-edge X-ray absorption fine structure (NEXAFS) spectroscopy, which could probe a surface layer of $\sim$1 nm thick [86, 87, 88, 89].

In this chapter, we describe the use of sum-frequency vibrational spectroscopy to probe the structure of a rubbed polymer surface. SFG is ideally suited as a probe to study interfacial structure between two centrosymmetric media. Being a nonlinear optical process involving three optical waves, in principle, SFG can yield more detailed structural information than all the linear optical techniques including NEXAFS. We have applied SFG vibrational spectroscopy to rubbed polyvinyl alcohol (PVA, [-CH$_2$-CHOH-]$_n$) [8, 9] and rubbed polyimide [90]. In this chapter we shall concentrate on PVA only. Rubbed
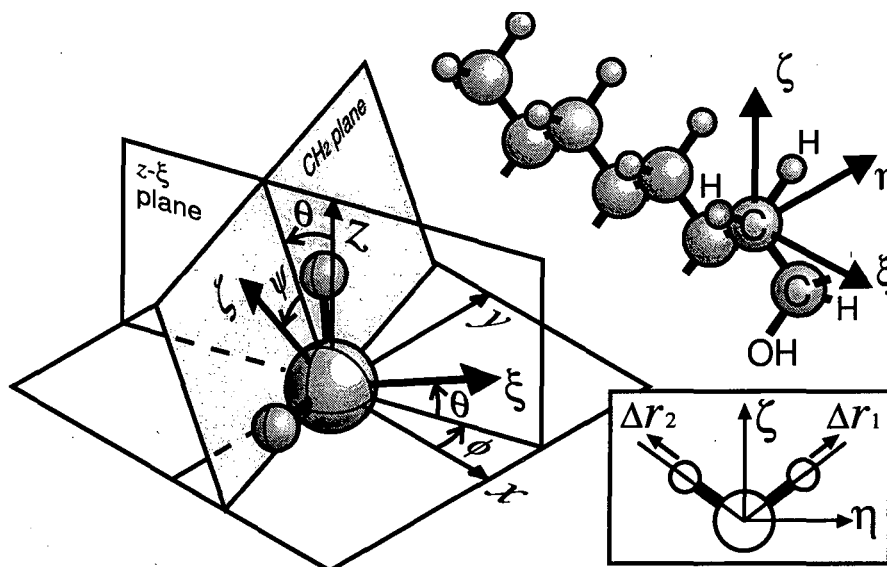
Figure 3.1: Molecular structure of PVA and orientational geometry of a CH_2 group on a rubbed PVA surface. Axis x is along the rubbing direction, and z is along the surface normal of the polymer film. Axis ξ is normal to the CH_2 plane and along the PVA chain, ζ along the symmetry axis of CH_2 and η orthogonal to ξ and ζ.

PVA is known to align LC molecules in a way similar to rubbed polyimide [72] but has a much simpler monomer unit. We focused on the stretch vibrational modes of the CH_2 groups of PVA at the surface. The CH_2 groups directly associated with the PVA backbone are oriented perpendicularly to the local PVA chains, as shown in Fig. 3.1. From the measured SFG spectra, we can deduce an orientational distribution for the CH_2 groups at the surface. This then yields directly an orientational distribution for the PVA chains on the rubbed surface. We found that the PVA chain orientation is indeed strongly affected by rubbing.

In the following sections, we present a detailed analysis of the SFG results together with the SHG study of an 8CB (4-n-octyl-4'-cyanobiphenyl) LC monolayer deposited on rubbed PVA (Fig. 3.2) showing how a rubbed PVA surface aligns the LC monolayer.
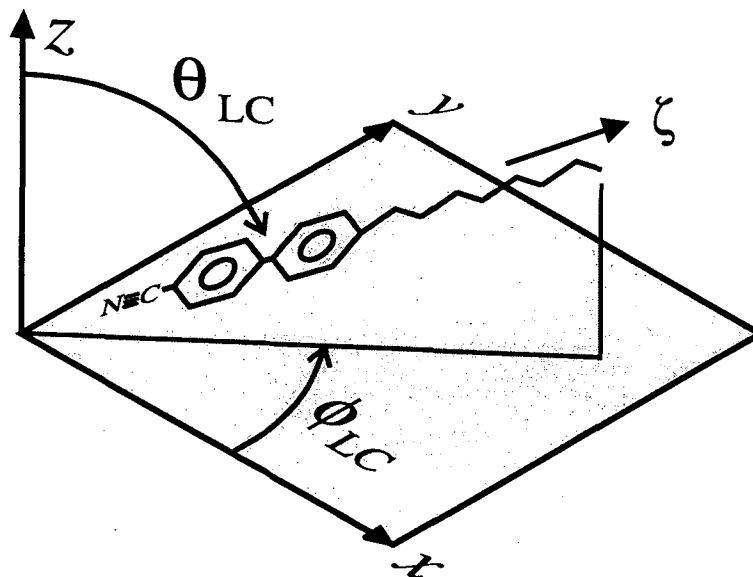
Figure 3.2: Molecular structure and orientational coordinates of an 8CB molecule deposited on a rubbed PVA surface. ζ is along the long axis of the cyanobiphenyl core of the 8CB molecule. θ_{LC} and ϕ_{LC} are the polar and azimuthal angles of ζ. The x axis stands for the rubbing direction.

Section 3.2 provides the theoretical background for the work and Sec. 3.3 describes the experimental arrangement. Experimental results and data analysis are presented in Sec. 3.4, and discussions of the results are in Sec. 3.5.

3.2 Theory

3.2.1 Surface sum-frequency and second-harmonic generation

As shown in Chap. 1, surface SFG results from a second-order nonlinear polarization induced at an interface by two input fields $\mathbf{E}(\omega_1)$ and $\mathbf{E}(\omega_2)$ at frequencies ω_1 (visible) and ω_2 (infrared), respectively,

$$\mathbf{P}^{(2)}(\omega_s) = \epsilon_0 \chi^{(2)} : \mathbf{E}(\omega_1)\mathbf{E}(\omega_2) , \tag{3.1}$$

where $\chi^{(2)}$ denotes the surface nonlinear susceptibility tensor. In MKS units the SFG output intensity in the reflected direction is given by

$$I(\omega_s) = \frac{\omega_s^2}{8\epsilon_0 c^3 \cos^2 \beta_s} |\chi^{(2)}_{\text{eff}}|^2 I(\omega_1) I(\omega_2) \ . \tag{3.2}$$

Here, β_s is the exit angle of the SF output, $I(\omega_i)$ is the beam intensity at ω_i, and $\chi^{(2)}_{\text{eff}}$ is the effective surface nonlinear susceptibility defined as

$$\chi^{(2)}_{\text{eff}} = [\mathbf{L}(\omega_s) \cdot \hat{\mathbf{e}}_s] \cdot \chi^{(2)} : [\mathbf{L}(\omega_1) \cdot \hat{\mathbf{e}}_1][\mathbf{L}(\omega_2) \cdot \hat{\mathbf{e}}_2] \ , \tag{3.3}$$

with $\hat{\mathbf{e}}_i$ being the unit polarization vector of the optical field at ω_i and $\mathbf{L}(\omega_i)$ the tensorial Fresnel factor (see Appendix B for details).

Eqs. (3.1)-(3.3) also apply to second-harmonic generation (SHG) with $\omega_1 = \omega_2$. In SHG, often only one input laser beam at frequency ω (usually in the visible) is used and the SH signal at $\omega_s = 2\omega$ is collected.

3.2.2 SFG vibrational spectroscopy for surface molecular groups

The surface nonlinear susceptibility tensor $\chi^{(2)}(\omega_s = \omega_1 + \omega_2)$ for SFG is expected to be resonantly enhanced when ω_2 approaches a surface vibrational resonance. Scanning over such resonances yields a surface SFG vibrational spectrum. We can express $\chi^{(2)}$ in terms of the resonant hyperpolarizability $\alpha_R^{(2)}$ for the surface molecular groups.

$$\begin{aligned} \chi^{(2)} &= \chi^{(2)}_{\text{NR}} + N_S \langle \alpha_R^{(2)} \rangle_f \\ &= \chi^{(2)}_{\text{NR}} + N_S \int \alpha_R^{(2)}(\Omega) f(\Omega) d\Omega \ , \end{aligned} \tag{3.4}$$

where $\chi^{(2)}_{\text{NR}}$ describes the nonresonant contribution, N_S is the surface density of molecules, Ω denotes a set of orientational angles (θ, ϕ, ψ) defined in Fig. 3.1 , and $\langle\ \rangle_f$ represents an

orientational average over the orientational distribution function $f(\Omega)$.

We assume that $\alpha_R^{(2)}$ is composed of Lorentzian resonant terms,

$$\alpha_R^{(2)}(\omega_2) = \sum_q \frac{a_q}{\omega_2 - \omega_q + i\Gamma_q} ,$$ (3.5)

where a_q, ω_q and Γ_q are the amplitude, resonant frequency and damping constant of the qth molecular vibrational mode. Insertion of Eq. (3.5) into Eq. (3.4) gives

$$\chi^{(2)}(\omega_2) = \chi_{NR}^{(2)} + \sum_q \frac{A_q}{\omega_2 - \omega_q + i\Gamma_q} ,$$ (3.6)

$$A_q = N_S \int a_q(\Omega) f(\Omega) d\Omega .$$ (3.7)

Being a rank-3 tensor, $\chi^{(2)}$ has in general 27 elements. Surface symmetry, however, can make some elements vanish and some become mutually dependent. In many cases, we can determine all the independent nonvanishing $\chi^{(2)}$ elements by measuring $\chi_{eff}^{(2)}$ with various beam geometries and polarization combinations. From the observed dispersion of $\chi^{(2)}$ we can deduce A_q in Eq. (3.6). We can also obtain a_q in Eq. (3.5) for the molecular nonlinear polarizability $\alpha_R^{(2)}$ from other measurements or theoretical calculations. Then, Eq. (3.7) will allow us to obtain an approximate orientational distribution function $f(\Omega)$. Note that in Eqs. (3.4) and (3.7), the microscopic local-field correction is not fully included. However, this has no effect on our deduction of $f(\Omega)$ (see Appendix C for details).

Since we shall be interested in the stretch vibrations of the CH_2 groups of PVA, we present here a simple theoretical model to calculate the resonant mode amplitude a_q for CH_2. There are two stretch vibrational modes for a CH_2 group, namely, the symmetric stretch (s) and the antisymmetric stretch (a). The theory of sum-frequency vibrational spectroscopy shows that a_q is related to the infrared and Raman characteristics of a vibrational mode

through the equation [45]

$$(a_q)_{lmn} = -\frac{1}{2\epsilon_0\omega_q}\frac{\partial\mu_n}{\partial Q_q}\frac{\partial\alpha_{lm}^{(1)}}{\partial Q_q} , \qquad (3.8)$$

where $\frac{\partial\mu_n}{\partial Q_q}$ and $\frac{\partial\alpha_{lm}^{(1)}}{\partial Q_q}$ are the infrared dipole derivative and the Raman polarizability tensor of the qth vibrational mode, and Q_q is the classical normal coordinate. From Eq. (3.8) we can see some important properties of the tensor $\mathbf{a}_q$. First, the Raman polarizability tensor is symmetric for CH_2, and therefore, $(a_q)_{lmn}$ is also symmetric in l and m, i.e., $(a_q)_{lmn} = (a_q)_{mln}$. Second, since all the $\frac{\partial\mu_n}{\partial Q_q}$ and $\frac{\partial\alpha_{lm}^{(1)}}{\partial Q_q}$ elements are real, $(a_q)_{lmn}$ must also be real, although $\chi^{(2)}$ can be complex due to the damping constant Γ_q in Eq. (3.6).

We can use Eq. (3.8) to calculate $(a_q)_{lmn}$ for the two stretch modes of CH_2. If we assume that the carbon atom is fixed in position, the normal coordinates of the s- and a-stretch modes are:

$$Q_s = \sqrt{\frac{m_H}{2}}(\Delta r_1 + \Delta r_2) ,$$

$$Q_a = \sqrt{\frac{m_H}{2}}(\Delta r_1 - \Delta r_2) , \qquad (3.9)$$

where Δr_1 and Δr_2 are the stretch distances of the two C-H bonds (Fig. 3.1), and m_H is the mass of a hydrogen atom. The dipole derivative $\frac{\partial\mu_n}{\partial Q_q}$ and the Raman polarizability $\frac{\partial\alpha_{lm}^{(1)}}{\partial Q_q}$ of these two modes can be calculated by assuming that the total dipole moment (or polarizability) is the sum of the dipole moments (or polarizabilities) of the two individual C-H bonds and that the dipole moment (or polarizability) of each individual C-H bond depends only on its own coordinate. This bond additivity model has been used by other authors in similar calculations [91]. Using this model, we find

$$\frac{\partial\mu}{\partial Q_s} = \frac{1}{\sqrt{2m_H}}\left(\frac{\partial\mu_1}{\partial\Delta r_1} + \frac{\partial\mu_2}{\partial\Delta r_2}\right) ,$$

$$
\begin{aligned}
\frac{\partial \boldsymbol{\mu}}{\partial Q_{\mathrm{a}}} &= \frac{1}{\sqrt{2m_{\mathrm{H}}}} \left(\frac{\partial \boldsymbol{\mu}_1}{\partial \Delta r_1} - \frac{\partial \boldsymbol{\mu}_2}{\partial \Delta r_2} \right) , \\
\frac{\partial \boldsymbol{\alpha}^{(1)}}{\partial Q_{\mathrm{s}}} &= \frac{1}{\sqrt{2m_{\mathrm{H}}}} \left(\frac{\partial \boldsymbol{\alpha}_1^{(1)}}{\partial \Delta r_1} + \frac{\partial \boldsymbol{\alpha}_2^{(1)}}{\partial \Delta r_2} \right) , \\
\frac{\partial \boldsymbol{\alpha}^{(1)}}{\partial Q_{\mathrm{a}}} &= \frac{1}{\sqrt{2m_{\mathrm{H}}}} \left(\frac{\partial \boldsymbol{\alpha}_1^{(1)}}{\partial \Delta r_1} - \frac{\partial \boldsymbol{\alpha}_2^{(1)}}{\partial \Delta r_2} \right) .
\end{aligned}
\tag{3.10}
$$

By symmetry, for the s-stretch there are three independent nonvanishing $(a_{\mathrm{s}})_{lmn}$ elements $(a_{\mathrm{s}})_{\xi\xi\zeta}$, $(a_{\mathrm{s}})_{\eta\eta\zeta}$, $(a_{\mathrm{s}})_{\zeta\zeta\zeta}$, and for the a-stretch there is only one $(a_{\mathrm{a}})_{\eta\zeta\eta} = (a_{\mathrm{a}})_{\zeta\eta\eta}$. Here (ξ, η, ζ) are the molecular coordinates defined in Fig. 3.1. To carry out numerical calculations, we need the values of the dipole and polarizability derivatives of a single C-H bond. Here we use the single bond dipole derivative deduced from Ref. [92] (the negative sign is based on the argument in Ref. [93])

$$
\frac{\partial \mu}{\partial \Delta r} \approx -0.86 \text{ Debye/Å} \approx -2.9 \times 10^{-20} \mathrm{C} ,
\tag{3.11}
$$

and the single bond polarizability derivative from Ref. [94],

$$
\frac{\partial \alpha_{\parallel}^{(1)}}{\partial \Delta r} \approx 3.0 \times 10^{-30} \frac{\mathrm{mC}}{\mathrm{V}} ,
\tag{3.12}
$$

$$
\frac{\partial \alpha_{\perp}^{(1)}}{\partial \Delta r} \approx 0.14 \times \frac{\partial \alpha_{\parallel}^{(1)}}{\partial \Delta r} \approx 0.4 \times 10^{-30} \frac{\mathrm{mC}}{\mathrm{V}} .
\tag{3.13}
$$

After inserting these numbers into Eq. (3.8), we obtain all the nonvanishing a_q elements for the CH_2 stretch modes:

$$
\begin{aligned}
(a_{\mathrm{s}})_{\xi\xi\zeta} &\approx 0.16 \, a_0 , \\
(a_{\mathrm{s}})_{\eta\eta\zeta} &\approx 0.82 \, a_0 , \\
(a_{\mathrm{s}})_{\zeta\zeta\zeta} &\approx 0.49 \, a_0 , \\
(a_{\mathrm{a}})_{\eta\zeta\eta} &= (a_{\mathrm{a}})_{\zeta\eta\eta} \approx 0.66 \, a_0 ,
\end{aligned}
\tag{3.14}
$$

where a_0 is a constant defined for a single C-H bond

$$a_0 = -\frac{1}{2\epsilon_0\omega_q m_{\mathrm{H}}}\frac{\partial\mu}{\partial\Delta r}\frac{\partial\alpha_{\parallel}^{(1)}}{\partial\Delta r} \approx 5.3 \times 10^{-27}\ \mathrm{m^4V^{-1}sec^{-1}}\ . \tag{3.15}$$

3.2.3 SHG from a liquid crystal monolayer

SHG has been used successfully to measure the molecular orientational distributions of liquid crystal monolayers. A detailed description of the theory and technique can be found in Ref. [72]. Similar to SFG, the surface SHG nonlinear susceptibility is also an orientational average of the nonlinear polarizability of surface molecular groups.

For 8CB, the SHG nonlinear polarizability mainly originates from the highly delocalized electrons in the cyanobiphenyl group and has one dominant tensor element $\alpha_{\zeta\zeta\zeta}^{(2)}$ along the long molecular axis ζ (Fig. 3.2). As a good approximation[72], we can neglect other tensor elements of $\boldsymbol{\alpha}^{(2)}$ and express $\chi_{ijk}^{(2)}$ as

$$\begin{aligned}
\chi_{ijk}^{(2)} &= N_{\mathrm{S}}\langle(\hat{i}\cdot\hat{\zeta})(\hat{j}\cdot\hat{\zeta})(\hat{k}\cdot\hat{\zeta})\rangle_g\alpha_{\zeta\zeta\zeta}^{(2)} \\
&= N_{\mathrm{S}}\int(\hat{i}\cdot\hat{\zeta})(\hat{j}\cdot\hat{\zeta})(\hat{k}\cdot\hat{\zeta})\alpha_{\zeta\zeta\zeta}^{(2)}g(\Omega)d\Omega\ , \tag{3.16}
\end{aligned}$$

where N_{S} is the surface number density of 8CB molecules; $\hat{i}$, $\hat{j}$, and $\hat{k}$ are the lab coordinates defined on the substrate; and $\langle\ \rangle_g$ denotes an average over the orientational distribution function $g(\Omega)$. By measuring all the nonvanishing independent $\chi_{ijk}^{(2)}$ elements we can deduce an approximate $g(\Omega)$.

3.3 Experiment

Polyvinyl alcohol (Scientific Polymer Products, Inc., M.W.=14,000, 100% hydrolyzed) was dissolved in water (1.5% weight) and spin coated on fused silica plates (hy-

drophilic), followed by baking and rubbing with velvet cloth. The film thickness was about 30 nm, and the rubbing strength used was at a saturation level, i.e., stronger rubbing would not improve the chain alignment further [72]. For the measurement, the sample was mounted on a 360° rotational stage, and the SFG spectra were taken with various input/output polarization combinations and different sample orientations specified by the azimuthal angle γ between the incidence plane and the rubbing direction (Fig. 1.3).

In the SHG study of LC alignment on PVA, 8CB was deposited on a rubbed PVA surface by evaporation, and a visible laser beam at 532 nm was directed onto the sample with an incidence angle of 67° (see Ref. [72] for details). The SHG output was detected in the reflected direction. Four different input/output polarization combinations (s_{in}-s_{out}, s_{in}-p_{out}, p_{in}-s_{out}, and p_{in}-p_{out}) were used. The azimuthal variation of SHG was also measured.

3.4 Results and analysis

3.4.1 SFG spectra and mode amplitudes

Surface SFG spectra in the CH stretch region of a rubbed PVA sample were taken with 6 different polarization combinations, each with different azimuthal orientations (typically every 45°). The spectra were found to be reproducible for different PVA samples prepared under the same conditions. Shown in Fig. 3.3 are the SFG spectra with the azimuthal angle $\gamma = 0°$ (parallel to rubbing) and $\gamma = 90°$ (perpendicular to rubbing) for the *ssp* (*s*-, *s*- and *p*-polarized SF output, visible input and infrared input, respectively), *sps* and *ppp* polarization combinations, and $\gamma = 90°$ for *sss*, *spp* and *pps*. For comparison, the spectra of *ssp* and *sps* from an unrubbed PVA surface are shown in Fig. 3.4.
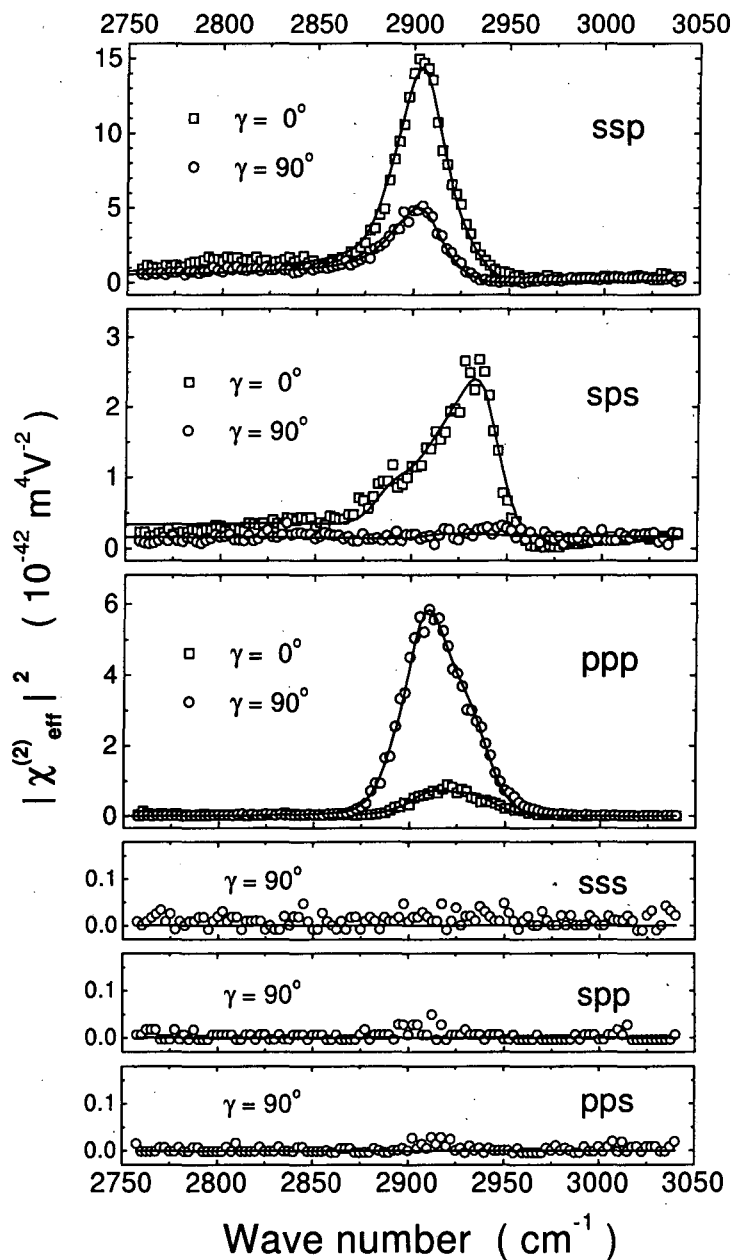
Figure 3.3: SFG spectra of a rubbed PVA surface in the CH stretch range for different polarization combinations. Only spectra at $\gamma = 0°$ and $90°$ are shown for *ssp*, *sps* and *ppp*. The spectra at $\gamma = 90°$ for *sss*, *spp* and *pps* are dominated by noise. Solid curves are fits from Eq. (3.6).
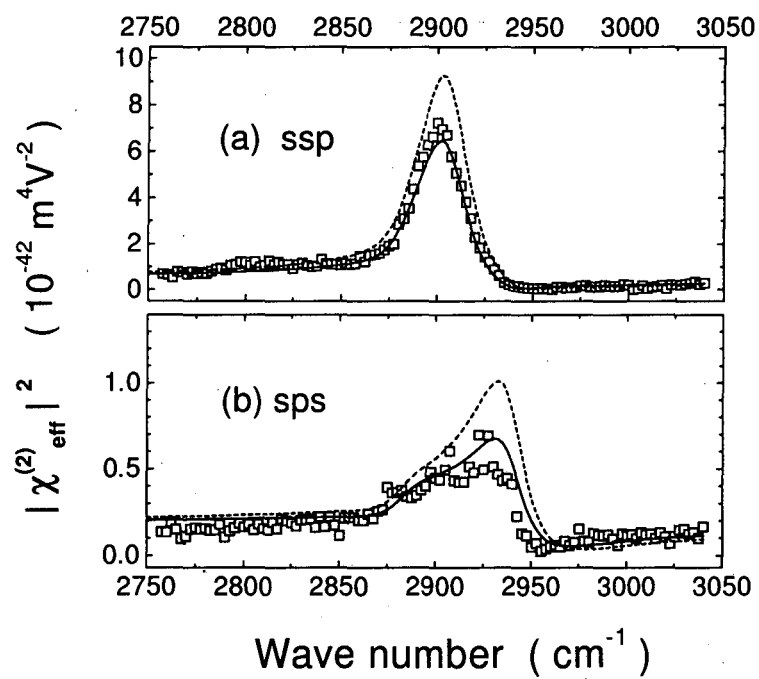
Figure 3.4: SFG spectra of unrubbed PVA for different polarization combinations (a)*ssp*, (b)*sps*. The solid and dashed lines are theoretical predictions assuming different orientational distributions (see Sec. 3.5.2).

All the measured SFG intensities have been calibrated with a reference z-cut quartz crystal, yielding for each polarization combination and sample orientation a spectrum of $|\chi_{\text{eff}}^{(2)}|^2$ in MKS units (see Sec. 1.3 for details). All the $|\chi_{\text{eff}}^{(2)}(\omega_2)|^2$ spectra can then be fit by

$$\chi_{\text{eff}}^{(2)}(\omega_2) = \chi_{\text{NR,eff}}^{(2)} + \sum_q \frac{A_{q,\text{eff}}}{\omega_2 - \omega_q + i\Gamma_q} , \tag{3.17}$$

assuming the presence of three resonant modes at $\omega_q/(2\pi c)=$ 2882, 2907 and 2940 cm^{-1}, each with a damping constant $\Gamma/(2\pi c)=16$ cm^{-1}. The first one, which is rather weak, probably comes from the stretch mode of the CH group on the PVA chain; the last two, highly prominent except for some polarization combinations and sample orientations, can be identified with the symmetric (s) and antisymmetric (a) stretch modes of CH$_2$ [95]. The azimuthal polar plots of the mode amplitudes $A_{\text{s,eff}}$ and $A_{\text{a,eff}}$ deduced by fitting of the spectra are presented in Fig. 3.5. Some additional data points of $A_{\text{s,eff}}(ssp)$ and $A_{\text{a,eff}}(sps)$ in Fig. 3.5 were deduced from the measured SFG peak intensity for every 5° with the infrared input frequency fixed on the resonant peak. $A_{\text{s,eff}}(sps)$ is below the noise level and not shown.

Note that the measurements described above could not determine the relative signs of $A_{q,\text{eff}}$ for different polarization combinations. These relative signs, however, can be determined by measuring interference between different $A_{q,\text{eff}}$ components. For example, the SFG intensity with p-polarized infrared input, mixed (m-, partially s and partially p) polarized visible input and m-polarized SFG output is proportional to the absolute square of the linear combination of $A_{q,\text{eff}}(ssp)$ and $A_{q,\text{eff}}(ppp)$, which can interfere constructively or destructively depending on their relative sign (Fig. 3.6). From such interferences, we were able to determine the relative signs of all $A_{q,\text{eff}}$. As shown in Fig. 3.5, if we choose the sign
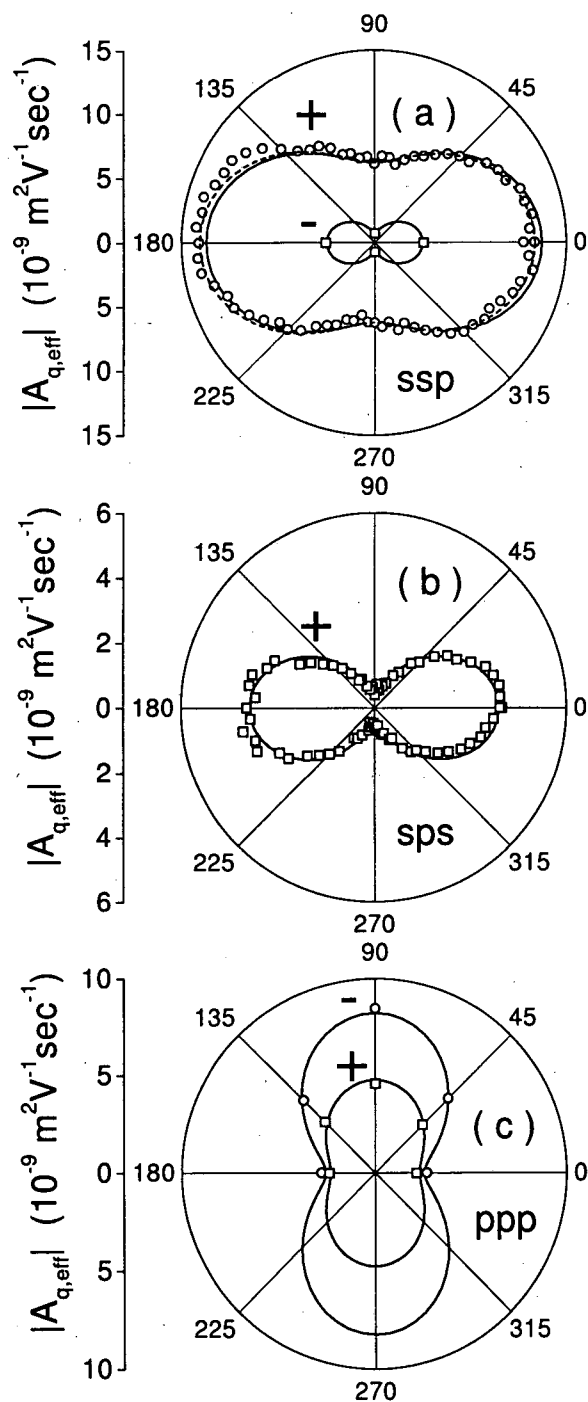
Figure 3.5: Effective mode amplitudes $|A_{q,\text{eff}}|$ of the CH_2 symmetric (circles) and antisymmetric (squares) stretch modes for rubbed PVA as functions of γ for different polarization combinations (a)*ssp*, (b)*sps* and (c)*ppp*. The relative signs of $A_{q,\text{eff}}$ are also shown in the figure. Symbols are values deduced from the measured SFG spectra. Lines are obtained from fits (see Sec. 3.4.4).
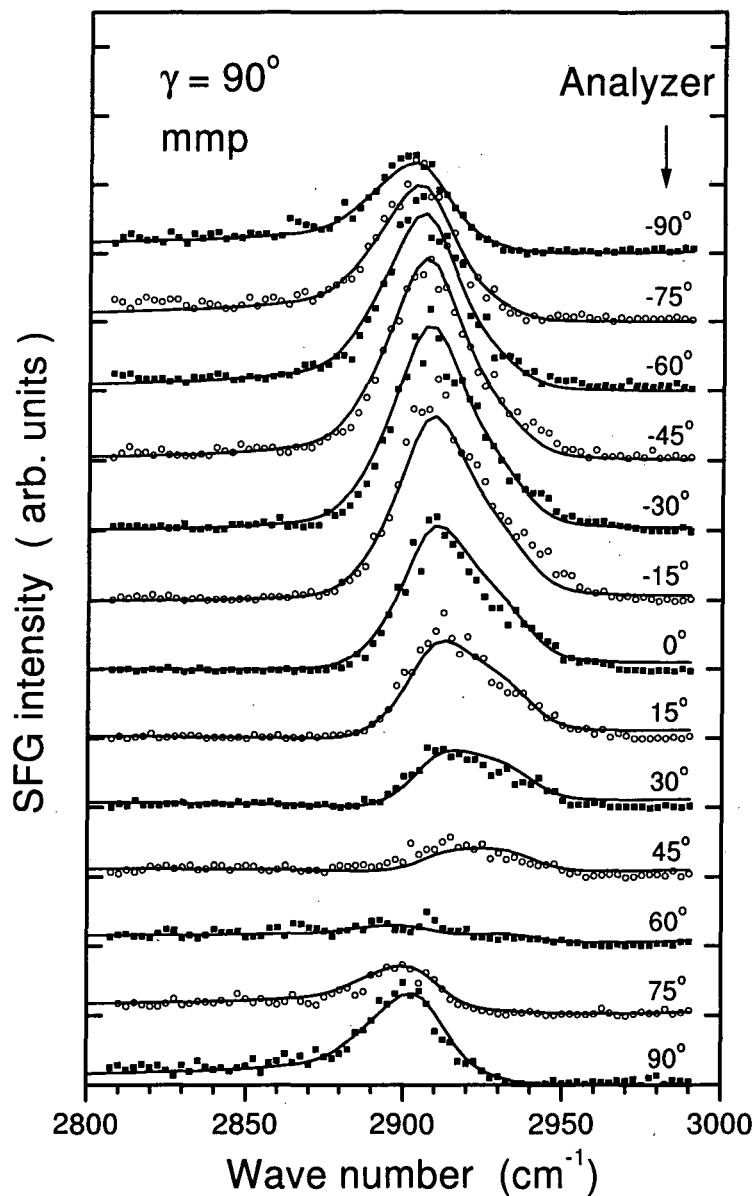
Figure 3.6: Relative phase measurement using the interference between $A_{q,\text{eff}}(ssp)$ and $A_{q,\text{eff}}(ppp)$. The infrared input was p polarized. The polarization of the 532 nm visible input was rotated clockwise (looking in the light propagation direction) from p by 40°. The polarization of the analyzer was rotated clockwise from p by an angle indicated on each spectrum.

of $A_{\mathrm{s,eff}}(ssp)$ to be positive, we find $A_{\mathrm{a,eff}}(sps)$ and $A_{\mathrm{a,eff}}(ppp)$ positive, and $A_{\mathrm{a,eff}}(ssp)$ and $A_{\mathrm{s,eff}}(ppp)$ negative.

Later, we will use these measured $A_{q,\mathrm{eff}}$ including their signs to deduce the tensor $\mathbf{A}_q$ through Eq. (3.3).

3.4.2 Surface specificity

In surface sum-frequency spectroscopy, there is always the question whether the SFG signal indeed comes from the surface under investigation. In order to deduce surface structure from SFG spectra, one has to make sure that the SFG signal is dominated by the surface contribution. In Chap. 4, we shall investigate the bulk contribution more generally. Here we present extra experimental studies specially for PVA.

For the rubbed PVA sample, the SFG signal might come from the bulk through electric-quadrupole and magnetic-dipole contributions or from the interface between PVA and the fused silica substrate. However, the fact that the SFG spectra of PVA are comparable in intensity to those observed from a closely packed monolayer of alkyl chains [96] indicates that the SFG signal of PVA originates from a monolayer of CH_2 pointing out of the polymer. The electric-quadrupole and magnetic-dipole contributions from CH_2 in the bulk are much weaker (Chap. 4), and significant contribution from the polymer/silica interface with CH_2 pointing towards the silica side is unlikely because the silica surface is hydrophilic [57]. Chemical studies indicate [97] that the monomer units in PVA prefer a head-to-tail arrangement, i.e., the OH groups are on alternate carbon atoms, and therefore all the CH_2 groups on a straight PVA chain should be on the same side of the chain as illustrated in Fig. 3.1. Being hydrophobic, the CH_2 groups like to point out of the polymer

surface. It is also known from infrared absorption studies [95] that strong hydrogen bonding exists between adjacent PVA chains. In order to maximize the number of hydrogen bonds to lower the surface free energy, the top layer of PVA chains would orient their OH bonds into the bulk and leave the CH_2 groups more or less polar ordered and pointing into air.

To check whether SFG from the PVA/air interface indeed dominated, we prepared a thick PVA sample ($\sim 500~\mu m$) on a fused silica substrate and measured the reflected SFG spectrum through the fused quartz substrate with the PVA layer facing down. From this geometry, the SFG signal from the PVA/air interface is negligible because (1) the PVA surface on the air side is rough, and (2) the infrared input is completely attenuated by the thick PVA layer. The result is shown in Fig. 3.7, in comparison with the SFG spectrum from a thin (~ 30 nm) spin-coated PVA film (unrubbed) which was also measured through the fused silica substrate. It clearly shows that the SFG contribution from the PVA/fused silica interface is much weaker than that from the PVA/air interface.

We also measured the SFG spectrum of the thin PVA film through the fused silica substrate as we put the sample in contact with water and found that the strong SFG signal dissappeared. After drying the film, the spectrum reappeared, indicating that the PVA film had not been dissolved in water. This is in agreement with our understanding of the strong SFG signal from the PVA/air interface. With the sample in contact with water, strong hydrogen bonding between water and PVA would randomize the orientation of the surface CH_2 groups, causing a drastic decrease of the SFG intensity. Interestingly, this test experiment may also provide an example of environment-induced surface structural change of polymers, another important topic in polymer science and technology [98].
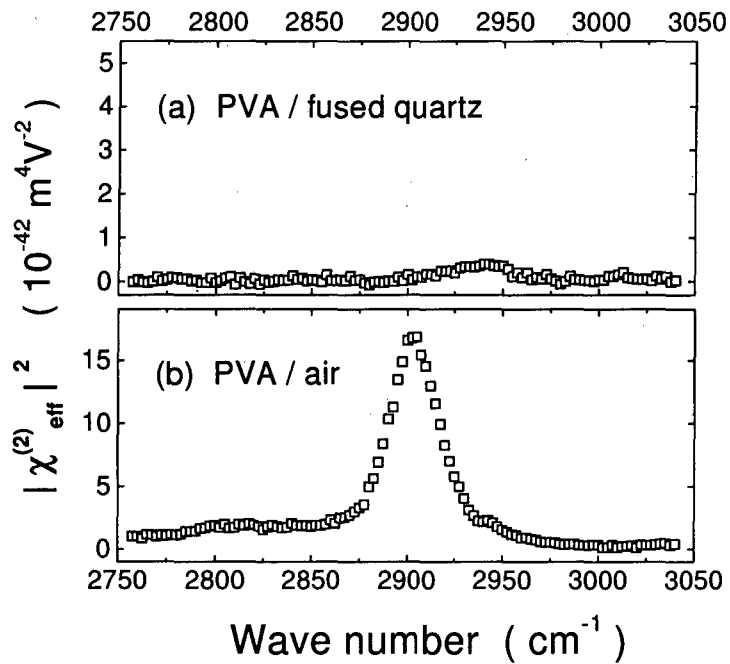
Figure 3.7: The SFG spectra of two PVA samples measured through the fused quartz substrates. The SFG signal from (a) the thick PVA sample on fused quartz is dominated by the PVA/fused silica interface, while the signal from (b) the thin spin-coated PVA film on fused silica is dominated by the PVA/air interface. The polarization combination used is *ssp*. Note that the intensity of the spectrum from PVA/air is higher than that in Fig. 3.4a because the Fresnel factors are different for the facing-down geometry.

3.4.3 Qualitative analysis of the SFG spectra

Without any calculation, we can already obtain some qualitative information about the CH_2 orientation on the rubbed PVA surface. This is illustrated in Fig. 3.8.

First, the excitation of the CH_2 symmetric stretch requires an IR polarization component along the CH_2 symmetry axis ζ defined in Fig. 3.1. The fact that the mode is very strong for the ssp polarization combination (with the last index p being the infrared polarization) but very weak for sps for all γ indicates that the CH_2 axis ζ must be nearly along the z axis. Second, the excitation of the CH_2 antisymmetric stretch requires an IR component along the axis η in the CH_2 plane. Since this mode is very strong for sps at $\gamma = 0°$ (Fig. 3.8a) but very weak at $\gamma = 90°$ (Fig. 3.8b), the CH_2 plane must be nearly the y-z plane. Correspondingly, the PVA chains must be oriented nearly parallel to the surface along the x axis, the rubbing direction. Finally, as seen from the plot of $A_{s,\text{eff}}(ssp)$ in Fig. 3.5, there is a small forward/backward asymmetry for $\gamma = 0°$ and $\gamma = 180°$. As will be shown later, this indicates that the average chain orientation has a slight upward tilt along the rubbing direction.

3.4.4 Quantitative analysis of the SFG data

As mentioned earlier, the surface nonlinear susceptibility $\chi_{ijk}^{(2)}$ (correspondingly, $(A_q)_{ijk}$ for each vibrational mode) has 27 matrix elements, but symmetry may greatly reduce the number of independent nonvanishing elements.

First, because the rubbed PVA surface has C_{1v} symmetry with the x-z plane being a mirror plane, all the $\chi_{ijk}^{(2)}$ elements with indices ijk containing an odd number of y should
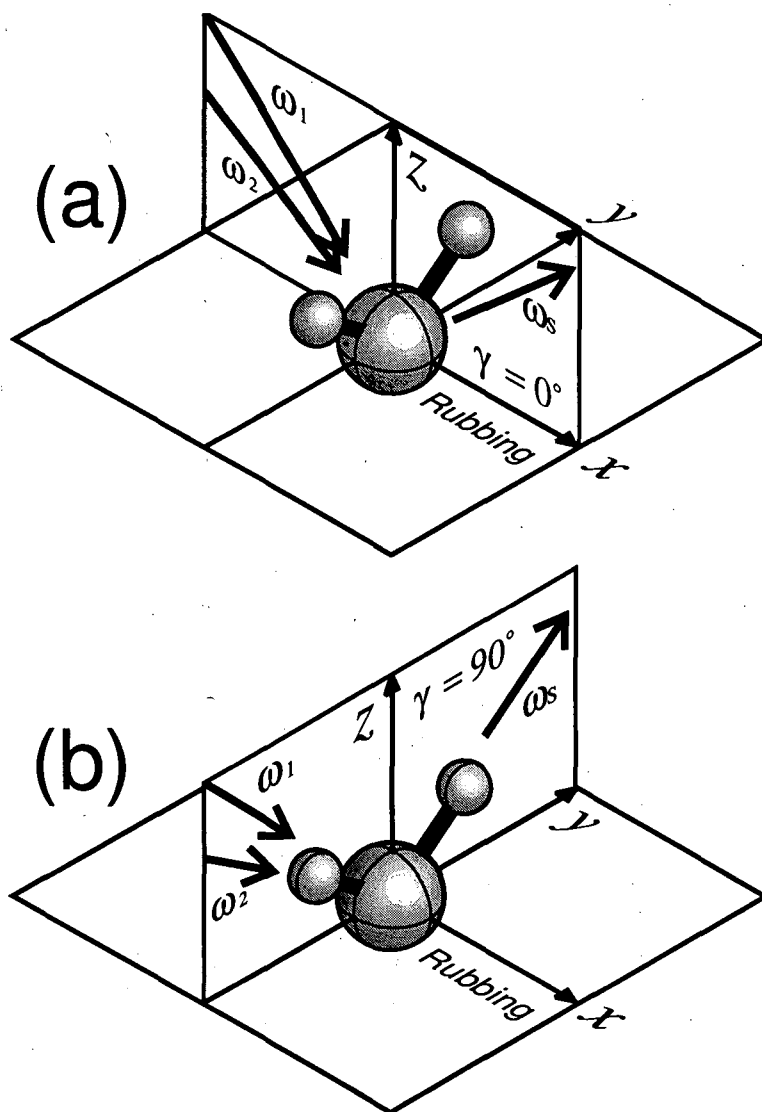
Figure 3.8: Sketches showing that with the given CH_2 orientation, the beam geometry $\gamma = 0°$ in (a) allows observation of the CH_2 s-stretch mode by the *ssp* polarization combination, and the CH_2 a-stretch mode by *sps*, in the SFG spectra, and the beam geometry $\gamma = 90°$ in (b) allows observation of only the CH_2 s-stretch mode by the *ssp* polarization combination.

vanish. Second, as discussed in Sec. 3.2.2, we have the symmetry $\chi_{ijk}^{(2)} = \chi_{jik}^{(2)}$. Combining these two, we find that $(A_q)_{ijk}$ for each CH$_2$ mode has only 10 independent nonvanishing elements with the following indices

$$xxz \quad , \quad yyz \quad , \quad zzz \quad , \quad xzx = zxx \quad , \quad yzy = zyy \quad ,$$

$$xxx \quad , \quad yyx \quad , \quad zzx \quad , \quad xyy = yxy \quad , \quad xzz = zxz \quad .$$

Furthermore, we notice that the forward/backward asymmetry shown in Fig. 3.5 is very small and that the SFG spectra for the *sss*, *spp* and *pps* polarization combinations are too weak to distinguish from noise (Fig. 3.3). These suggest that we may first use C_{2v} as an approximation for the symmetry of the rubbed PVA surface and neglect the last five matrix elements listed above which contain an odd number of x. With this approximation, we can deduce the five major (C_{2v}-allowed) $(A_q)_{ijk}$ elements for both s- and a-stretches of CH$_2$. Later, the observed forward/backward asymmetry will be used to deduce some of the remaining (C_{2v}-forbidden) elements if possible.

From the theory described in Sec. 3.2 we find that $A_{q,\text{eff}}$ in Eq. (3.17) is related to $(A_q)_{ijk}$ through

$$A_{q,\text{eff}} = [\mathbf{L}(\omega_s) \cdot \hat{\mathbf{e}}_s] \cdot \mathbf{A}_q : [\mathbf{L}(\omega_1) \cdot \hat{\mathbf{e}}_1][\mathbf{L}(\omega_2) \cdot \hat{\mathbf{e}}_2] \ . \tag{3.18}$$

Neglecting the forward/backward asymmetry, we can write $A_{q,\text{eff}}$ for the three polarization combinations in terms of the five major $(A_q)_{ijk}$ elements,

$$A_{q,\text{eff}}(\gamma, ssp) = \sin\beta_2 L_{YY}(\omega_s) L_{YY}(\omega_1) L_{ZZ}(\omega_2)$$

$$\times [(A_q)_{yyz} \cos^2\gamma + (A_q)_{xxz} \sin^2\gamma] \ , \tag{3.19}$$

$$A_{q,\text{eff}}(\gamma, sps) = \sin\beta_1 L_{YY}(\omega_s) L_{ZZ}(\omega_1) L_{YY}(\omega_2)$$

Table 3.1: Some parameters of the three beams and the calculated Fresnel factors for the air/fused quartz interface (applicable to the top surface only).

	ω_s	ω_1	ω_2
λ	460 nm	532 nm	3.4 μm
n	1.465	1.461	1.410
β	46.5°	45°	57°
L_{XX}	.93	.92	1.02
L_{YY}	.70	.71	.65
L_{ZZ}	1.07/ϵ'_s	1.08/ϵ'_1	.98/ϵ'_2
$e_X L_{XX}$ (p)	-.64	.65	.56
$e_Y L_{YY}$ (s)	.70	.71	.65
$e_Z L_{ZZ}$ (p)	.78/ϵ'_s	.77/ϵ'_1	.82/ϵ'_2

$$\times [(A_q)_{yzy} \cos^2 \gamma + (A_q)_{zzx} \sin^2 \gamma] , \qquad (3.20)$$

$$A_{q,\text{eff}}(\gamma, ppp) = -\cos \beta_s \cos \beta_1 \sin \beta_2 L_{XX}(\omega_s) L_{XX}(\omega_1) L_{ZZ}(\omega_2)$$

$$\times [(A_q)_{xxz} \cos^2 \gamma + (A_q)_{yyz} \sin^2 \gamma]$$

$$+ \sin \beta_s \sin \beta_1 \sin \beta_2 L_{ZZ}(\omega_s) L_{ZZ}(\omega_1) L_{ZZ}(\omega_2)(A_q)_{zzz} . \qquad (3.21)$$

Here, for $A_{q,\text{eff}}(\gamma, ppp)$ we have neglected the contributions from $(A_q)_{xzx}$, $(A_q)_{zxx}$, $(A_q)_{yzy}$ and $(A_q)_{zyy}$, which nearly cancel out themselves simply because $\beta_s \approx \beta_1$. The Fresnel factors L_{ii} in Eqs. (3.19)-(3.21) were calculated (Appendix B) and listed in Table 3.1. Note that the surface dielectric constant ϵ' in L_{ZZ} is unknown (Appendix C); therefore, with Eqs. (3.19)-(3.21), we can only determine the following quantities

$$\frac{(A_q)_{xxz}}{\epsilon'(\omega_2)} , \quad \frac{(A_q)_{yyz}}{\epsilon'(\omega_2)} , \quad \frac{(A_q)_{zzz}}{\epsilon'(\omega_1)^2 \epsilon'(\omega_2)} ,$$

$$\frac{(A_q)_{xzx}}{\epsilon'(\omega_1)} = \frac{(A_q)_{zxx}}{\epsilon'(\omega_1)} , \quad \frac{(A_q)_{yzy}}{\epsilon'(\omega_1)} = \frac{(A_q)_{zyy}}{\epsilon'(\omega_1)} ,$$

instead of $(A_q)_{ijk}$. Here, we have neglected the dispersion of ϵ' in the visible so that $\epsilon'(\omega_s) = \epsilon'(\omega_1)$. Using these five "reduced" $(A_q)_{ijk}$ elements as independent fitting parameters we can fit the experiment data well, as shown by the solid lines in Fig. 3.5, except for the

forward/backward asymmetry of $A_{s,\text{eff}}(ssp)$, which has been neglected so far.

In general we cannot separate $\epsilon'(\omega_i)$ from $(A_q)_{ijk}$ purely by SFG measurement. However, there exist the following equations that relate some of the $(A_q)_{ijk}$ elements specifically to the CH$_2$ stretch vibrations

$$(A_{\text{s}})_{xxz} + (A_{\text{s}})_{yyz} + (A_{\text{s}})_{zzz} = N_{\text{S}} \langle \hat{\zeta} \cdot \hat{z} \rangle_f [(a_{\text{s}})_{\xi\xi\zeta} + (a_{\text{s}})_{\eta\eta\zeta} + (a_{\text{s}})_{\zeta\zeta\zeta}] ,$$

$$(A_{\text{s}})_{xzx} + (A_{\text{s}})_{yzy} + (A_{\text{s}})_{zzz} = N_{\text{S}} \langle \hat{\zeta} \cdot \hat{z} \rangle_f (a_{\text{s}})_{\zeta\zeta\zeta} ,$$

$$(A_{\text{a}})_{xxz} + (A_{\text{a}})_{yyz} + (A_{\text{a}})_{zzz} = 0 ,$$

$$(A_{\text{a}})_{xzx} + (A_{\text{a}})_{yzy} + (A_{\text{a}})_{zzz} = N_{\text{S}} \langle \hat{\zeta} \cdot \hat{z} \rangle_f (a_{\text{a}})_{\eta\zeta\eta} . \tag{3.22}$$

The proof of the above equations is quite straightforward. In the following we consider the first equation as an example. We can express Eq. (3.7) in the form

$$(A_{\text{s}})_{ijk} = N_{\text{S}} \int \sum_{\lambda\mu\nu} (a_{\text{s}})_{\lambda\mu\nu} (\hat{\lambda} \cdot \hat{i})(\hat{\mu} \cdot \hat{j})(\hat{\nu} \cdot \hat{k}) f(\Omega) d\Omega . \tag{3.23}$$

Knowing that

$$\sum_{ij} \delta_{ij} (\hat{\lambda} \cdot \hat{i})(\hat{\mu} \cdot \hat{j}) = \delta_{\lambda\mu} , \tag{3.24}$$

we find

$$\sum_{ij} \delta_{ij} (A_{\text{s}})_{ijk} = N_{\text{S}} \sum_{\lambda\mu\nu} \delta_{\lambda\mu} (a_{\text{s}})_{\lambda\mu\nu} \int (\hat{\nu} \cdot \hat{k}) f(\Omega) d\Omega . \tag{3.25}$$

For the CH$_2$ symmetric stretch there are only three independent nonvanishing $(a_{\text{s}})_{\lambda\mu\nu}$ elements $(a_{\text{s}})_{\xi\xi\zeta}$, $(a_{\text{s}})_{\eta\eta\zeta}$, and $(a_{\text{s}})_{\zeta\zeta\zeta}$. Therefore, we have

$$\sum_{\lambda\mu} \delta_{\lambda\mu} (a_{\text{s}})_{\lambda\mu\nu} = \delta_{\nu\zeta} [(a_{\text{s}})_{\xi\xi\zeta} + (a_{\text{s}})_{\eta\eta\zeta} + (a_{\text{s}})_{\zeta\zeta\zeta}] . \tag{3.26}$$

Insertion of Eq. (3.26) into Eq. (3.25) yields

$$\sum_{ij} \delta_{ij} (A_{\text{s}})_{ijk} = N_{\text{S}} [(a_{\text{s}})_{\xi\xi\zeta} + (a_{\text{s}})_{\eta\eta\zeta} + (a_{\text{s}})_{\zeta\zeta\zeta}] \int (\hat{\zeta} \cdot \hat{k}) f(\Omega) d\Omega , \tag{3.27}$$

Table 3.2: Measured and calculated non-vanishing tensor elements A_{ijk} for the CH$_2$ symmetric (s) and antisymmetric (a) stretch modes. All values are in unit of 10^{-10} m^{2}V^{-1}sec^{-1}.

	s-stretch		a-stretch	
	measured	calculated	measured	calculated
A_{xxz}	225 ± 15	225	-30 ± 20	-12
A_{yyz}	475 ± 15	474	-135 ± 20	-146
A_{zzz}	345 ± 45	358	220 ± 70	158
$A_{xzx} = A_{zxx}$	~ 0	24	20 ± 25	52
$A_{yzy} = A_{zyy}$	~ 0	-31	230 ± 15	238
A_{xxx}	~ 0	-9	~ 0	-5
A_{yyx}	-19 ± 6	-19	~ 0	8
A_{zzx}	~ 0	-12	~ 0	-5
$A_{xyy} = A_{yxy}$	~ 0	3	~ 0	-9
$A_{xzz} = A_{zxz}$	~ 0	-8	~ 0	-5

which is identical to the first equation in Eq. (3.22) if $\hat{k} = \hat{z}$. Similarly, the other three equations in Eq. (3.22) can be proven.

These additional equations of constraint [Eq. (3.22)] allow us to deduce $\epsilon'(\omega_i)$ from experiment without knowing the actual orientational distribution of the CH$_2$ groups. Applying Eq. (3.22) to the five "reduced" $(A_q)_{ijk}$ elements deduced from experiment, we find $\epsilon'(\omega_1) = 2.1$ and $\epsilon'(\omega_2) = 1.5$. We can then obtain the five corresponding $(A_q)_{ijk}$ elements; their values are listed in Table 3.2 and labeled as "measured".

Finally we include the forward/backward asymmetry observed in the SFG spectra for the *ssp* polarization combination. Including contributions from $(A_q)_{yyx}$ and $(A_q)_{xxx}$, Eq. (3.19) becomes

$$
\begin{aligned}
A_{q,\text{eff}}(\gamma, ssp) = {} & \sin\beta_2 L_{YY}(\omega_s) L_{YY}(\omega_1) L_{ZZ}(\omega_2) \\
& \times [(A_q)_{yyz}\cos^2\gamma + (A_q)_{xxz}\sin^2\gamma] \\
& + \cos\beta_2 L_{YY}(\omega_s) L_{YY}(\omega_1) L_{XX}(\omega_2) \\
& \times [(A_q)_{yyx}\cos^3\gamma + (A_q)_{xxx}\cos\gamma\sin^2\gamma] .
\end{aligned}
\tag{3.28}
$$

It turns out that $(A_s)_{yyx}$ is the only additional element that can be determined with sufficient accuracy. The dashed line in Fig. 3.5a is the fit with a non-zero $(A_s)_{yyx}$. The deduced value of $(A_s)_{yyx}$ is listed in Table 3.2.

With these measured values of $(A_q)_{ijk}$, we can then use Eqs. (3.7) and (3.14) to obtain an approximate orientational distribution function $f(\theta, \phi, \psi)$ for the CH$_2$ groups. Knowing that the PVA chains are quite well aligned, we can assume a Gaussian distribution

$$f(\theta, \phi, \psi) = C \exp\left[-\frac{(\theta - \theta_0)^2}{2\sigma_\theta^2} - \frac{(\phi - \phi_0)^2}{2\sigma_\phi^2} - \frac{(\psi - \psi_0)^2}{2\sigma_\psi^2}\right] , \qquad (3.29)$$

where C is a normalization constant; $\phi_0 = \psi_0 = 0°$ by symmetry; and θ_0, σ_θ, σ_ϕ, and σ_ψ are parameters to be determined. For this calculation, the distribution function $f(\theta, \phi, \psi)$ is defined such that the probability of finding a CH$_2$ group oriented at (θ', ϕ', ψ') in the range $\theta < \theta' < \theta + d\theta$, $\phi < \phi' < \phi + d\phi$, and $\psi < \psi' < \psi + d\psi$ is equal to $f(\theta, \phi, \psi)d\theta d\phi d\psi$. We find, for the best fit,

$$\theta_0 = 2.5° \pm 0.7° ,$$

$$\sigma_\theta = 26° \pm 5° ,$$

$$\sigma_\phi = 27° \pm 5° ,$$

$$\sigma_\psi = 35° \pm 5° .$$

These values, when used with Eq. (3.29) in Eq. (3.7) to calculate $(A_q)_{ijk}$, reproduce almost all the measured $(A_q)_{ijk}$ values within the experimental error, as shown in the column "calculated" in Table 3.2. One may notice that the number of experimentally deduced $(A_q)_{ijk}$ far exceeds the number of input parameters (θ_0, σ_θ, σ_ϕ, σ_ψ, $\epsilon'(\omega_1)$, $\epsilon'(\omega_2)$ and N_S) used for this calculation. The fact that we can still consistently reproduce all the measured $(A_q)_{ijk}$

values indicates that Eq. (3.29) is a good representation of the orientational distribution.

The above results are for the surface CH_2 groups. Since the CH_2 molecular plane is perpendicular to the PVA chain locally, the same set of parameters θ and ϕ also describe the orientation of the polymer chains. The values listed above indicate that the PVA chains lie almost flat and are well aligned on the surface with an average $2.5°$ upward tilt along the rubbing direction.

3.4.5 SHG study of an 8CB monolayer on rubbed PVA

As described in Sec. 3.2.3, the molecular orientational distribution of an 8CB monolayer adsorbed on a rubbed polymer surface can be determined from SHG measurements. Deposition of the 8CB monolayer was monitored by SHG *in situ* [99]. We present in Fig. 3.9 the SHG intensities from the 8CB monolayer on rubbed PVA as a function of the sample azimuthal angle γ for different input/output polarization combinations.

The 8CB monolayer on rubbed PVA also has a macroscopic C_{1v} symmetry, which restricts the number of nonvanishing independent $\chi^{(2)}_{ijk}$ elements to six under the approximation that $\alpha_{\zeta\zeta\zeta}$ dominates over other nonvanishing elements of $\boldsymbol{\alpha}^{(2)}$ of 8CB. As listed in Ref. [72], they are

$$\chi^{(2)}_{zzz} \ ,$$

$$\chi^{(2)}_{xxx} \ ,$$

$$\chi^{(2)}_{xyy} = \chi^{(2)}_{yxy} = \chi^{(2)}_{yyx} \ ,$$

$$\chi^{(2)}_{xzz} = \chi^{(2)}_{zxz} = \chi^{(2)}_{zzx} \ ,$$

$$\chi^{(2)}_{zxx} = \chi^{(2)}_{xzx} = \chi^{(2)}_{xxz} \ ,$$

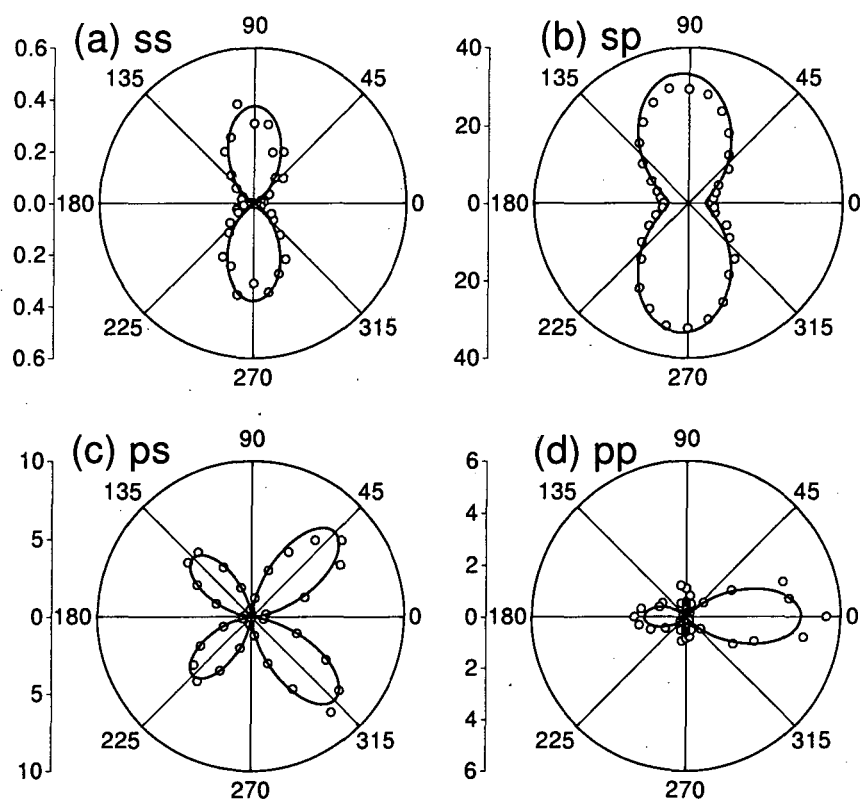Figure 3.9: Polar plots of SHG intensities (arbitrary units) from an 8CB monolayer on a rubbed PVA surface. $0°$ and $180°$ are the rubbing and anti-rubbing directions, respectively. Circles are the experimental data and solid lines are the theoretical fits. The input-output polarization combinations are (a)s_{in}-s_{out}, (b)s_{in}-p_{out}, (c)p_{in}-s_{out}, and (d)p_{in}-p_{out}.

86

Table 3.3: Nonvanishing independent $\chi_{ijk}^{(2)}$ elements of the 8CB monolayer on rubbed PVA deduced from the SHG expriment with the zzz component normalized to 1.

$\chi_{zzz}^{(2)}/\epsilon'^3$	1
$\chi_{xxx}^{(2)}$	3.0 ± 0.5
$\chi_{xyy}^{(2)}$	0.32 ± 0.25
$\chi_{xzz}^{(2)}/\epsilon'^2$	0.15 ± 0.09
$\chi_{zxx}^{(2)}/\epsilon'$	11.5 ± 0.8
$\chi_{zyy}^{(2)}/\epsilon'$	4.4 ± 0.4

$$\chi_{zyy}^{(2)} = \chi_{yzy}^{(2)} = \chi_{yyz}^{(2)} \ ,$$

and can be deduced by fitting the data in Fig. 3.9 using Eqs. (3.2) and (3.3). The fit is plotted as solid lines in Fig. 3.9, and the deduced nonvanishing $\chi_{ijk}^{(2)}$ elements are presented in Table 3.3.

As in Ref. [72], we can assume for 8CB molecules in the monolayer an orientational distribution of the form

$$g(\theta_{LC}, \phi_{LC}) = C \exp\left[-\frac{(\theta_{LC} - \theta_{LC,0})^2}{2\sigma^2}\right][1 + d_1 \cos\phi_{LC}$$
$$+ d_2 \cos(2\phi_{LC}) + d_3 \cos(3\phi_{LC})] \ , \tag{3.30}$$

where θ_{LC}, ϕ_{LC} are the polar and the azimuthal angles defined in Fig. 3.2 , and $\theta_{LC,0}$, σ, d_1, d_2 and d_3 are five independent parameters to be determined from the five measured ratios in Table 3.3 using Eq. (3.16) with a given value of ϵ'. The results are presented in Table 3.4. In this case, ϵ' cannot be determined separately, and the assumption $\epsilon'(\omega)=\epsilon'(2\omega)$ used here also may not be true because of the electronic resonance of 8CB molecules at the second-harmonic frequency. Nevertheless, as shown in Table 3.4, varying ϵ' from 1 to 2.25 mainly changes the deduced values of $\theta_{LC,0}$ and σ, and has little effect on the parameters d_1, d_2 and d_3 which describe the azimuthal distribution.

Table 3.4: Deduced parameters in $g(\theta_{LC}, \phi_{LC})$ for various values of the surface dielectric constant ϵ' of the 8CB monolayer.

ϵ'	θ_0 (deg)	σ (deg)	d_1	d_2	d_3
1.0	80±5	6±3	.07±.03	.85±.03	.04±.02
1.25	78±6	8±4	.07±.03	.85±.03	.04±.02
1.5	75±8	9±4	.07±.03	.85±.03	.04±.02
1.75	72±9	10±5	.07±.03	.85±.03	.04±.02
2.0	69±10	11±5	.07±.03	.85±.03	.04±.02
2.25	66±12	12±6	.07±.03	.85±.03	.04±.02

3.5 Discussion

3.5.1 Surface density of CH$_2$ groups

As seen in Eq. (3.7), N_S, the surface density of CH$_2$ groups, is a parameter needed in our quantitative analysis of the SFG data. To obtain the best-fit values of $(A_q)_{ijk}$ listed in the "calculated" column in Table 3.2, we used

$$N_S = (1.7 \pm 0.2) \times 10^{15} \text{ cm}^{-2} , \tag{3.31}$$

which seems too large considering that the CH$_2$ surface density calculated from the PVA crystalline structure [100] is only about 7×10^{14} cm^{-2}. This is presumably because in our calculation we have neglected the factor $l_\parallel(\omega_s)l_\parallel(\omega_1)l_\parallel(\omega_2)$ resulting from the microscopic local-field effect. As discussed in Appendix C, N_S in Eq. (3.7) should be replaced by $N_S l_\parallel(\omega_s)l_\parallel(\omega_1)l_\parallel(\omega_2)$. A theoretical estimate of such an effect [Eq. (C.5)] shows that $l_\parallel$ is usually larger than 1, which makes the value of N_S closer to the expected one.

3.5.2 Effect of rubbing on PVA surface structure

We have presented the SFG spectra (Fig. 3.4) for the *ssp* and *sps* polarization combinations for the unrubbed PVA sample. The spectra from the rubbed and unrubbed
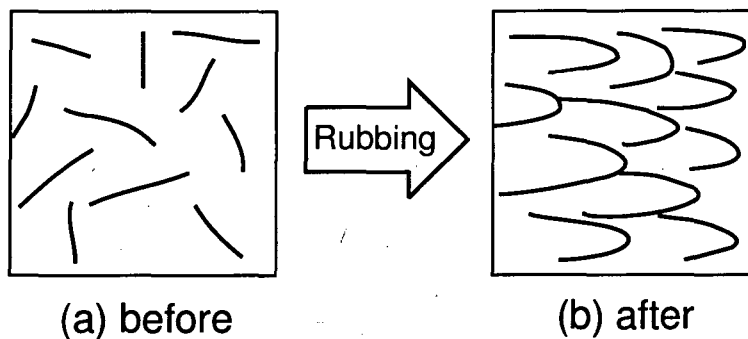
(a) before   (b) after

Figure 3.10: Proposed polymer chain distribution (top view) on a PVA surface (a)before, and (b)after rubbing.

samples look similar except that there is no azimuthal spectral variation for the unrubbed one. The dashed lines in Fig. 3.4 are predicted spectra for the unrubbed sample assuming the same Gaussian distribution for θ and ψ deduced earlier for the rubbed one, but a uniform distribution in ϕ. The absolute intensities of the measured spectra are slightly lower than predicted. A somewhat broader distribution in θ and ψ ($\sigma_\theta = 35°$, $\sigma_\psi = 45°$) fits the spectra well (solid lines).

Based on these results, a possible scenario for rubbing-induced PVA chain ordering is proposed in Fig. 3.10 (partially inspired by a "rubbing" effect on a street in Berkeley, see Fig. 3.11). Before rubbing, some sections of the PVA chains were lying more or less flat on the surface and isotropic in the plane, with their ends presumably buried in the bulk. During rubbing, fibers on the rubbing material would grab the surface polymer chains, stretch them in the rubbing direction and even pull some chain sections out from the sub-surface, resulting in stacked elongated half loops one on top of another. This would explain not only the azimuthal chain ordering in the rubbing direction, but also the forward/backward asymmetry.

Figure 3.11: "Rubbing" effect on Bancroft Way, Berkeley. This crosswalk on the street has been rubbed repeatedly by the wheels of passing vehicles going downhill. Note that the white mark tends to "align" in the rubbing direction. Our group often cross this street to go to lunch together. This scene strikingly resembles the mechanism of rubbing induced polymer chain alignment that we proposed in Fig. 3.10.
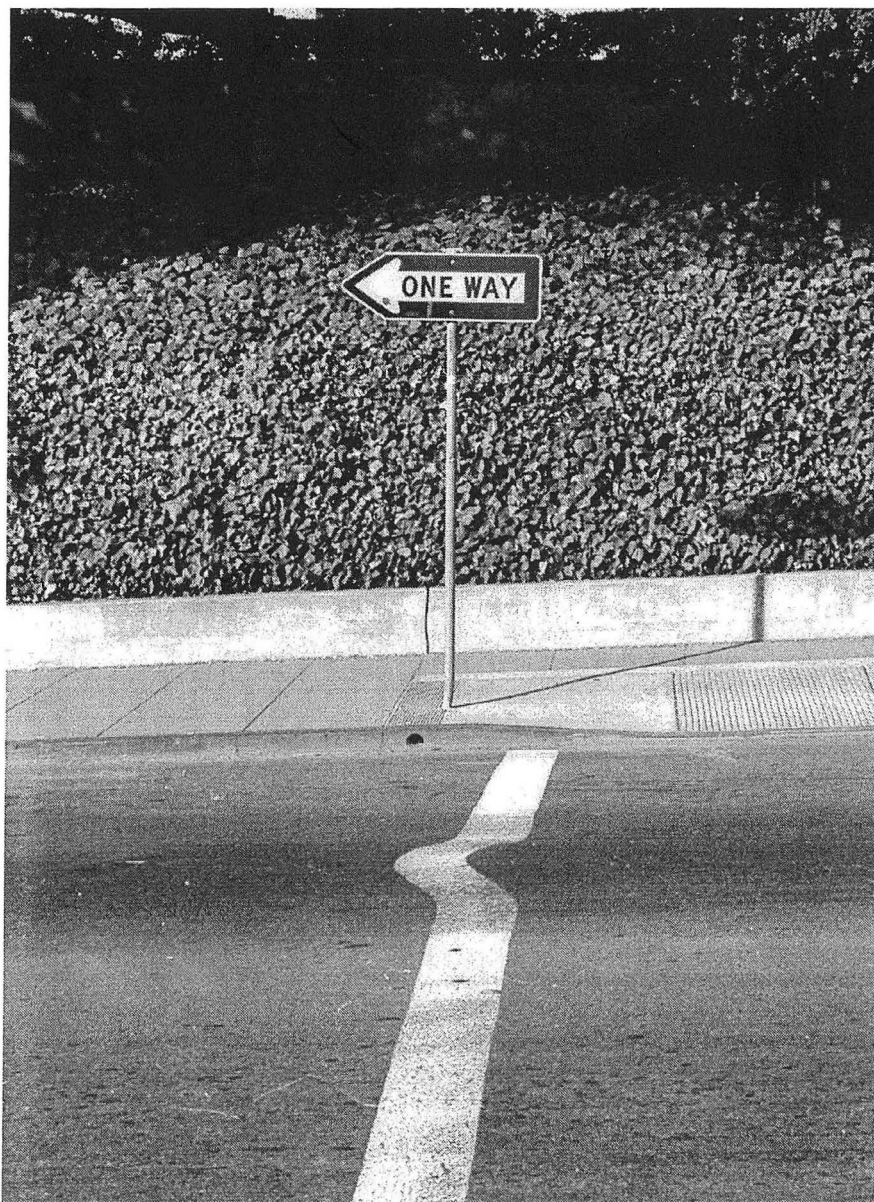
3.5.3 Molecular interaction between 8CB and PVA

From the SFG and SHG studies we have obtained the orientational distribution functions $f(\theta, \phi, \psi)$ for the surface PVA chains and $g(\theta_{LC}, \phi_{LC})$ for the molecules in the 8CB monolayer independently. It is important to find the correlation between them. In order to do so, we calculate a grand azimuthal distribution function $F(\phi)$ for PVA chains by integrating $f(\theta, \phi, \psi)$ over θ and ψ, and also $G(\phi_{LC})$ for the 8CB molecules by integrating $g(\theta_{LC}, \phi_{LC})$ over θ_{LC}. However, we notice that unlike an 8CB molecule, a section of PVA chain has no polarity, i.e., (θ, ϕ) and $(-\theta, \phi + 180°)$ describe the same chain orientation. To define $f(\theta, \phi, \psi)$ over all orientations, we can limit θ between 0° and 90° and vary ϕ over the entire 360°. We naturally use the same limiting ranges for θ_{LC} and ϕ_{LC} to define $g(\theta_{LC}, \phi_{LC})$ for polar 8CB molecules.

A polar plot of $\sqrt{F(\phi)}$ and $\sqrt{G(\phi_{LC})}$ are presented in Fig. 3.12. The correlation between the two is remarkable. As we expected, the rubbed PVA surface appears to be more ordered in the azimuthal distribution than the adsorbed 8CB monolayer. This suggests that the rubbed polymer surface indeed serves as a molecular template to align LC molecules through short-range molecular interaction [101].

The forward/backward asymmetry of the 8CB orientational distribution (represented by the positive coefficient $d_1 = 0.07$) indicates that the 8CB molecules prefer to align in the forward direction. This must be somehow related to the average upward tilt angle ($\theta_0 = 2.5°$) of the PVA chains. Similar results have also been found from other rubbed polymers [82, 87, 88], yet no theoretical model is available to correlate these two tilt angles quantitatively. There are, however, some qualitative explanations. For example, it
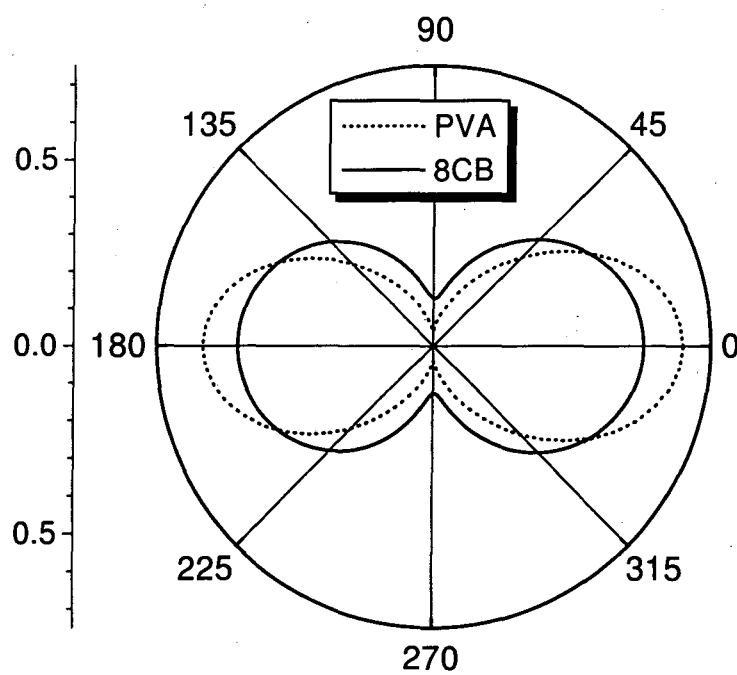
Figure 3.12: Polar plot of the grand azimuthal distribution functions of the PVA chains (dashed line) and 8CB molecules (solid line) on a rubbed PVA surface. Square root values are used so that the total areas inside the two curves remain constant.

has been assumed that rubbing induces a saw-tooth-like polymer surface which leads to a homogeneous LC alignment with a forward pretilt angle [102]. This is consistent with the scenario we proposed for the rubbed PVA surface (Fig. 3.10), in which the 8CB molecules adsorbed on the back-slanted terraces would appear to align more in the forward direction. As demonstrated in Ref [74], the LC monolayer then governs the forward pretilt angle of a bulk LC film.

3.6 Conclusion

We have used SFG surface vibrational spectroscopy to determine, for the first time, a quantitative orientational distribution of the polymer chains at the very top surface of a rubbed PVA sample. We have also used SHG to determine the orientational distribution of a monolayer of 8CB molecules adsorbed on rubbed PVA. Comparison of the two in the azimuthal plane shows that they are well correlated. This strongly supports the belief that "orientational epitaxy" is the mechanism responsible for the surface-induced LC bulk alignment by rubbed polymer surfaces. We have proposed a possible scenario for how rubbing changes the polymer chain conformation at the surface, which is subject to future experimental tests. This work is also a demonstration to show that SFG vibrational spectroscopy can be an effective tool to probe quantitatively the surface structure of a polymer, with or without external perturbation.

Chapter 4

Experimental evaluation of surface vs. bulk contributions

4.1 Introduction

Among many useful applications of SFG surface spectroscopy, studies of the inter-facial structure of neat materials are of particular interest since few other techniques can yield as much information. Ice and rubbed PVA discussed in previous chapters are two such examples.

In interpreting the observed SFG spectra in reflection, one usually assumes that the spectra originate from the top surface monolayer. From a general physical argument, however, we can only conclude that the bulk electric-quadrupole contribution from a cen-trosymmetric medium is smaller than, or of the same order of magnitude as, the surface contribution to SFG in reflection [2, 103]. Without any prior knowledge about the surface

structure, it is not clear whether the bulk contribution can always be neglected. To be certain, we need to know the surface and bulk contributions separately. This, in general, cannot be done [103, 104, 105]. However, from SFG measurements in both reflection and transmission [106], we can obtain a good estimate of the bulk nonlinearity, which allows us to judge whether it is negligible or not.

Section 4.2 discusses the theoretical background and assumptions behind our measurements. Section 4.3 presents the experimental scheme for measurements and comparison of reflected and transmitted SFG spectra. The technique has been applied to three different samples. The first one is a silane monolayer adsorbed on fused quartz (Sec. 4.4.1) from which the reflected and transmitted SFG spectra appear to be well correlated as they should be. The second one is a polyethylene film (Sec. 4.4.2). There, the reflected and transmitted SFG spectra are significantly different, indicating that the bulk contribution is important for the transmitted SFG. The third one is the fused silica/water interface (Sec. 4.4.3), which also shows some bulk contribution in transmission. We can then deduce the value of the bulk nonlinearity and show that its contribution to the reflected SFG is indeed negligible. In fact, the measured bulk nonlinearity also gives us an estimate of how weak the reflected SFG would have to be for the bulk contribution to be non-negligible.

4.2 Theory

In a typical surface SFG experiment, two input laser beams at frequencies ω_1 and ω_2 overlap at a surface or interface to induce a surface nonlinear polarization

$$\mathbf{P}_S^{(2)}(\omega_s) = \epsilon_0 \chi_S^D : \mathbf{E}(\omega_1)\mathbf{E}(\omega_2) \tag{4.1}$$

and generate a coherent SFG output at ω_s in two well defined directions (reflection and transmission, see Fig. 4.1). Both directions are determined by the requirement that the parallel (x) components of the input and output wavevectors are matched:

$$k_{1x} + k_{2x} = k_{sx} \ . \tag{4.2}$$

Scanning ω_2 over the frequency range of the surface molecular vibrational modes yields an SFG spectrum.

For a centrosymmetric bulk medium, although its nonlinear susceptibility $\chi_{\mathrm{B}}^{\mathrm{D}}$ vanishes under the electric-dipole approximation, it still has a bulk nonlinear polarization resulting from electric-quadrupole contributions [2, 103, 105]

$$\mathbf{P}_{\mathrm{B}}^{(2)}(\omega_s) \ = \ \epsilon_0 \boldsymbol{\chi}^{\mathrm{Q1}} \vdots \nabla \mathbf{E}(\omega_1) \mathbf{E}(\omega_2) + \epsilon_0 \boldsymbol{\chi}^{\mathrm{Q2}} \vdots \mathbf{E}(\omega_1) \nabla \mathbf{E}(\omega_2) - \epsilon_0 \nabla \cdot [\boldsymbol{\chi}^{\mathrm{Q}} : \mathbf{E}(\omega_1)\mathbf{E}(\omega_2)] \ .$$

$$\tag{4.3}$$

This general form has also included the magnetic dipole contribution [107]. If $\mathbf{E}(\omega_1)$ and $\mathbf{E}(\omega_2)$ can be treated as plane waves with wavevectors $\mathbf{k}_1'$ and $\mathbf{k}_2'$, then Eq. (4.3) becomes

$$P_{\mathrm{B}i}^{(2)} \ = \ i\epsilon_0 \sum_{jlm} \left[\chi_{ijlm}^{\mathrm{Q1}} k_{1m}' + \chi_{ijlm}^{\mathrm{Q2}} k_{2m}' - \chi_{ijlm}^{\mathrm{Q}} (k_{1m}' + k_{2m}') \right] E_j(\omega_1) E_l(\omega_2) \ . \tag{4.4}$$

This bulk contribution to SFG can be described in terms of an effective surface nonlinear susceptibility [108]

$$\chi_{ijk}^{\mathrm{SB}} \ = \ \sum_m \frac{\chi_{ijlm}^{\mathrm{Q}}(k_{1m}' + k_{2m}') - \chi_{ijlm}^{\mathrm{Q1}} k_{1m}' - \chi_{ijlm}^{\mathrm{Q2}} k_{2m}'}{k_{sz}' - k_{1z}' - k_{2z}'} \ . \tag{4.5}$$

The absolute value of the denominator in Eq. (4.5) yields the factor $l_c = \frac{1}{|k_{sz}' - k_{1z}' - k_{2z}'|}$, which is usually defined as the coherence length. Since k_{sz}' is positive and negative for the reflected and transmitted SFG, respectively, l_c is very different for the two geometries. By

measuring SFG in both reflection and transmission directions, we can deduce some components of χ_{ijk}^{SB} and therefore obtain an estimate of χ^{Q}, χ^{Q1} and χ^{Q2} if we assume their nonvanishing elements are of the same order of magnitude.

It is well known that some part of the bulk contribution cannot be separated from the surface contribution in SFG and SHG (second-harmonic generation) measurements [104]. There are also extra bulk contributions arising from rapid variations of the fields and the structure at an interface [105]. They behave like a surface nonlinear susceptibility and also cannot be separated from χ_S^{D} experimentally. However, these are all electric-quadrupole in nature, and their contributions to the effective surface nonlinearity presumably have the same order of magnitude as χ^{Q}, χ^{Q1} and χ^{Q2}. Thus the deduction of an order-of-magnitude value of χ^{Q}, χ^{Q1} and χ^{Q2} from the measurement of χ_{ijk}^{SB} allows us to have an order-of-magnitude estimate of the importance of all the bulk contributions to SFG. In the following, we combine χ_S^{D} and the inseparable bulk contributions into one quantity $\chi_S^{(2)}$, and express the total effective surface nonlinear susceptibility for SFG in the form

$$\chi_{\text{tot}}^{(2)} = \chi_S^{(2)} + \frac{\chi_B^{(2)}(\mathbf{k}_1', \mathbf{k}_2')}{k_{sz}' - k_{1z}' - k_{2z}'} \ . \tag{4.6}$$

4.3 Experiment

The experimental arrangement is depicted in Fig. 4.1. The input beams, one at 1.064 μm, and the other tunable between 2.5 μm and 9 μm, were generated from a Nd:YAG laser and a laser-pumped optical parametric system. Both beams have a pulse width of $\sim$15 psec, a repetition rate of 20 Hz, and a typical beam diameter of $\sim$1 mm at the sample surface. Since alignment is crucial for this experiment, we give below a detailed account of

Table 4.1: Calculated SFG exit angle β_s for different infrared frequencies. The "visible" beam ω_1 is at 1064 nm, and the incidence angles of ω_1 and ω_2 are 45° and 57° from the sample surface normal, respectively, as shown in Fig. 4.1(a).

Wave number $\omega_2/(2\pi c)$	SFG exit angle β_s
2800 cm^{-1}	20.6°
2900 cm^{-1}	20.0°
3000 cm^{-1}	19.5°

our alignment procedure.

First, to align for the reflected SFG measurements (Fig. 4.1a), we used a z-cut quartz reference sample to optimize the signal. The SFG reflection angle β_s varied with the input infrared wavelength (Table 4.1) but could be compensated by lens L1, which imaged the beam spot on the sample surface to pinhole P2 in front of the detector. A He-Ne laser beam was then directed to trace the SFG beam path into detector D with the help of pinholes P1 and P2. With the real sample replacing the reference sample, the alignment was done by adjusting the sample position such that the reflected 1.064 μm input beam and the He-Ne laser beam retraced their previous beam paths.

If the dispersion between the He-Ne and SFG wavelengths (633 nm and ~810 nm, respectively, in our experiment) is negligible, the He-Ne laser beam used to trace the reflected SFG beam should also trace the transmitted SFG beam. Therefore, for alignment of the transmitted SFG measurements (Fig. 4.1b), we used mirrors M2 and M3 underneath the sample to reflect the transmitted He-Ne guide beam into the same path defined by P1 and P2 for the reflected beam. To compensate for the variation of the SFG exit angle due to dispersion, we used another lens (L2) between M2 and M3 to image the beam spot on the sample surface 1:1 back onto itself. The transmitted and reflected He-Ne, and hence SFG, beams were then along the same path through P1 and P2 into the detector.
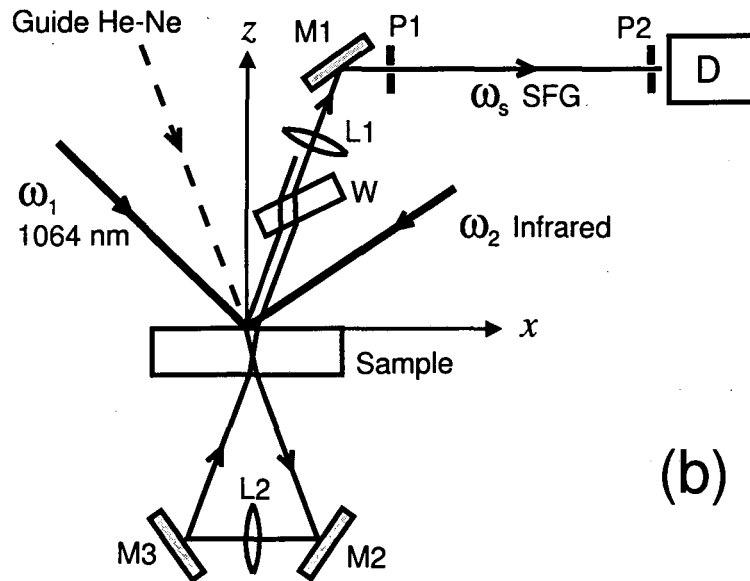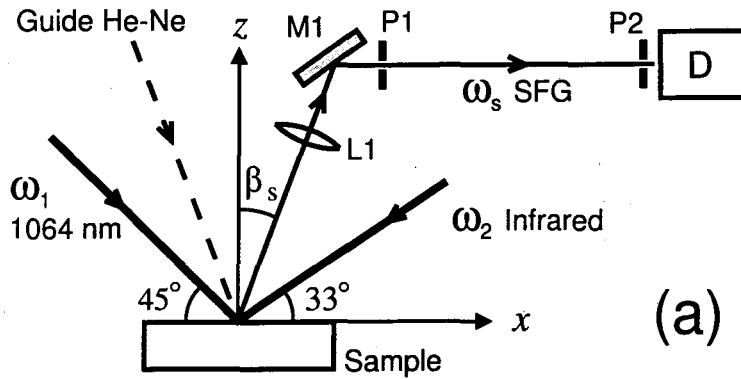
Figure 4.1: Experimental setup for measuring SFG in (a)reflection, and (b)transmission. M1, M2 and M3: metal mirrors to reflect the SFG signal; P1 and P2: iris diaphragms to direct the SFG and the guide He-Ne beams; D: photo-detector; L1: lens to image the beam spot on the sample surface to diaphragm P2; L2: lens to image the beam spot on the sample surface back to itself with a slight parallel shift; W: flat window to shift the SFG beam.

In the actual SFG measurements, we had to separate reflected and transmitted SFG signals. This was accomplished by a small parallel shift of M3 to the right that displaced the transmitted SFG beam slightly from the reflected SFG beam on their way to the detector. Then only the reflected SFG output could go through the pinholes to reach the detector. To measure the transmitted SFG, we inserted flat window W in front of L1 to compensate for the shift of the transmitted SFG beam caused by the shift of M3 and, at the same time, shift the reflected SFG beam away. Only the transmitted SFG output could then reach the detector.

The above alignment procedure was found to be reliable and easy to implement. Since the reflected and transmitted SFG signals were recorded by the same detection system, the results were amenable to quantitative comparison.

4.4 Results and analysis

4.4.1 Octadecyltrichlorosilane monolayer

We have measured SFG spectra in both reflection and transmission from an octadecyltrichlorosilane (OTS) monolayer on a fused silica substrate. The sample was prepared by the usual self-assembly technique [52]. The thickness of the fused silica substrate is about 3 mm, sufficient to eliminate the SFG contribution from the bottom surface. OTS has a long alkyl chain and is known to form a well-ordered self-assembled monolayer on glass. SFG spectra of the C-H stretch modes in reflection from such a monolayer were reported earlier [96]. In this case, because the resonant SFG signal originated from a surface monolayer, the reflected and transmitted spectra were expected to be correlated.

The surface nonlinear susceptibility $\chi_S^{(2)}$ of an OTS monolayer with $C_{\infty v}$ symmetry has only 3 independent non-vanishing elements:

$$\chi_{S,zzz}^{(2)} \; ,$$

$$\chi_{S,xxz}^{(2)} = \chi_{S,yyz}^{(2)} \; ,$$

$$\chi_{S,xzx}^{(2)} = \chi_{S,zxx}^{(2)} = \chi_{S,yzy}^{(2)} = \chi_{S,zyy}^{(2)} \; .$$

In the last row we have used the approximation $\chi_{S,ijk}^{(2)} = \chi_{S,jik}^{(2)}$ because ω_1 and ω_s are far away from electronic resonances.

Near vibrational resonances $\chi_S^{(2)}$ takes the form

$$\chi_S^{(2)}(\omega_2) = \chi_S^{NR} + \sum_q \frac{A_q}{\omega_2 - \omega_q + i\Gamma_q} \; , \tag{4.7}$$

where χ_S^{NR} describes the nonresonant background, and A_q, ω_q and Γ_q are the amplitude, resonant frequency and damping constant, respectively, of the qth molecular vibrational mode.

In MKS units the SFG output intensity is given by

$$I(\omega_s) = \frac{\omega_s^2}{8\epsilon_0 c^3 \cos^2 \beta_s} |\chi_{tot,eff}^{(2)}|^2 I(\omega_1) I(\omega_2) \; , \tag{4.8}$$

where $I(\omega_i)$ is the beam intensity at ω_i, and $\chi_{tot,eff}^{(2)}$ is the total effective surface nonlinear susceptibility defined as

$$
\begin{aligned}
\chi_{tot,eff}^{(2)} &= \chi_{S,eff}^{(2)} + \chi_{B,eff}^{(2)} \\
&= [\mathbf{L}(\omega_s) \cdot \hat{\mathbf{e}}_s] \cdot \chi_{tot}^{(2)} : [\mathbf{L}(\omega_1) \cdot \hat{\mathbf{e}}_1][\mathbf{L}(\omega_2) \cdot \hat{\mathbf{e}}_2] \; ,
\end{aligned}
\tag{4.9}
$$

with $\hat{\mathbf{e}}_i$ being the unit polarization vector of the optical field at ω_i and $\mathbf{L}(\omega_i)$ being the tensorial Fresnel factor. In the present case, $\chi_{B,eff}^{(2)}$ comes from the fused silica substrate.

Table 4.2: Parameters of the three beams and the calculated Fresnel factors for the air/fused quartz interface. (R) and (T) represent reflection and transmission, respectively. $L(\omega_s, T)$ includes the transmission coefficient of the bottom surface of the fused quartz substrate. The dielectric constant of the surface monolayer $\epsilon' = 1$ was used for the calculation of L_{zz}.

	$\omega_s(R)$	$\omega_s(T)$	ω_1	ω_2
λ	810 nm	810 nm	1064 nm	3.4 μm
n	1.453	1.453	1.450	1.410
β	20.0°	20.0°	45°	57°
L_{xx}	.83	.97	.92	1.02
L_{yy}	.80	.96	.72	.65
L_{zz}	1.17	.97	1.08	.98
$L_{xx}e_x$ (p)	-.78	.91	.65	-.56
$L_{yy}e_y$ (s)	.80	.96	.72	.65
$L_{zz}e_z$ (p)	.40	.33	.77	.82

The Fresnel factors at the center of our tuning range have been calculated and listed in Table 4.2. Because the tuning range is relatively small (200 cm^{-1}) in this experiment, the dispersion of Fresnel factors due to the variation of ω_2 can be neglected. Using these values, we can express all the surface effective nonlinear susceptibilities in terms of the 3 independent non-vanishing $\chi^{(2)}_{S,ijk}$ elements:

$$\chi^{(2)}_{S,eff}(ssp, R) = .47\chi^{(2)}_{S,xxz} ,$$

$$\chi^{(2)}_{S,eff}(ssp, T) = .56\chi^{(2)}_{S,xxz} ,$$

$$\chi^{(2)}_{S,eff}(ppp, R) = .25\chi^{(2)}_{S,zzz} - .42\chi^{(2)}_{S,xxz} + .19\chi^{(2)}_{S,xzx} ,$$

$$\chi^{(2)}_{S,eff}(ppp, T) = .21\chi^{(2)}_{S,zzz} + .49\chi^{(2)}_{S,xxz} - .51\chi^{(2)}_{S,xzx} ,$$

$$\chi^{(2)}_{S,eff}(sps, R) = .40\chi^{(2)}_{S,xzx} ,$$

$$\chi^{(2)}_{S,eff}(sps, T) = .48\chi^{(2)}_{S,xzx} . \qquad (4.10)$$

These equations show a strict correlation between the reflected and transmitted SFG spectra from the surface contribution, in contrast to the effective bulk nonlinear susceptibility $\chi^{(2)}_{B,eff}$,

Table 4.3: Molecular vibrational modes on an OTS monolayer and their corresponding nonlinear amplitudes obtained from fitting of the SFG spectra. The unit of A is $10^{-9}\mathrm{m}^2\mathrm{V}^{-1}\mathrm{sec}^{-1}$.

Mode	$\omega_q/(2\pi c)$	$\Gamma_q/(2\pi c)$	A_{xxz}	A_{zzz}	A_{xzx}
s-CH$_3$	2882 cm^{-1}	7.5 cm^{-1}	7.9	1.2	0
Fermi-Res.	2943 cm^{-1}	10.5 cm^{-1}	10.2	0.1	-1.5
a-CH$_3$	2970 cm^{-1}	9.5 cm^{-1}	-3.4	6.3	6.4

which can be strongly enhanced by the longer coherence length in the transmission direction.

Fig. 4.2 shows the reflected and transmitted SFG spectra obtained from the OTS monolayer. To take into account the different losses of signal in reflection and transmission, all spectra were normalized against the SFG intensity from a z-cut crystalline quartz reference sample (see Sec. 1.3.2 for details), which makes it possible to plot all spectra in MKS units. The reflected and transmitted spectra in Fig. 4.2 seem to be somewhat different, especially for the *sps* polarization combination (i.e., *s*-, *p*-, and *s*-polarized SFG output at ω_s, 1064 nm input at ω_1 and tunable infrared input at ω_2, respectively), but this can be explained by the different non-resonant bulk contributions $\chi^{(2)}_{\mathrm{B,eff}}$ for the two different geometries. In fact, we were able to fit all the spectra (shown by the solid lines in Fig. 4.2) using Eqs. (4.7) and (4.10) with the same set of $\mathbf{A}_q$, ω_q and Γ_q values and different nonresonant contributions $\chi^{\mathrm{NR}}_{\mathrm{tot,eff}}$, as listed in Tables 4.3 and 4.4. The typical relative error of the deduced $\mathbf{A}_q$ or $\chi^{(2)}$ in SFG is about 10%. The close fit in Fig. 4.2 indicates that SFG spectra in reflection and transmission from the OTS monolayer are indeed very well correlated.

With the values of $\chi^{\mathrm{NR}}_{\mathrm{tot,eff}}$ in both reflection and transmission, we could further deduce $\chi^{\mathrm{NR}}_{\mathrm{S,eff}}$ and $\chi^{\mathrm{NR}}_{\mathrm{B,eff}}$. Here we take the *sps* polarization combination as an example.
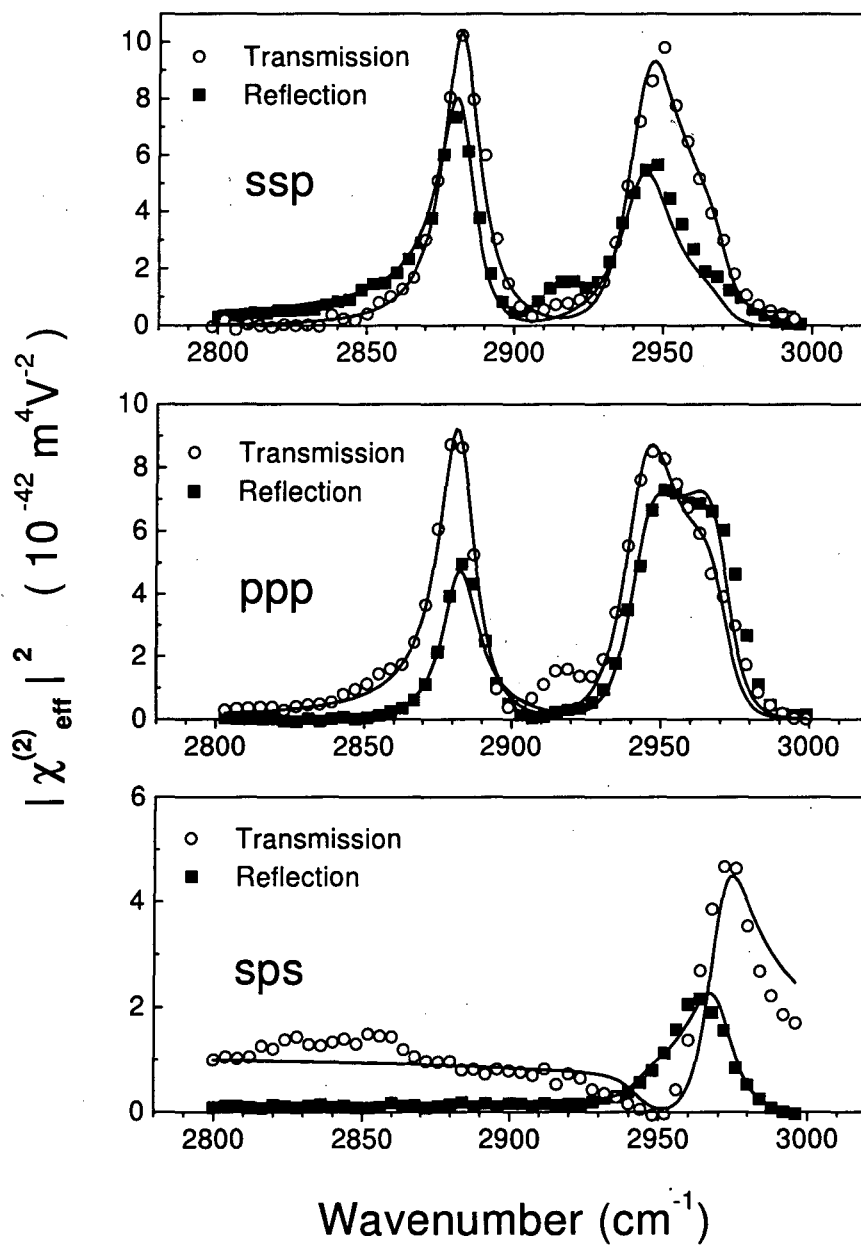
Figure 4.2: SFG spectra of an OTS monolayer on fused silica. Points are experiment data and the curves are theoretical fits.

From Eqs. (4.6) and (4.9), we have

$$\chi^{(2)}_{S,eff}(sps) = L_{yy}(\omega_s)e_{sy}\chi^{(2)}_{S,yzy}L_{zz}(\omega_1)e_{1z}L_{yy}(\omega_2)e_{2y} \ ,$$

$$\chi^{(2)}_{B,eff}(sps) = \frac{L_{yy}(\omega_s)e_{sy}L_{yy}(\omega_2)e_{2y}}{k'_{sz} - k'_{1z} - k'_{2z}}[\chi^{(2)}_{B,yzy}L_{zz}(\omega_1)e_{1z} + \chi^{(2)}_{B,yxy}L_{xx}(\omega_1)e_{1x}] \ . \ (4.11)$$

Here, we have two nonvanishing components, $\chi^{(2)}_{B,yzy}$ and $\chi^{(2)}_{B,yxy}$, contributing to the bulk term because, as shown by Eq. (4.5), $\chi^{(2)}_B$ depends linearly on the wavevectors $\mathbf{k}'_1$ and $\mathbf{k}'_2$, which break the inversion symmetry along the x and z axes. Eqs. (4.11) and (4.11) are valid for both resonant and nonresonant contributions. Only two parameters are different for the reflection and transmission geometries. One is $L_{yy}(\omega_s)e_{sy}$, which can be found in Table 4.2, and the other is $\frac{1}{|k'_{sz} - k'_{1z} - k'_{2z}|}$, which is equal to 49 nm and 720 nm for reflection and transmission, respectively. Inserting these values in Eqs. (4.11) and (4.11) we find

$$\chi^{(2)}_{tot,eff}(sps, R) = \chi^{(2)}_{S,eff}(sps, R) + \chi^{(2)}_{B,eff}(sps, R)$$

$$= .52\{\chi^{(2)}_{S,yzy}L_{zz}(\omega_1)e_{1z} + 49nm \left[\chi^{(2)}_{B,yzy}L_{zz}(\omega_1)e_{1z} + \chi^{(2)}_{B,yxy}L_{xx}(\omega_1)e_{1x}\right]\},$$

$$(4.12)$$

$$\chi^{(2)}_{tot,eff}(sps, T) = \chi^{(2)}_{S,eff}(sps, T) + \chi^{(2)}_{B,eff}(sps, T)$$

$$= .62\{\chi^{(2)}_{S,yzy}L_{zz}(\omega_1)e_{1z} - 720nm \left[\chi^{(2)}_{B,yzy}L_{zz}(\omega_1)e_{1z} + \chi^{(2)}_{B,yxy}L_{xx}(\omega_1)e_{1x}\right]\},$$

$$(4.13)$$

which are again valid for both resonant and nonresonant contributions. Thus knowing the values of $\chi^{NR}_{tot,eff}(sps, R)$ and $\chi^{NR}_{tot,eff}(sps, T)$ listed in Table 4.4, we could solve Eqs. (4.12) and (4.13) and obtain the surface and bulk contributions $\chi^{NR}_{S,eff}(sps)$ and $\chi^{NR}_{B,eff}(sps)$ separately. Their values are also listed in Table 4.4.

Table 4.4: The nonresonant background obtained from fitting of the SFG spectra of OTS in the unit of $10^{-22}\text{m}^2\text{V}^{-1}$.

	Reflection	Transmission
$\chi_{\text{tot,eff}}^{\text{NR}}(ssp)$	-3.4	2.8
$\chi_{\text{tot,eff}}^{\text{NR}}(ppp)$	-2.6	-0.7
$\chi_{\text{tot,eff}}^{\text{NR}}(sps)$	-3.2	10
$\chi_{\text{S,eff}}^{\text{NR}}(sps)$	-2.4	-3
$\chi_{\text{B,eff}}^{\text{NR}}(sps)$	-0.8	13

4.4.2   Polyethylene film

We have also measured the reflected and transmitted SFG in the C-H stretch region from a thin film of polyethylene on a fused silica plate. The molecular structure of polyethylene is shown in the inset of Fig. 4.3. The reflected SFG spectra were reported in an earlier study, and they were found to be dominated by the surface contribution [109]. With transmitted SFG, we can determine the bulk contribution more quantitatively.

The polyethylene sample used in this experiment was prepared on a fused silica substrate using the following technique. A grain of low density polyethylene was sandwiched between fused silica and sodium chloride windows. It was heated until it completely melted. Then it was squeezed between the two windows to form a 100-200 μm thick film. The "sandwich" was then cooled to room temperature and immersed in distilled water. Due to dissolution, the NaCl window was separated from the film, and a smooth polyethylene surface suitable for optical measurements appeared. The film thickness was sufficient to absorb most of the infrared energy to prevent the polymer/silica interface from contributing to SFG. Therefore the SFG signal we measured must have come from the air/polymer interface and the neighboring polymer bulk within the infrared absorption length.

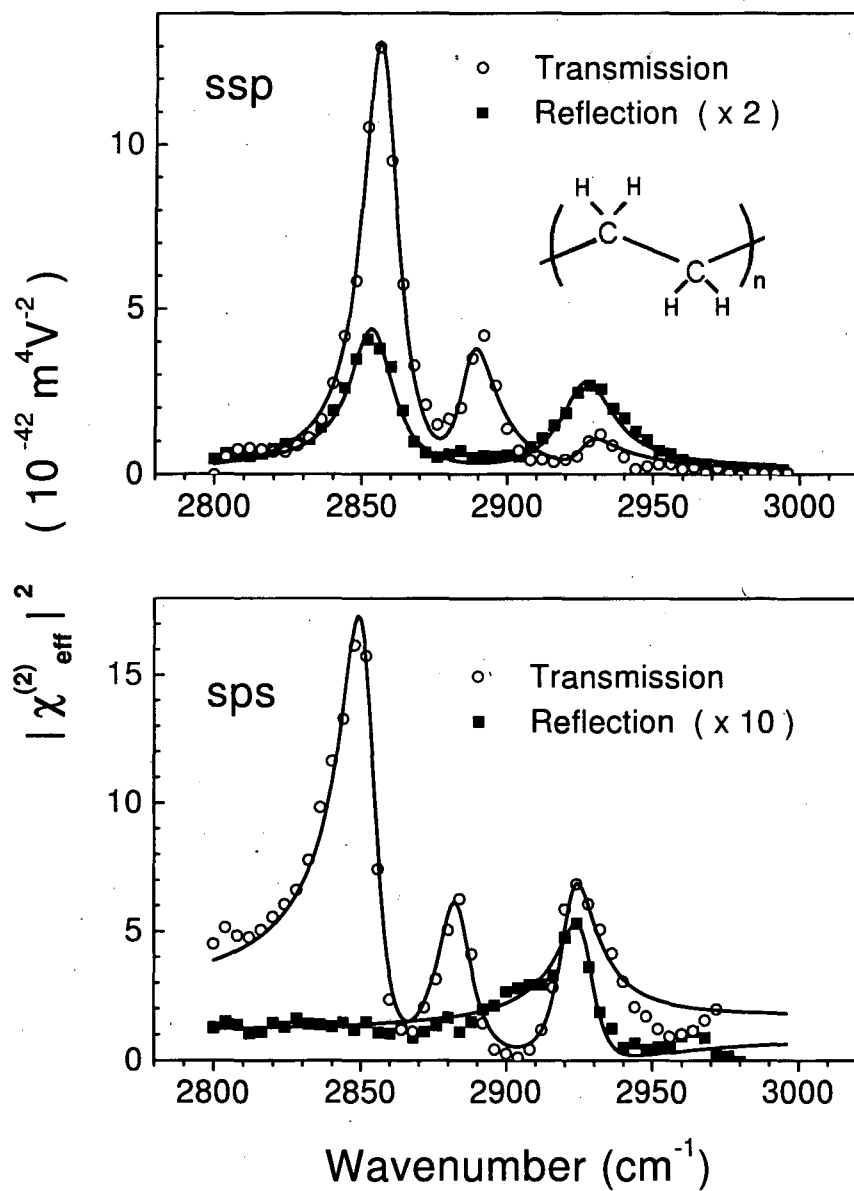Fig. 4.3 displays the SFG spectra of polyethylene for the *ssp* and *sps* polarization

Figure 4.3: SFG spectra of a polyethylene film on fused silica. The solid curves are theoretical fits.

combinations. While the reflection SFG spectra are essentially the same as those published in Ref. [109], the transmission SFG spectra are very different and can be explained only by the existence of the bulk contribution. The spectra show mainly three vibrational modes at $2850 \, \text{cm}^{-1}$, $2884 \, \text{cm}^{-1}$ and $2926 \, \text{cm}^{-1}$. They can be assigned to the symmetric CH_2, Raman-active antisymmetric CH_2 and IR-active antisymmetric CH_2 stretch vibrations, respectively [109, 110, 111]. One remarkable feature is that the Raman-active antisymmetric CH_2 stretch mode appears in the transmitted SFG spectra but not in the reflected SFG spectra. Being Raman-active and infrared-forbidden, this vibrational mode can only be excited by the infrared field via electric-quadrupole excitation and therefore shows up only in the bulk contribution to SFG.

The significantly stronger SFG signal in the transmitted direction is due to a longer coherence length l_c that enhances the bulk contribution through the $\chi_B^{(2)}$ term in Eq. (4.6). From the measured spectra we can obtain a rough estimate of $\chi_B^{(2)}$. Here we consider the CH_2 symmetric stretch mode in the *sps* polarization combination, which appears to be the strongest peak in the transmitted SFG spectrum. Since polyethylene has a refractive index (~ 1.5) very close to that of fused quartz, we can still use Eqs. (4.12) and (4.13) as a good approximation because the Fresnel factors and the coherence length in Eqs. (4.11) and (4.11) are not very sensitive to the refractive index. For example, varying n from 1.45 to 1.60 only changes $L_{yy}(\omega_s, \text{R})$ in Table 4.2 from 0.80 to 0.75 .

From Fig. 4.3 we find that at the peak of the CH_2 symmetric stretch mode,

$$|\chi_{\text{tot,eff}}^{(2)}(sps, \text{T})| \approx 4 \times 10^{-21} \text{m}^2 \text{V}^{-1}$$

$$|\chi_{\text{tot,eff}}^{(2)}(sps, \text{R})| \approx 0$$

By solving Eqs. (4.12) and (4.13), we obtain the effective bulk contribution in the reflection direction

$$|\chi_{B,eff}^{(2)}(sps, R)| \approx 3 \times 10^{-22} m^2 V^{-1}$$

which is one order of magnitude smaller than a typical surface dipole contribution $|\chi_{S,eff}^{(2)}(R)|$ on a vibrational resonance. This indicates that in the reflected SFG from polyethylene, the bulk contribution is indeed negligible.

The above value of $|\chi_{B,eff}^{(2)}(R)|$ suggests that with the reflection geometry the bulk contribution is usually negligible as long as the SFG signal is reasonably strong (i.e., $|\chi_{tot,eff}^{(2)}(R)| \gg 3 \times 10^{-22} m^2 V^{-1}$). This justifies the assumption in many cases that the reflected SFG spectra are dominated by surface contribution and can be used to probe surface structure.

4.4.3   Silica/water interface

The fused silica/water interface has been used to study the nature of hydrogen bonding in water with SFG [42]. By varying the pH value of water, an electric field-induced ordering in the hydrogen bonding network at the interface was observed. The bulk contribution in this study was also neglected. As in the case of polyethylene, we can determine the bulk contribution more quantitatively with the transmitted geometry.

For this experiment, a water cell was constructed with two fused quartz windows (IR grade) with a layer of water in between sealed with a Teflon spacer. The water layer was about 500 μm thick, enough to absorb all the infrared input energy to prevent SFG from the bottom interface. Two samples were used. One has deionized water with a pH value

lower than 7 due to unintentionally dissolved carbon dioxide from air. The other one has a dilute ammonia-water solution with pH $= 11.1$ at room temperature. The SFG spectra shown in Fig. 4.4 were taken in both reflection and transmission geometries.

The spectra obtained with the reflection geometry are similar to those in Ref. [42]. The spectra obtained with the transmission geometry are different due to non-negligible bulk contribution in transmission. As in the case of polyethylene, the difference in the SFG spectra with reflection and transmission geometries allows us to obtain an estimate of $\chi_{B,eff}^{(2)}(ssp)$. For this we calculated the Fresnel factors and the coherence lengths for the two geometries at the infrared frequency $\omega_2/(2\pi c) = 3200$ cm^{-1}, from which we obtained the following equations similar to Eqs. (4.12) and (4.13)

$$
\begin{aligned}
\chi_{tot,eff}^{(2)}(ssp, R) &= \chi_{S,eff}^{(2)}(ssp, R) + \chi_{B,eff}^{(2)}(ssp, R) \\
&= .64\{\chi_{S,yyz}^{(2)}L_{zz}(\omega_2)e_{2z} + 52\text{nm}\left[\chi_{B,yyz}^{(2)}L_{zz}(\omega_2)e_{2z} + \chi_{B,yyx}^{(2)}L_{xx}(\omega_2)e_{2x}\right]\},
\end{aligned}
$$

$$(4.14)$$

$$
\begin{aligned}
\chi_{tot,eff}^{(2)}(ssp, T) &= \chi_{S,eff}^{(2)}(ssp, T) + \chi_{B,eff}^{(2)}(ssp, T) \\
&= .61\{\chi_{S,yyz}^{(2)}L_{zz}(\omega_2)e_{2z} - 905\text{nm}\left[\chi_{B,yyz}^{(2)}L_{zz}(\omega_2)e_{2z} + \chi_{B,yyx}^{(2)}L_{xx}(\omega_2)e_{2x}\right]\}.
\end{aligned}
$$

$$(4.15)$$

From the spectra in Fig. 4.4(a) we find that at 3200 cm^{-1},

$$
|\chi_{tot,eff}^{(2)}(ssp, R)| \approx 1.1 \times 10^{-21}\text{m}^2\text{V}^{-1} ,
$$

$$
|\chi_{tot,eff}^{(2)}(ssp, T)| \approx 2.0 \times 10^{-21}\text{m}^2\text{V}^{-1} .
$$

Solving Eqs. (4.14) and (4.15) with the above measured values of $|\chi_{tot,eff}^{(2)}(ssp, R)|$ and
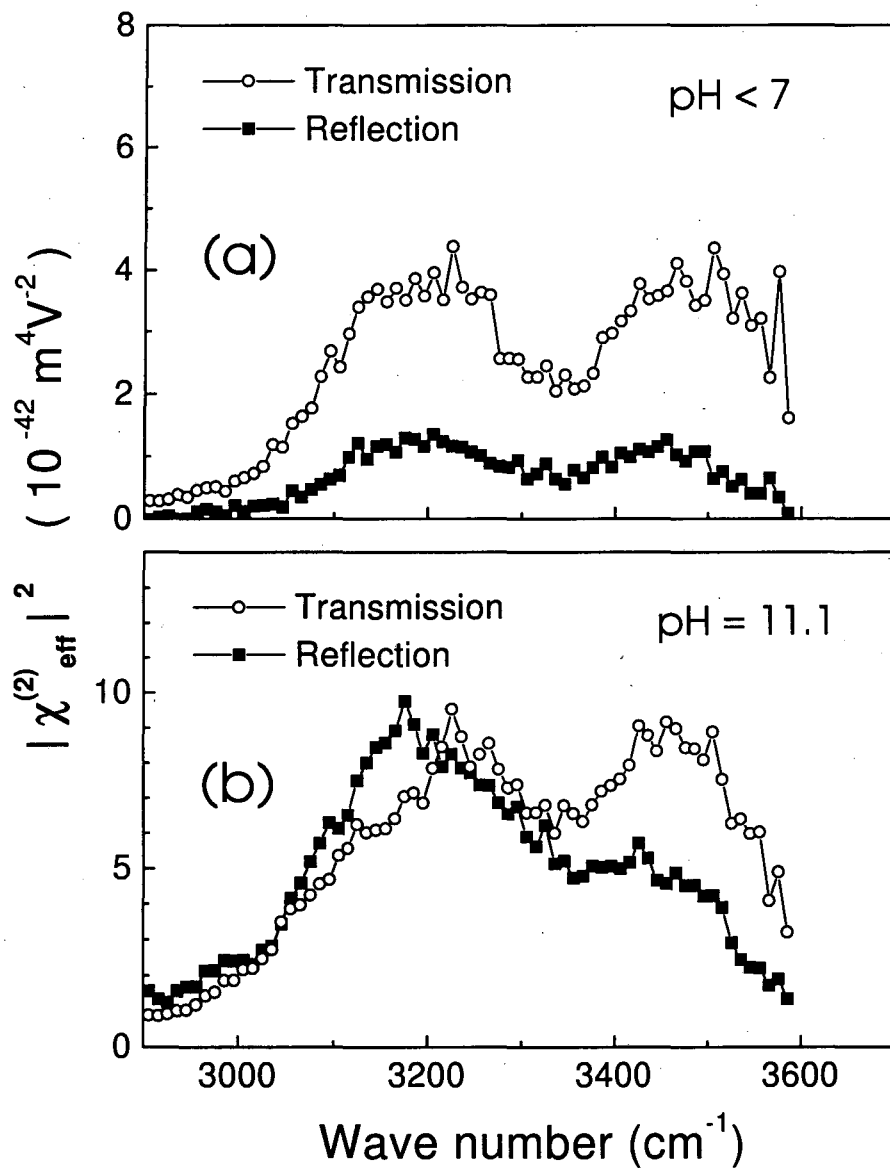
Figure 4.4: SFG spectra of the silica/water interface with reflection and transmission geometries with (a)low pH value due to carbon dioxide dissolved in water and (b)high pH value from intentionally doped ammonia. The polarization combination was ssp, and the temperature was 24°C.

$|\chi^{(2)}_{\text{tot,eff}}(ssp,\text{T})|$ then yields the effective bulk contribution in the reflection direction

$$|\chi^{(2)}_{\text{B,eff}}(ssp,\text{R})| \;=\; (1.1\pm0.6)\times10^{-22}\text{m}^2\text{V}^{-1}\;.$$

In spite of the relatively large error due to the uncertainty of the relative sign between $|\chi^{(2)}_{\text{tot,eff}}(ssp,\text{R})|$ and $|\chi^{(2)}_{\text{tot,eff}}(ssp,\text{T})|$, the above value of $|\chi^{(2)}_{\text{B,eff}}(ssp,\text{R})|$ remains one order of magnitude smaller than the surface contribution $|\chi^{(2)}_{\text{S,eff}}(ssp,\text{R})|$. As in the case of polyethylene, the bulk contribution in the reflection direction for the silica/water interface is also negligible.

4.5 Conclusion

We have developed a scheme to measure both reflected and transmitted SFG spectra from the same sample and used them to estimate the relative contributions of the surface and bulk to SFG. Measurements on an OTS monolayer adsorbed on fused silica showed that the reflected and transmitted spectra originating from the monolayer are well correlated, while the nonresonant background resulting from the bulk contribution of the substrate is significant only in the transmitted spectra. That the bulk contribution is important only for transmitted SFG is also true in the cases of polyethylene and silica/water. Even though the bulk contribution is significant and easily detected in the transmitted SFG, our results suggest that the bulk contribution to the reflected SFG spectra is usually negligible.

Chapter 5

Motional effect in sum-frequency vibrational spectroscopy

5.1 Introduction

Surface vibrational spectroscopy is highly surface-specific and sensitive in media with inversion symmetry. With various input/output polarization combinations, the SFG vibrational spectra can yield detailed information about orientational distributions of selected atomic groups at a surface or interface [9, 55, 60]. In all quantitative SFG studies reported so far, the effects of rotational or librational motion of molecules on their vibrational spectra have been neglected. This, however, may not be a good approximation if the molecules move rapidly. In the latter case, two types of effects can be envisioned. One is the well known motional narrowing effect, which reduces the inhomogeneous linewidth of a vibrational resonance [112]. The other is motional averaging, which may affect the

strength of a vibrational resonance with a given input/output polarization combination. In this chapter we show that the motional averaging effect on SFG spectra can be significant and present an experimental case to demonstrate the effect.

5.2 Theory

Surface SFG results from a second-order nonlinear polarization $\mathbf{P}^{(2)}$ induced at a surface or interface by two input fields $\mathbf{E}_1$ and $\mathbf{E}_2$ at visible and infrared frequencies, respectively. In the time domain, we can write

$$\mathbf{P}^{(2)}(t) \;=\; N_S \langle \mathbf{p}^{(2)}(t) \rangle \;, \tag{5.1}$$

and

$$p_\lambda^{(2)}(t) \;=\; -i\epsilon_0 \sum_q \sum_{\mu\nu} a_{q,\lambda\mu\nu} E_{1\mu}(t) \int_0^{+\infty} E_{2\nu}(t-\tau) e^{-i(\omega_q - i\Gamma_q)\tau} d\tau \;, \tag{5.2}$$

where N_S is the surface density of molecules; the angle brackets denote an ensemble average; $a_{q,\lambda\mu\nu}$, ω_q and Γ_q are the amplitude, resonant frequency and damping constant of the qth molecular vibrational mode, respectively; and the indices λ, μ, ν refer to the molecular coordinates. Here we assume that the visible input is far from resonance. We also neglect inhomogeneous broadening and nonresonant contributions in our discussion. The frequency domain expression of Eq. (5.2) is

$$\tilde{p}_\lambda^{(2)}(\omega_s) = \epsilon_0 \sum_q \sum_{\mu\nu} \int_{-\infty}^{+\infty} d\omega_1 \int_{-\infty}^{+\infty} d\omega_2 \delta(\omega_s - \omega_1 - \omega_2) \frac{a_{q,\lambda\mu\nu}}{\omega_2 - \omega_q + i\Gamma_q} \tilde{E}_{1\mu}(\omega_1) \tilde{E}_{2\nu}(\omega_2) \;,$$

$$\tag{5.3}$$

where $\tilde{p}_\lambda^{(2)}(\omega_s)$, $\tilde{E}_{1\mu}(\omega_1)$, and $\tilde{E}_{2\nu}(\omega_2)$ are the Fourier integrals of $p_\lambda^{(2)}(t)$, $E_{1\mu}(t)$, and $E_{2\nu}(t)$, respectively. For example,

$$\tilde{p}_\lambda^{(2)}(\omega_s) = \frac{1}{2\pi} \int\limits_{-\infty}^{+\infty} p_\lambda^{(2)}(t)e^{i\omega_s t}dt . \tag{5.4}$$

For simplicity, in Eq. (5.2) we have dropped the complex conjugate term, which, when added, would contribute to Eq. (5.3) an extra term $-\frac{a_{q,\lambda\mu\nu}}{\omega_2 + \omega_q + i\Gamma_q}$. However, it has no significant effect on our results.

Transformed into the lab coordinates i, j, k, Eq. (5.2) becomes

$$p_i^{(2)}(t) = -i\epsilon_0 \sum_q \sum_{jk} \sum_{\lambda\mu\nu} a_{q,\lambda\mu\nu} E_{1j}(t) D_{i\lambda}(t) D_{j\mu}(t) \int\limits_0^{+\infty} D_{k\nu}(t-\tau)E_{2k}(t-\tau)e^{-i(\omega_q - i\Gamma_q)\tau}d\tau . \tag{5.5}$$

Here $D_{l\xi}(t) = \hat{l} \cdot \hat{\xi}(t)$ is a time-dependent direction cosine matrix with $l = i, j, k$ and $\xi = \lambda, \mu, \nu$, assuming that the molecular orientation varies with time. Fourier transformation into the frequency domain gives

$$\begin{aligned}
\tilde{p}_i^{(2)}(\omega_s) &= \frac{\epsilon_0}{2\pi} \sum_q \sum_{jk} \sum_{\lambda\mu\nu} \int\limits_{-\infty}^{+\infty} dt \int\limits_{-\infty}^{+\infty} d\omega_1 \int\limits_{-\infty}^{+\infty} d\omega_2 \, a_{q,\lambda\mu\nu} \\
&\quad \Theta_{q,ijk}^{\lambda\mu\nu}(\omega_2, t)\tilde{E}_{1j}(\omega_1)\tilde{E}_{2k}(\omega_2)e^{i(\omega_s - \omega_1 - \omega_2)t} ,
\end{aligned} \tag{5.6}$$

where

$$\Theta_{q,ijk}^{\lambda\mu\nu}(\omega_2, t) = -iD_{i\lambda}(t)D_{j\mu}(t) \int\limits_0^{+\infty} D_{k\nu}(t-\tau)e^{i(\omega_2 - \omega_q + i\Gamma_q)\tau}d\tau . \tag{5.7}$$

Then, with Eqs. (5.6) and (5.7) and the relation

$$\begin{aligned}
\tilde{P}_i^{(2)}(\omega_s) &= N_S \langle \tilde{p}_i^{(2)}(\omega_s) \rangle \\
&= \epsilon_0 \sum_{jk} \int\limits_{-\infty}^{+\infty} d\omega_1 \int\limits_{-\infty}^{+\infty} d\omega_2 \delta(\omega_s - \omega_1 - \omega_2)\chi_{ijk}^{(2)}(\omega_2)\tilde{E}_{1j}(\omega_1)\tilde{E}_{2k}(\omega_2)
\end{aligned} \tag{5.8}$$

defining the surface nonlinear susceptibility $\chi^{(2)}_{ijk}(\omega_2)$, we find

$$\chi^{(2)}_{ijk}(\omega_2) = N_S \sum_q \sum_{\lambda\mu\nu} a_{q,\lambda\mu\nu} \langle \Theta^{\lambda\mu\nu}_{q,ijk}(\omega_2)\rangle \; . \tag{5.9}$$

Being an ensemble average, $\langle\Theta^{\lambda\mu\nu}_{q,ijk}(\omega_2)\rangle$ in Eq. (5.9) is time-independent.

If the molecular orientations are fixed in time, then

$$\Theta^{\lambda\mu\nu}_{q,ijk}(\omega_2) = \frac{1}{\omega_2 - \omega_{\hat q} + i\Gamma_q} D_{i\lambda}D_{j\mu}D_{k\nu} \; , \tag{5.10}$$

which leads to

$$\chi^{(2)}_{ijk}(\omega_2) = N_S \sum_q \sum_{\lambda\mu\nu} \frac{a_{q,\lambda\mu\nu}}{\omega_2 - \omega_q + i\Gamma_q} \langle D_{i\lambda}D_{j\mu}D_{k\nu}\rangle \; . \tag{5.11}$$

Equation (5.11) is the expression that has been commonly used for the analysis [9, 55, 60, 113] and simulation [46] of SFG vibrational spectra. As the derivation shows, however, Eq. (5.11) is not necessarily correct if $D_{l\xi}(t)$ varies in time. It is still a good approximation, though, if $D_{l\xi}(t)$ varies much more slowly than the vibrational relaxation time $1/\Gamma_q$ (the slow-motion limit). In the other extreme, however, if the molecular orientation fluctuates very rapidly around the average orientation within the time scale $1/\Gamma_q$ (the rapid-motion limit), with

$$-i\int_0^{+\infty} D_{k\nu}(t-\tau)e^{i(\omega_2-\omega_q+i\Gamma_q)\tau}d\tau \approx \frac{1}{\omega_2 - \omega_q + i\Gamma_q}\langle D_{k\nu}(t)\rangle \tag{5.12}$$

and the equivalence of temporal and ensemble averages, we find

$$\langle\Theta^{\lambda\mu\nu}_{q,ijk}(\omega_2)\rangle \approx \frac{1}{\omega_2 - \omega_q + i\Gamma_q}\langle D_{i\lambda}D_{j\mu}\rangle\langle D_{k\nu}\rangle \; , \tag{5.13}$$

116

and

$$\chi_{ijk}^{(2)}(\omega_2) \approx N_S \sum_q \sum_{\lambda\mu\nu} \frac{a_{q,\lambda\mu\nu}}{\omega_2 - \omega_q + i\Gamma_q} \langle D_{i\lambda} D_{j\mu} \rangle \langle D_{k\nu} \rangle .$$

(5.14)

This is obviously different from Eq. (5.11). For the intermediate case between the two limits, we must refer to the more general expression for $\chi_{ijk}^{(2)}(\omega_2)$ [Eq. (5.9)].

The orientational fluctuations of molecules of liquids may occur on a subpicosecond time scale [114, 115, 116] and therefore could have an observable effect on the SFG surface vibrational spectra. We take the free (or dangling) OH bonds at the vapor/water interface as an example. The free OH stretch mode appears as a sharp peak at $\sim$3700 cm^{-1} in the SFG spectra [41]. To see how the SFG spectra can be affected by the OH orientational fluctuation, which may occur rapidly over a large solid angle, we calculate the resonant mode amplitudes for different polarization combinations in both slow- and rapid-motion limits. As seen from Eqs. (5.11) and (5.14), the mode amplitudes are given by

$$A_{q,ijk} = N_S \sum_{\lambda\mu\nu} a_{q,\lambda\mu\nu} \langle D_{i\lambda} D_{j\mu} D_{k\nu} \rangle$$

(5.15)

for the slow-motion limit, and

$$A_{q,ijk} = N_S \sum_{\lambda\mu\nu} a_{q,\lambda\mu\nu} \langle D_{i\lambda} D_{j\mu} \rangle \langle D_{k\nu} \rangle$$

(5.16)

for the rapid-motion limit. As in Chap. 2, we assume the only nonvanishing elements of $a_{q,\lambda\mu\nu}$ for a free OH bond are $a_{\zeta\zeta\zeta}$ and $a_{\xi\xi\zeta} = a_{\eta\eta\zeta}$, where $\hat{\zeta}$ is along the OH bond direction and $\hat{\xi}$ and $\hat{\eta}$ are perpendicular to $\hat{\zeta}$. From Raman measurements it was found that $a_{\xi\xi\zeta} = 0.32 a_{\zeta\zeta\zeta}$ [41, 48]. To calculate the ensemble averages, we assume for the free OH

bonds at the interface a step function orientational distribution

$$f(\theta) = \text{constant} \quad \text{for } 0 \leq \theta \leq \theta_M \;,$$

$$f(\theta) = 0 \qquad\qquad \text{for } \theta > \theta_M \;.$$

in the bond tilt angle θ from the surface normal $\hat{z}$ (the azimuthal distribution is isotropic). We could also assume $f(\theta)$ to take other forms (e.g., a Gaussian distribution) without changing our general conclusion.

The SFG output from a surface is proportional to the square of the effective surface nonlinear susceptibility [9]

$$\chi_{\text{eff}}^{(2)}(\omega_2) = \sum_q \frac{A_{q,\text{eff}}}{\omega_2 - \omega_q + i\Gamma_q} \;, \tag{5.17}$$

with

$$A_{q,\text{eff}} = [\mathbf{L}(\omega_s) \cdot \hat{\mathbf{e}}_s] \cdot \mathbf{A}_q : [\mathbf{L}(\omega_1) \cdot \hat{\mathbf{e}}_1][\mathbf{L}(\omega_2) \cdot \hat{\mathbf{e}}_2] \;, \tag{5.18}$$

where $\hat{\mathbf{e}}_i$ is the unit polarization vector of the field at ω_i and $\mathbf{L}(\omega_i)$ is the tensorial Fresnel factor (Appendix B). The values of the Fresnel factors are listed in Table 5.1. The dielectric constant of the surface monolayer $\epsilon'(\omega_i)$ in Table 5.1 is an unknown parameter. The physical implication of ϵ' is discussed in Appendix C. For the vapor/water interface, we used $\epsilon'(\omega_s) = \epsilon'(\omega_1) = 1.31$ deduced from our SFG measurement of the vapor/ice interface (Chap. 2), which agrees very well with the estimate Eq. (C.6) obtained from the model presented in the appendix of Ref. [55]. With the same model, we obtained $\epsilon'(\omega_2) \approx 1.2$ from $\epsilon(\omega_2) \approx 1.4$ for bulk water at 3700 cm^{-1} [117]. We can then use Eq. (5.18) to calculate $A_{q,\text{eff}}(\hat{\mathbf{e}}_s, \hat{\mathbf{e}}_1, \hat{\mathbf{e}}_2)$ and compare with experimentally deduced values.

Table 5.1: Calculated Fresnel factors for the vapor/water interface. z is along the sample surface normal, with the xz plane being the light incidence plane. β is the incidence angle of the input or output beam. ϵ' is the effective dielectric constant of the surface monolayer.

	ω_s	ω_1	ω_2
λ	444 nm	532 nm	2.7 μm
n	1.34	1.34	1.18
β	46.8°	45°	57°
L_{xx}	.95	.95	1.04
L_{yy}	.76	.77	.79
L_{zz}	$1.05/\epsilon'_s$	$1.05/\epsilon'_1$	$.96/\epsilon'_2$
$e_x L_{xx}$ (p)	-.66	.67	.57
$e_y L_{yy}$ (s)	.76	.77	.79
$e_z L_{zz}$ (p)	$.76/\epsilon'_s$	$.75/\epsilon'_1$	$.80/\epsilon'_2$

We have calculated $A_{q,\mathrm{eff}}$ for three different polarization combinations ssp (denoting s-, s-, and p-polarized sum-frequency output, visible input, and infrared input, respectively), ppp, and sps in both slow- and rapid-motion limits. The results as functions of θ_M are presented in Fig. 5.1. For ssp and ppp, the difference between the two limits is appreciable only at large θ_M, which is understandable because the motional effect is important only if the motion covers a very broad range. For $A_{q,\mathrm{eff}}(sps)$, it vanishes in the rapid-motion limit for all θ_M because, from Eqs. (5.16) and (5.18), $A_{q,\mathrm{eff}}(sps) \propto A_{q,yzy} \propto \langle \hat{y} \cdot \hat{\zeta} \rangle = 0$, since $\langle \hat{\zeta} \rangle$ is along the surface normal $\hat{z}$. On the other hand, in the slow-motion limit, $A_{q,\mathrm{eff}}(sps)$ contains terms proportional to $\langle (\hat{y} \cdot \hat{\zeta})(\hat{z} \cdot \hat{\zeta})(\hat{y} \cdot \hat{\zeta}) \rangle$ and $\langle (\hat{y} \cdot \hat{\eta})(\hat{z} \cdot \hat{\eta})(\hat{y} \cdot \hat{\zeta}) \rangle$ that do not vanish for finite θ_M.

5.3 Experiment

We have obtained experimentally the SFG spectra from the vapor/water interface with the polarization combinations specified above. The experimental setup has been de-
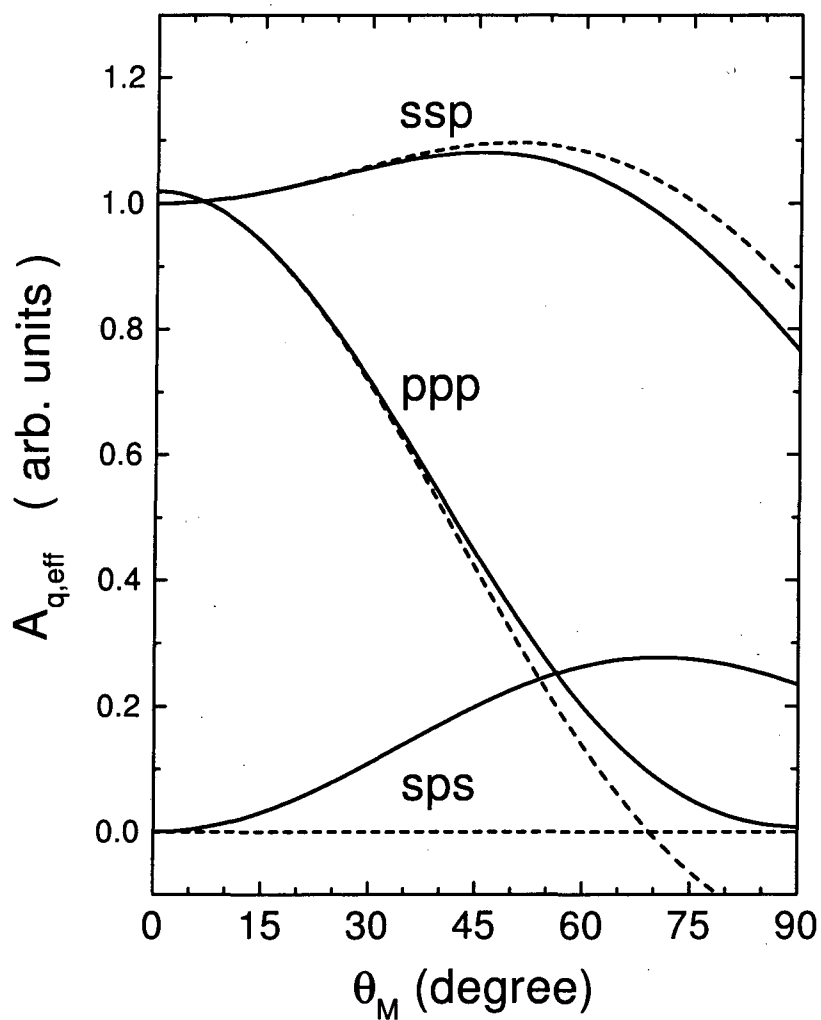
Figure 5.1: Theoretical prediction of the mode amplitudes $A_{q,\text{eff}}$ for the free OH bonds on the water surface. The solid lines are calculated for the slow-motion limit, and the dashed lines are for the rapid-motion limit. All values are normalized with respect to $A_{q,\text{eff}}(ssp)$ at $\theta_M = 0$.

Table 5.2: Parameters used to fit the *ssp* SFG spectrum of the vapor/water interface. The non-resonant background was $\chi^{(2)}_{NR,eff}(ssp) = 1.2 \times 10^{-22}$ m^{2}V^{-1}.

Mode	$\omega_q/(2\pi c)$	$\Gamma_q/(2\pi c)$	$A_{q,eff}(ssp)$
Bonded OH	3008 cm^{-1}	108 cm^{-1}	-2.7$\times10^{-9}$ m^{2}V^{-1}sec^{-1}
Bonded OH	3171 cm^{-1}	118 cm^{-1}	-9.6$\times10^{-9}$ m^{2}V^{-1}sec^{-1}
Bonded OH	3414 cm^{-1}	111 cm^{-1}	10.5$\times10^{-9}$ m^{2}V^{-1}sec^{-1}
Free OH	3698 cm^{-1}	14.5 cm^{-1}	1.70$\times10^{-9}$ m^{2}V^{-1}sec^{-1}

scribed in Sec. 1.2. The measured spectra are depicted in Fig. 5.2. The SFG intensities have been calibrated with a reference z-cut quartz crystal (Sec. 1.3.2), yielding the spectra of $|\chi^{(2)}_{eff}(\omega_2)|^2$ in MKS units. The solid curves are fits using Eq. (5.17) with the addition of a nonresonant contribution to $\chi^{(2)}_{eff}$. The fitting parameters used here to fit the *ssp* spectrum are presented in Table 5.2. They are somewhat different from those in Ref. [41]. The two broad peaks at ~ 3200 cm^{-1} and ~ 3400 cm^{-1} in the *ssp* spectrum have been assigned to the more ordered and less ordered hydrogen-bonded OH stretch modes, respectively [42]. The resonant feature at $3500 - 3600$ cm^{-1} in the *ppp* and *sps* polarization combinations, which has not been reported before for the vapor/water interface, is presumably associated with OH bonds that are only weakly perturbed by hydrogen-bonding to neighbors. Here, our focus is on the free OH bonds only.

The free OH stretch mode appears at $\omega_q/(2\pi c) = 3698$ cm^{-1}, with $\Gamma_q/(2\pi c) = 14.5$ cm^{-1} (including the finite infrared linewidth) and the following mode amplitudes

$$A_{q,eff}(ssp) = 1.70 \pm 0.15 \times 10^{-9} \text{ m}^2\text{V}^{-1}\text{sec}^{-1} ,$$

$$A_{q,eff}(ppp) = 4.8 \pm 0.5 \times 10^{-10} \text{ m}^2\text{V}^{-1}\text{sec}^{-1} ,$$

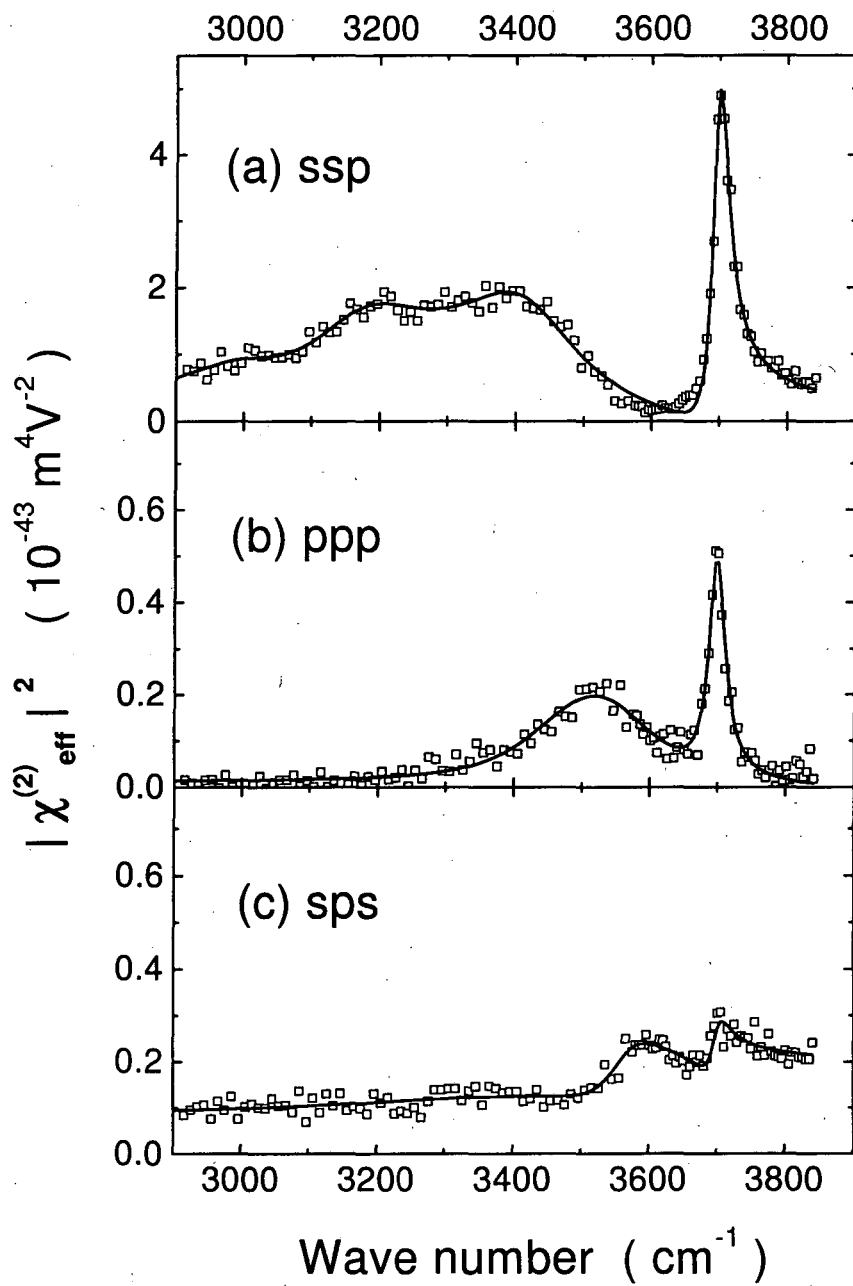$$A_{q,eff}(sps) = 9 \pm 3 \times 10^{-11} \text{ m}^2\text{V}^{-1}\text{sec}^{-1} .$$

Figure 5.2: Free OH SFG spectra of the water surface at 20°C with three different polarization combinations *ssp*, *ppp*, and *sps*.

To compare the theory with experiment, we notice that from the experiment,

$$A_{q,\text{eff}}(ssp) : A_{q,\text{eff}}(ppp) : A_{q,\text{eff}}(sps)$$

$$= \quad 1 \; : \; 0.28 \pm 0.04 \; : \; 0.05 \pm 0.02 \; .$$

This does not agree with the ratio for any value of θ_M obtained from the set of curves for the slow-motion limit in Fig. 5.1. In other words, with the motional effect neglected, we cannot find a reasonable orientational distribution for the free OH bonds to explain the experimental results. The very small value of $A_{q,\text{eff}}(sps)$ in comparison with $A_{q,\text{eff}}(ssp)$ and $A_{q,\text{eff}}(ppp)$ indicates that the motional effect is significant and that the rapid-motion limit is actually a better approximation. The theoretical curves for the rapid-motion limit in Fig. 5.1 predict that an orientational distribution with $\theta_\text{M} = 51°$ should yield a ratio $A_{q,\text{eff}}(ssp) : A_{q,\text{eff}}(ppp) : A_{q,\text{eff}}(sps) = 1 : 0.28 : 0$, which matches the experimental ratio better than the theoretical prediction based on the slow-motion limit.

We note that the theoretical result described here does not depend critically on the assumptions made for $a_{q,\lambda\mu\nu}$, ϵ', and $f(\theta)$. The motional effect is largely manifested by the unexpectedly weak mode strength in the *sps* SFG spectrum. This has been observed on other liquid surfaces as well. For example, the absence of the N-H stretch mode in the *sps* SFG spectrum of the surface of an ammonia-water solution [60] could also be the result of motional averaging. On the other hand, for larger molecules with slow orientational fluctuations, we can observe reasonably large values of $A_{q,\text{eff}}(sps)$. One such example is the C-N stretch mode of pentyl-cyanoterphenyl (5CT) molecules on water, from which a ratio $\frac{A_{q,\text{eff}}(sps)}{A_{q,\text{eff}}(ssp)} \approx 0.4$ has been reported [55].

5.4 Conclusion

In summary, we have considered here an effect from the rotation or libration of molecules on surface sum-frequency vibrational spectroscopy. The free OH stretch mode at the vapor/water interface is used as an example to illustrate the significance of the effect. Difficulty in the interpretation of the SFG spectra would arise if the effect is neglected. In general, the effect of motional averaging should also be observable in infrared and Raman spectroscopy.

124

Bibliography

[1] X. D. Zhu, H. Suhr, and Y. R. Shen, Phys. Rev. B **35**, 3047 (1987).

[2] Y. R. Shen, "Surface spectroscopy by nonlinear optics", in *Frontiers in Laser Spectroscopy*, Proceedings of the International School of Physics "Enrico Fermi", Course CXX, T. W. Hänsch and M. Inguscio, eds., (North Holland, Amsterdam, 1994), p.139.

[3] D. Kim, Ph.D. thesis, University of California (1997), Chap. 3.

[4] T. F. Heinz, Ph.D. thesis, University of California (1982), Appendix 3.

[5] S. Singh, "Nonlinear optical materials", in *Handbook of Lasers*, R. J. Pressley, ed., (Chemical Rubber Co., Cleveland, Ohio, 1971) p.489 and p.497.

[6] Y. R. Shen, *The Principles of Nonlinear Optics* (John Wiley & Sons, Inc., New York, 1984) p.73-76.

[7] X. Wei, P. B. Miranda, and Y. R. Shen, Phys. Rev. Lett., accepted.

[8] X. Wei, X. Zhuang, S.-C. Hong, T. Goto, and Y. R. Shen, Phys. Rev. Lett. **82**, 4256 (1999).

[9] X. Wei, S.-C. Hong, X. Zhuang, T. Goto, and Y. R. Shen, Phys. Rev. E **62**, 5160 (2000).

[10] X. Wei, S.-C. Hong, A. I. Lvovsky, H. Held, and Y. R. Shen, J. Phys. Chem. B **104**, 3349 (2000).

[11] X. Wei and Y. R. Shen, to be published.

[12] M. Faraday, Lecture before the Royal Institution reported in the Athenaeum no.**1181**, 640 (1850); M. Faraday, Philos. Mag. **17**, 162 (1859); M. Faraday, Proc. Roy. Soc., London **10**, 440 (1860).

[13] J. W. M. Frenken and J. F. van der Veen, Phys. Rev. Lett. **54**, 134 (1985); J. W. M. Frenken, P. M. J. Maree, and J. F. van der Veen, Phys. Rev. B **34**, 7506 (1986).

[14] K. C. Prince, U. Breuer, and H. P. Bonzel, Phys. Rev. Lett. **60**, 1146 (1988).

[15] D.-M. Zhu and J. G. Dash, Phys. Rev. Lett. **57**, 2959 (1986).

[16] E. G. McRae and R. A. Malic, Phys. Rev. Lett. **58**, 1437 (1987).

[17] R. Trittibach, Ch. Grütter, and J. H. Bilgram, Phys. Rev. B **50**, 2529 (1994).

[18] M. Polčik, L. Wilde, and J. Haase, Phys. Rev. Lett. **78**, 491 (1997).

[19] J. G. Dash, H. Fu, and J. S. Wettlaufer, Rep. Prog. Phys. **58**, 115 (1995).

[20] J. S. Wettlaufer and J. G. Dash, Scientific American, **282**, 34 (2000).

[21] N. H. Fletcher, Philos. Mag. **18**, 1287 (1968).

[22] J. S. Wettlaufer, Phys. Rev. Lett. **82**, 2516 (1999); and references therein.

[23] G.-J. Kroes, Surface Science **275**, 365 (1992).

[24] Y. Furukawa and H. Nada, J. Phys. Chem. B **101**, 6167 (1997).

[25] K. Bolton and J. B. C. Pettersson, J. Phys. Chem. B **104**, 1590 (2000).

[26] D. Nason and N. H. Fletcher, J. Chem. Phys. **62**, 4444 (1975).

[27] I. Golecki and C. Jaccard, J. Phys. C **11**, 4229 (1978).

[28] D. Beaglehole and D. Nason, Surf. Sci. **96**, 357-65 (1980).

[29] Y. Furukawa, M. Yamamoto, and T. Kuroda, J. Cryst. Growth **82**, 655 (1987).

[30] M. Elbaum, S. G. Lipson, and J. G. Dash, J. Cryst. Growth **129**, 491-505 (1993).

[31] J. Ocampo and J. Klinger, J. Phys. Chem. **87**, 4325 (1983)

[32] Y. Mizuno and N. Hanafusa, J. Phys. Colloq. C1 **48**, 511 (1987)

[33] N. Materer, U. Starke, A. Barbieri, M. A. Van Hove, G. A. Somorjai, G.-J. Kroes, and C. Minot, J. Phys. Chem. **99**, 6267 (1995).

[34] H. Dosch, A. Lied, and J. H. Bilgram, Surf. Sci. **327**, 145-164 (1995); A. Lied, H. Dosch, and J. H. Bilgram, Phys. Rev. Lett. **72**, 3554 (1994).

[35] J. Braun, A. Glebov, A. P. Graham, A. Menzel, and J. P. Toennies, Phys. Rev. Lett. **80**, 2638 (1998).

[36] A. Döppenschmidt and H. J. Butt, Langmuir **16**, 6709 (2000).

[37] B. Pittinger, D. J. Cook, C. R. Slaughterbeck, and S. C. Fain, J. Vac. Sci. Technol. A **16**, 1832 (1998).

[38] R. R. Gilpin, J. Colloid Interface Sci. **77**, 435 (1980).

[39] M. Maruyama, M. Bienfait, J. G. Dash, and G. Coddens, J. Cryst. Growth **118**, 33 (1992).

[40] S. S. Barer, N. V. Churaev, B. V. Derjaguin, O. A. Kiseleva, and V. D. Sobolev, J. Colloid Interface Sci. **74**, 173 (1980).

[41] Q. Du, R. Superfine, E. Freysz, and Y. R. Shen, Phys. Rev. Lett. **70**, 2313 (1993).

[42] Q. Du, E. Freysz, and Y. R. Shen, Phys. Rev. Lett. **72**, 238 (1994).

[43] Q. Du, E. Freysz, and Y. R. Shen, Science **264**, 826 (1994).

[44] X. Su, L. Lianos, Y. R. Shen, and G. A. Somorjai, Phys. Rev. Lett. **80**, 1533 (1998).

[45] R. Superfine, J. Y. Huang, and Y. R. Shen, Chem. Phys. Lett. **172**, 303 (1990).

[46] A. Morita and J. T. Hynes, Chem. Phys. **258**, 371 (2000).

[47] S. A. Clough, Y. Beers, G. P. Klein, and L. S. Rothman, J. Chem. Phys. **59**, 2254 (1973).

[48] W. F. Murphy, Mol. Phys. **36**, 727 (1978).

[49] F. M. Geiger, A. C. Tridico, and J. M. Hicks, J. Phys. Chem. B **103**, 8205 (1999).

[50] T. F. Heinz, M. M. T. Loy, and W. A. Thompson, Phys. Rev. Lett. **54**, 63 (1985).

[51] R. A. Brown, J. Kelzer, U. Stelger, and Y. Yeh, J. Phys. Chem. **87**, 4135 (1983)

[52] J. Sagiv, J. Am. Chem. Soc. **102** 92 (1980).

128

[53] J. R. Scherer and R. G. Snyder, J. Chem. Phys. **67**, 4794 (1977).

[54] P. T. T. Wong and E. Whalley, J. Chem. Phys. **62**, 2418 (1975).

[55] X. Zhuang, P. B. Miranda, D. Kim, and Y. R. Shen, Phys. Rev. **B59**, 12632 (1999).

[56] I. Engquist and B. Liedberg, J. Phys. Chem. **100**, 20089 (1996).

[57] R. K. Iler, *The Chemistry of Silica* (Wiley, New York, 1979) p.622-729.

[58] K. Wolfrum, J. Löbau, and A. Laubereau, Appl. Phys. A **59**, 605 (1994).

[59] Y. R. Shen, Solid State Communications **108**, 399 (1998).

[60] D. Simonelli and M. J. Shultz, J. Chem. Phys. **112**, 6804 (2000).

[61] J. D. Bernal and R. H. Fowler, J. Chem. Phys. **1**, 515 (1933).

[62] P. V. Hobbs, *Ice Physics*, (Oxford University Press, New York, 1974) Chap. 2.

[63] V. F. Petrenko and R. W. Whitworth, *Physics of Ice*, (Oxford University Press, New York, 1999) Chap. 4.

[64] M. C. Desjonquères and D. Spanjaard, *Concepts in Surface Physics*, 2nd edition (Springer, New York, 1996) p.15-43.

[65] M. Elbaum, Phys. Rev. Lett. **67**, 2982 (1991).

[66] S. Kawada and R. Tutiya, J. Phys. Chem. Solids **58**, 115 (1997).

[67] C. Mauguin, Bull. Soc. Fr. Miner. **34**, 71 (1911).

[68] B. Bahadur, ed., *Liquid Crystals Applications and Uses* (World Scientific, Singapore, 1990).

[69] D. W. Berreman, Phys. Rev. Lett. **28**, 1683 (1972); Mol. Cryst. Liq. Cryst. **23**, 215 (1973).

[70] J. M. Geary, J. W. Goodby, A. R. Kmetz, and J. S. Patel, J. Appl. Phys. **62**, 4100 (1987).

[71] W. Chen, M. B. Feller, and Y. R. Shen, Phys. Lett. **63**, 2665 (1989).

[72] M. B. Feller, W. Chen, and Y. R. Shen, Phys. Rev. A **43**, 6778 (1991).

[73] M. Barmentlo, R. W. J. Hollering, and N. A. J. M. van Aerle, Phys. Rev. A **46**, R4490 (1992).

[74] X. Zhuang, L. Marrucci, and Y. R. Shen, Phys. Rev. Lett. **73**, 1513 (1994).

[75] R. Meister and B. Jérôme, Macromolecules **32**, 480 (1999).

[76] Y. M. Zhu, L. Wang, Z. H. Lu, Y. Wei, X. X. Chen, and J. H. Tang, Appl. Phys. Lett. **65**, 49 (1994).

[77] Y. B. Kim, H. Olin, S. Y. Park, J. W. Choi, L. Komitov, M. Matuszczyk, and S. T. Lagerwall, Appl. Phys. Lett. **66**, 2218 (1995).

[78] A. J. Pidduck, G. P. Bryan-Brown, S. Haslam, R. Bannister, and I. Kitely, J. Vac. Sci. Tech. A **14**, 1723 (1996).

[79] I. Hirosawa, Jap. J. Appl. Phys. Part1 **35**, 5873 (1996).

130

[80] K. Sakamoto, R. Arafune, N. Ito, S. Ushioda, Y. Suzuki, and S. Morokawa, Jap. J. Appl. Phys. **33**, L1323 (1994); K. Sakamoto, R. Arafune, N. Ito, and S. Ushioda, J. Appl. Phys. **80**, 431 (1996).

[81] R. Hasegawa, Y. Mori, H. Sasaki and M. Ishibashi, Jap. J. Appl. Phys. **35**, 3492 (1996).

[82] R. Arafune, K. Sakamoto, and S. Ushioda, Appl. Phys. Lett. **71**, 2755 (1997).

[83] G. D. Hietpas, J. M. Sands, and D. L. Allara, J. Phys. Chem. B **102**, 10556 (1998).

[84] M. F. Tony, T. P. Russell, J. A. Logan, H. Kikuchi, J. M. Sands, and S. K. Kumar, Nature **374**, 709 (1995)

[85] I. Hirosawa, N. Sasaki, and H. Kimura, Jap. J. Appl. Phys. Part2 **38**, L583 (1999).

[86] M. G. Samant, J. Stöhr, H. R. Brown, T. P. Russell, J. M. Sands, and S. K. Kumar, Macromolecules **29**, 8334 (1996).

[87] K. Weiss, C. Wöll, E. Böhm, B. Fiebranz, G. Forstmann, B. Peng, V. Scheumann, and D. Johannsmann, Macromolecules **31**, 1930 (1998).

[88] J. Stöhr, M. G. Samant, A. Cossy-Favre, J. Diaz, Y. Momoi, S. Odahara, and T. Nagata, Macromolecules **31**, 1942 (1998).

[89] A. Cossy-Favre, J. Diaz, Y. Liu, H. R. Brown, M. G. Samant, J. Stöhr, A. J. Hanna, S. Anders, and T. P. Russell, Macromolecules **31**, 4957 (1998).

[90] M. Oh-e, A. I. Lvovsky, X. Wei, and Y. R. Shen, J. Chem. Phys. **113**, 8827 (2000).

[91] C. Hirose, N. Akamatsu, and K. Domen, J. Chem. Phys. **96**, 997 (1992); C. Hirose, H. Yamamoto, N. Akamatsu, and K. Domen, J. Phys. Chem. **97**, 10064 (1993).

[92] R. G. Snyder, J. Chem. Phys. **42**, 1744 (1965).

[93] K. B. Wiberg and J. J. Wendolosky, J. Phys. Chem. **88**, 586 (1984).

[94] K. M. Gough, J. Chem. Phys. **91**, 2424 (1989).

[95] S. Krimm, C. Y. Liang, and G. B. B. M. Sutherland, J. Polymer Sci. **22**, 227 (1956).

[96] P. Guyot-Sionnest, R. Superfine, J. H. Hunt, and Y. R. Shen, Chem. Phys. Lett. **144**, 1 (1988).

[97] C. S. Marvel and C. E. Denoon, J. Am. Chem. Soc. **60**, 1045 (1938)

[98] D. Zhang, R. S. Ward, Y. R. Shen, and G. A. Somorjai, J. Phys. Chem. B **101**, 9060 (1997).

[99] C. S. Mullin, P. Guyot-Sionnest, and Y. R. Shen, Phys. Rev. A **39**, 3745 (1989).

[100] A. I. Kitaigorodskii, *Organic Chemical Crystallography* (Consultants Bureau, New York, 1961) p.322-323.

[101] X. Zhuang, D. Wilk, L. Marrucci, and Y. R. Shen, Phys. Rev. Lett. **75**, 2144 (1995).

[102] S. Kobayashi, and Y. Iimura, Proc. SPIE **2175**, 122 (1994); D.-S. Seo, K. Araya, N. Yoshida, M. Nishikawa, Y. Yabe, and S. Kobayashi, Jpn. J. Appl. Phys. **34**, L503 (1995).

[103] Y. R. Shen, Appl. Phys. B: Laser Opt. **68**, 295 (1999).

[104] J. E. Sipe, V. Mizrahi, and G. I. Stegeman, Phys. Rev. B **35**, 9091 (1987).

[105] P. Guyot-Sionnest and Y. R. Shen, Phys. Rev. B **38**, 7985 (1988).

132

[106] R. Superfine, J. Y. Huang, and Y. R. Shen, Phys. Rev. Lett. **66**, 1066 (1991).

[107] P. S. Pershan, Phys. Rev. **130**, 919 (1963).

[108] See, for example, Y. R. Shen, *The Principles of Nonlinear Optics* (John Wiley & Sons, Inc., New York, 1984) Chap.25.

[109] D. Zhang, Y. R. Shen, and G. A. Somorjai, Chem. Phys. Lett. **281**, 394 (1997).

[110] D. O. Hummel, *Polymer Spectroscopy* (Verlag Chemie, London, 1973).

[111] P. A. Bentley and P. J. Hendra, Spectrochim. Acta A **51**, 2125 (1995).

[112] See, for example, W. G. Rothschild, J. Chem. Phys. **65**, 455 (1976).

[113] C. Hirose, N. Akamatsu, and K. Domen, Applied Spectroscopy **46**, 1051 (1992).

[114] S. Woutersen, U. Emmerichs, and H. J. Bakker, Science **278**, 658 (1997).

[115] H. K. Nienhuys, R. A. van Santen, and H. J. Bakker, J. Chem. Phys. **112**, 8487 (2000).

[116] M. Cho, G. R. Fleming, S. Saito, I. Ohmine, and R. M. Stratt, J. Chem. Phys. **100**, 6672 (1994).

[117] H. D. Downing and D. Williams, J. Geophys. Res. **80**, 1656 (1975).

[118] P. N. Butcher and D. Cotter, *The Elements of Nonlinear Optics* (Cambridge University Press, New York, 1990), p.25.

[119] P. Fischer and A. D. Buckingham, J. Opt. Soc. Am. B **15**, 2951 (1998).

[120] Y. R. Shen, Annu. Rev. Phys. Chem. **40**, 327 (1989).

[121] P. Ye and Y. R. Shen, Phys. Rev. B **28**, 4288 (1983).

Appendix A

$\chi^{(2)}$-related conventions

"The nonlinear-optics literature contains a tortuous jumble of inconsistent definitions" (from Ref [118] by Butcher and Cotter). Different conventions in nonlinear optics are indeed very confusing and difficult to keep track of. The purpose of this appendix is to clarify the conventions used in this thesis.

One confusion, which is probably the worst one, arises from permutation of the input fields. Depending on the convention, the definition of $\chi_{ijk}^{(2)}$ can have different forms, either without permutation of the fields

$$P_i^{(2)}(\omega_s) = \sum_{jk} \chi_{ijk}^{(2)} E_j(\omega_1) E_k(\omega_2) , \qquad (A.1)$$

or with permutation of the fields

$$P_i^{(2)}(\omega_s) = \sum_{jk} \chi_{ijk}^{(2)} [E_j(\omega_1) E_k(\omega_2) + E_j(\omega_2) E_k(\omega_1)] . \qquad (A.2)$$

The convention we have adopted is Eq. (A.1) with strict ordering of the input frequencies, i.e., $\omega_1 > \omega_2$. For second-harmonic generation (SHG) we can still use Eq. (A.1) with

$\omega_1 = \omega_2$. However, with our convention, $\chi_{ijk}^{(2)}$ for SFG is twice as large as its value for SHG as ω_1 approaches ω_2. This can be easily explained as follows.

Suppose we shine onto a sample surface two laser beams with the same frequency ($\omega_1 = \omega_2 = \omega$) but different incidence angles. In principle we should get three output beams at 2ω, i.e., the SHG of the first beam, the SHG of the second beam, and the SFG of the two. These three output beams will propagate in different directions depending on the in-plane phase matching condition. We can write down the expression for the nonlinear polarization induced by the two input fields,

$$
\begin{aligned}
P_i^{(2)}(2\omega) &= \sum_{jk} \chi_{ijk}^{(2)}(2\omega) \left[E_{1j}(\omega) + E_{2j}(\omega) \right] \left[E_{1k}(\omega) + E_{2k}(\omega) \right] \\
&= \sum_{jk} \chi_{ijk}^{(2)}(2\omega) \left[E_{1j}(\omega)E_{1k}(\omega) + E_{2j}(\omega)E_{2k}(\omega) + 2E_{1j}(\omega)E_{2k}(\omega) \right] \ . \quad \text{(A.3)}
\end{aligned}
$$

Here we have used the symmetry $\chi_{ijk}^{(2)}(2\omega) = \chi_{ikj}^{(2)}(2\omega)$. Note the factor of 2 in the cross term which contributes to the SFG of the two input fields. Now if we slightly detune the two input frequencies (assuming $\omega_1 > \omega_2$), we expect the SFG signal to change continuously, therefore,

$$
P_i^{(2)}(\omega_1 + \omega_2) \approx 2 \sum_{jk} \chi_{ijk}^{(2)}(2\omega) E_j(\omega_1) E_k(\omega_2) \ . \quad \text{(A.4)}
$$

Comparing with Eq. (A.1) we find

$$
\chi_{ijk}^{(2)}(\omega_1 + \omega_2) \approx 2\chi_{ijk}^{(2)}(2\omega) \ . \quad \text{(A.5)}
$$

To avoid such a discontinuity in $\chi_{ijk}^{(2)}$, sometimes a K-factor ($K = 1$ for SFG and $K = \frac{1}{2}$ for SHG [118]) or a g-factor ($g = 2$ for SFG and $g = 1$ for SHG [5]) is inserted into Eq. (A.1). But we have chosen not to do so.

To add even more confusion, there are two different ways to define $E(\omega)$ of a monochromatic light wave, i.e.,

$$\mathbf{E}(t) = \mathbf{E}(\omega)e^{-i\omega t} + c.c. \; , \qquad (A.6)$$

or

$$\mathbf{E}(t) = \frac{1}{2}\left[\mathbf{E}(\omega)e^{-i\omega t} + c.c.\right] \; . \qquad (A.7)$$

Depending on the choice, $\chi_{ijk}^{(2)}$ may differ by another factor of 2. We have chosen Eq. (A.6) as the convention for most of our publications. This explains why our Eq. (1.4) differs from that in Ref. [119] by Fisher and Buckingham, who had chosen Eq. (A.7) as their convention. Note that with Eq. (A.6), $E(\omega)$ is not the true amplitude of the electric field. One has to be careful when converting $E(\omega)$ to the power density.

In Sec. 1.3.2 the nonlinear susceptibility of quartz $\chi_{\mathrm{q}}^{(2)}$ differs from the d_{11} coefficient by a total factor of 4 [Eq. (1.6)] because $\chi_{\mathrm{q}}^{(2)}$ is for SFG with Eq. (A.6) as the convention for the field amplitude while d_{11} was measured by SHG with Eq. (A.7) as the convention.

There's yet another convention issue, and this is for the MKS units only. There are also two conventions in the definition of $\chi_{ijk}^{(2)}$ depending on whether or not ϵ_0 is included in Eq. (A.1). In this thesis I have included ϵ_0 in Eq. (A.1), as seems more common in the literature. Note that one paper of ours, Ref. [8], used the other convention. Therefore all the values of $\chi_{ijk}^{(2)}$ in that paper were different from those in Ref. [9] by a factor of ϵ_0.

Appendix B

Fresnel factors

The L_{ii} factors in Eq. (1.3) are the transmission Fresnel coefficients relating the field components in an input or output beam to the corresponding ones in the interfacial layer [2, 120]. For an interface between two continuous media with dielectric constants ϵ_1 and ϵ_2, we have

$$
\begin{aligned}
L_{XX}(\omega_i) &= \frac{2\epsilon_1(\omega_i)k_{2Z}(\omega_i)}{\epsilon_2(\omega_i)k_{1Z}(\omega_i) + \epsilon_1(\omega_i)k_{2Z}(\omega_i)} \ , \\
L_{YY}(\omega_i) &= \frac{2k_{1Z}(\omega_i)}{k_{1Z}(\omega_i) + k_{2Z}(\omega_i)} \ , \\
L_{ZZ}(\omega_i) &= \frac{2\epsilon_1(\omega_i)\epsilon_2(\omega_i)k_{1Z}(\omega_i)}{\epsilon_2(\omega_i)k_{1z}(\omega_i) + \epsilon_1(\omega_i)k_{2Z}(\omega_i)} \cdot \frac{1}{\epsilon'(\omega_i)} \ ,
\end{aligned}
\tag{B.1}
$$

where $\epsilon'(\omega_i)$ is an empirical dielectric constant of the surface monolayer at ω_i. The physical meaning of $\epsilon'(\omega_i)$ will be discussed in Appendix C.

The Fresnel factors for the surface of a thin film coated on a substrate are slightly more complicated. Details can be found in the appendices of Ref. [72]. In Chap. 3, however, the coated PVA film turns out to have little effect on the Fresnel factors because the thickness of the PVA film is only ~30 nm, much less than an optical wavelength, and the

138

refractive index of PVA is not too different from that of the fused silica substrate. Therefore we can use the calculated Fresnel factors listed in Table 3.1 for the air/fused quartz interface as a good approximation.

As discussed in Sec. 1.3, for buried interfaces or SFG in the transmitted direction, the Fresnel factors must still be defined as the coefficients relating the field at the interface to the field of the input or output beam in air or vacuum. In particular, for a buried interface with a thick cover layer, we may neglect multi-reflection and calculate the Fresnel factors in a "cascaded" fashion to take into account the effect of surface reflection and refraction. Let us take the silica/ice interface (Sec. 2.5.2) as an example. In this case, the overall Fresnel factor would be

$$L_{ii} = L_{ii}(\text{air} \to \text{silica}) \times L_{ii}(\text{silica} \to \text{ice}) \, . \tag{B.2}$$

Here $L_{ii}(\text{air} \to \text{silica})$ is the Fresnel factor relating the field in air to the field in silica, and $L_{ii}(\text{silica} \to \text{ice})$ is the Fresnel factor relating the field in silica to the field at the silica/ice interface.

Appendix C

Dielectric constant of the surface layer

In the theory of surface nonlinear optical spectroscopy we have introduced a dielectric constant ϵ' for the surface layer, which appears in the Fresnel factor L_{ZZ} in Eq. (B.1). From the theoretical point of view, the dielectric constant is not well defined for a monolayer because it is a macroscopic or mesoscopic property. However, ϵ' can be interpreted as a result of the microscopic local-field correction in a monolayer [55, 121].

We consider a surface monolayer of molecules at an interface between two media with dielectric constants ϵ_1 and ϵ_2. The local field components experienced by these molecules are

$$
E_X^{(\text{Loc})} = l_{XX}L_{XX}E_X ,
$$

$$
E_Y^{(\text{Loc})} = l_{YY}L_{YY}E_Y ,
$$

$$
E_Z^{(\text{Loc})} = l_{ZZ}L_{ZZ}E_Z , \tag{C.1}
$$

where l_{ii} denotes the microscopic local-field correction factor, L_{ii} is the Fresnel or macroscopic local-field factor (defined by Eq. (B.1) but without the factor $\frac{1}{\epsilon'}$), and E_i is the electric field component of the incoming and outgoing optical plane waves. If $l_{XX} = l_{YY} = l_\parallel$ and $l_{ZZ} = l_\perp$, the total local-field factors including both macroscopic and microscopic effects are

$$
\begin{aligned}
F_{XX} &= l_{XX}L_{XX} = l_\parallel \frac{2\epsilon_1 k_{2Z}}{\epsilon_2 k_{1Z} + \epsilon_1 k_{2Z}} \ , \\
F_{YY} &= l_{YY}L_{YY} = l_\parallel \frac{2k_{1Z}}{k_{1Z} + k_{2Z}} \ , \\
F_{ZZ} &= l_{ZZ}L_{ZZ} = l_\perp \frac{2\epsilon_1 \epsilon_2 k_{1Z}}{\epsilon_2 k_{1Z} + \epsilon_1 k_{2Z}} \ .
\end{aligned}
\tag{C.2}
$$

We notice that F_{ii} differs from L_{ii} in Eq. (B.1) only by a common factor $l_\parallel$ if we define

$$
\epsilon' = \frac{l_\parallel}{l_\perp} \ .
\tag{C.3}
$$

It has been shown that the value of ϵ' defined this way is usually between 1 and the bulk dielectric constant ϵ [55]. The physical meaning of ϵ' now becomes clear; it is simply the ratio of $l_\parallel$ to $l_\perp$. By introducing the factor $\frac{1}{\epsilon'}$ in Eq. (B.1), we have partially included the microscopic local-field correction. To have it fully included, the surface density N_S in Eqs. (2.8), (2.9), (3.4), (3.7), (5.15) and (5.16) should all be replaced with $N_S l_\parallel(\omega_s)l_\parallel(\omega_1)l_\parallel(\omega_2)$. The additional factor $l_\parallel(\omega_s)l_\parallel(\omega_1)l_\parallel(\omega_2)$ is usually neglected since it has no effect on our deduction of the orientational distribution function $f(\Omega)$.

A simple slab model was presented in the appendix of Ref. [55] to obtain an estimate of ϵ' and $l_\parallel$. For the surface of a medium with a bulk dielectric constant ϵ, this slab model gives

$$
l_\perp = \frac{2\epsilon + 1}{3\epsilon} \ ,
\tag{C.4}
$$

$$l_{\parallel} = \frac{\epsilon + 5}{6} \quad , \tag{C.5}$$

$$\epsilon' = \frac{\epsilon(\epsilon + 5)}{4\epsilon + 2} \quad . \tag{C.6}$$

ERNEST ORLANDO LAWRENCE BERKELEY NATIONAL LABORATORY
ONE CYCLOTRON ROAD | BERKELEY, CALIFORNIA 94720